

SCHEDDING LIGHT ON CARBON-OXYGEN WHITE DWARF MERGERS AND POST-MERGER
EVOLUTION

by

Chenchong Zhu

A thesis submitted in conformity with the requirements
for the degree of Doctor of Philosophy
Graduate Department of Astronomy & Astrophysics
University of Toronto

© Copyright 2016 by Chenchong Zhu

Abstract

Shedding Light on Carbon-Oxygen White Dwarf Mergers and Post-Merger Evolution

Chenchong Zhu

Doctor of Philosophy

Graduate Department of Astronomy & Astrophysics

University of Toronto

2016

the mechanism(s) by which a normally inert WD is agitated into exploding remains mysterious and widely debated.

“Do or do not; there is no try.”

–Yoda

Acknowledgements

I'd like to thank the academy for choosing me...

Contents

1	Introduction	1
1.1	White Dwarf Mergers	1
1.1.1	The Panopoly of Stellar Mergers	1
1.1.2	Mergers of WD Binaries	1
1.2	The Mystery of Type Ia Supernovae	2
1.2.1	Properties and Traditional Formation Channels of SNe Ia	3
1.2.2	Traditional Shortfalls	3
1.2.3	Brave New Channels	4
1.3	The vK10 SN Ia Channel	4
1.3.1	Hot DQs, High-Field Magnetic WDs, and Other Oddities	4
1.4	Thesis Overview	4
1.5	The Physics of Pre-Merger Evolution	5
1.5.1	Stable and Unstable Mass Transfer	5
1.5.2	Are Merging WDs Co-Rotating?	5
2	A Parameter-Space Study of Carbon-Oxygen White Dwarf Mergers	6
2.1	Introduction	7
2.2	Code and Input Physics	8
2.2.1	The SPH Code	8
2.2.2	Initial Conditions	9
2.2.3	Merger Completion Time	11
2.3	Results	11
2.3.1	Representative Mergers	11
2.3.2	Merger Trends	15
2.3.3	A Qualitative Picture of the Merger	29
2.4	Variation of Merger Parameters and Robustness of Results	30
2.4.1	Changing the Composition	30
2.4.2	Varying the Initial Binary Separation	30
2.4.3	Synchronization	33
2.4.4	Running the Simulation Longer	35
2.4.5	Viscosity Prescription	37
2.4.6	Spurious Heating	37
2.4.7	Resolution	39

2.5	Comparison With Others	41
2.5.1	Comparison With Lorén-Aguilar et al. (2009)	41
2.5.2	Comparison with Others	43
2.5.3	The Importance of Accurate Initial Conditions	43
2.6	Post-Merger Evolution	47
2.6.1	Viscous Evolution and Possible Spin Down	47
2.6.2	Possible Explosions?	50
2.7	Conclusion	50
2.8	Postscript: Post-Merger Evolution Revised	51
3	White Dwarf Mergers in Smoothed-Particle and Moving Mesh Hydrodynamics	56
3.1	Introduction	57
3.2	Codes and Initial Conditions	58
3.2.1	Traditional Smoothed-Particle Hydrodynamics	59
3.2.2	GASOLINE SPH Code	61
3.2.3	AREPO Moving Mesh Code	62
3.2.4	Initial Conditions and Completion Time	64
3.3	Improving Angular Momentum Conservation in Arepo	65
3.4	Results	70
3.5	Discussion	74
3.5.1	Resolution Test	74
4	Magnetized Moving Mesh Merger of a Carbon-Oxygen White Dwarf Binary	79
4.1	Introduction	80
4.2	Methods	80
4.3	Results	81
4.4	Robustness Tests	85
4.4.1	Resolution Test	85
4.4.2	Changing the Seed Field Strength	86
4.5	Discussion	86
4.6	Postscript: Reconsidering Divergence Cleaning in AREPO	88
Bibliography		89

List of Tables

List of Figures

2.1	Structure of a $0.4 - 0.8 M_{\odot}$ merger remnant, representing the general outcome of a merger of white dwarfs with dissimilar mass. Upper left and middle – binned maps of density ρ and temperature T along slices in the xy and xz -planes. Lower left – binned maps and contours of density, temperature, and angular frequency Ω in the (ω, z) plane, averaged over cylindrical coordinate ϕ and over $\pm z$ (with 1 added to Ω to avoid problems with the logarithmic intensity scale). Middle – enclosed masses of donor and accretor material M_d and M_a (solid red and blue, resp.), and fraction of donor material f_d at a particular mass shell (dashed magenta). Middle, one but lowest – temperature-density profile with enclosed masses in $0.2 M_{\odot}$ increments indicated, both along the equatorial plane (solid curve, squares) and along the rotational axis (dot-dashed curve, circles). Middle, bottom – enclosed mass as a function of r , with the total mass indicated by the horizontal dashed red line. Right-hand column, top to bottom - density, temperature, entropy, angular (cyan) and Keplerian (blue) frequency, and degeneracy (blue), thermal (red) and rotational (cyan) specific energies as a function of enclosed mass M , both along the equatorial plane and along the rotational axis (solid and dot-dashed curves, respectively). In all graphs, the start of the disk (where the centrifugal acceleration equals half the gravitational one) and the equatorial radius (or mass enclosed within) of maximum temperature are marked by vertical green and blue dashed lines, respectively. [See the electronic edition of the Journal for Figs. 1.1–1.48.]	12
2.2	As Fig. Set 2.1, but for a $0.6 - 0.6 M_{\odot}$ merger remnant, representing the general outcome of a similar-mass merger.	13
2.3	Properties of mergers with $0.65 M_{\odot}$ (left) and $1.0 M_{\odot}$ (right) accretors, for donor masses of 0.4 (red), 0.5 (orange), 0.55 (lime), 0.575 (green), 0.6 (cyan), 0.625 (light blue), 0.64 (blue), 0.65 (dark blue), 0.7 (magenta), 0.8 (purple), 0.9 (brown), and $1.0 M_{\odot}$ (black). Shown are, from top to bottom, density ρ , fraction of donor material f_d , angular frequency Ω , temperature T , specific thermal energy E_{th} , and specific rotational energy E_{rot} , all as a function of fractional enclosed mass M/M_{tot} . All properties are determined along the equatorial plane, except for f_d which is defined spherically. The $1.0 - 1.0 M_{\odot}$ merger (dashed black line) is an outlier; see text.	16
2.4	Dependence of the properties of mergers on mass difference, with, from left to right, $\Delta M \equiv M_a - M_d = 0.0, 0.1, 0.2$, and $0.3 M_{\odot}$ mergers. Properties shown, coloring, and line styles are as in Fig. 2.3, except color represents accretor mass.	17

- 2.5 Relation between central density ρ_c and mass M for carbon-oxygen white dwarfs, showing both the results of relaxing white dwarf models in Gasoline (red points), and integrating hydrostatic equilibrium directly for spherically symmetric, non-rotating CO WDs with $T = 5 \times 10^6$ K (blue line). For the mass range considered, the central density depends roughly exponentially on mass. 18
- 2.6 Dependence of merger core properties on the ratio of the donor and accretor central densities, $\rho_{c,d}/\rho_{c,a}$. Shown are the ratio of central to maximum temperature T_c/T_{\max} (squares), central to maximum angular velocity Ω_c/Ω_{\max} (triangles), and central core donor to accretor mass fraction $(f_d/f_a)_{cc}$ (circles), with colors representing different accretor masses, encoded as in Fig. 2.3. The vertical line marks $q_\rho \equiv \rho_{c,d}/\rho_{c,a} = 0.6$, where Ω_c/Ω_{\max} reaches unity, $(f_d/f_a)_{cc}$ becomes non-zero, and $T_c/T_{\max} \simeq 0.5$. We suggest it separates “dissimilar” from “similar” mass mergers. 19
- 2.7 Structural properties of mergers. (a) Central scaleheights along the rotational axis (circles) and along the equatorial plane (squares) scaled to the scaleheight of the accretor, h_z/h_a and h_ω/h_a . (b) Central density of the merger remnant scaled to the central density of the accretor, $\rho_c/\rho_{c,a}$. Colors represent different accretor masses, encoded as in Fig. 2.3. Triangles represent the outlying $1.0 - 1.0 M_\odot$ merger. 21
- 2.8 Mixing, heating, and spin-up (left to right) for mergers. (a) Scaled mass of the remnant core-envelope (where scaling here and below is to the accretor mass). (b) Fraction of the accretor within the mass enclosing half the donor mass. (c) Scaled remnant mass enclosing half the donor mass. (d) Fraction of the accretor mass within the region enclosing 25–75% of the donor mass. (e) Maximum equatorial temperature T_{\max} (circles), with the approximation $T_{\max} = 0.20GM_a m_p/k_B R_a$ overdrawn. Maximum temperatures along the rotational axis are shown with crosses. (f) Scaled density at the location of T_{\max} (symbols as above). (g) Scaled mass enclosed within the radius of T_{\max} (symbols as above). (h) Scaled mass enclosing half of the remnant thermal energy. (i) Scaled mass of the region enclosing 25 – 75% of the remnant thermal energy. (j) Maximum angular velocity Ω_{\max} (circles) with best fit $\Omega_{\max} = 3.8\Omega_{\text{orb}}$ overdrawn. (k) Fraction of the angular momentum in the core-envelope. (l) Scaled mass enclosed within the radius of maximum angular velocity. (m) Scaled mass enclosing half of the total remnant rotational energy. (n) Scaled mass of the region enclosing 25 – 75% of the remnant rotational energy. Colors represent different accretor masses, encoded as in Fig. 2.3. Triangles represent equatorial plane values, and x-marks rotational axis values, of the $1.0 - 1.0 M_\odot$ merger. 23
- 2.9 Partition of energies in (a) the overall merger remnant, (b) the remnant core plus envelope, and (c) the remnant disk. In each panel, the fraction of total energy carried in degeneracy (triangles), thermal (squares), and rotational (circles) energy is shown. Colors represent different accretor masses, encoded as in Fig. 2.3. Triangles represent the $1.0 - 1.0 M_\odot$ merger. 26
- 2.10 As Fig. 2.3, but for $0.4 - 0.4 M_\odot$ (left) and $0.4 - 0.8 M_\odot$ (right) mergers with different compositions: pure ${}^4\text{He}$ (red), CO (orange), and pure ${}^{24}\text{Mg}$ (lime). Dash-dotted lines represent profiles along the rotational axis rather than the equatorial plane. 31

2.11 As Fig. 2.10, but for $0.6 - 0.6 M_{\odot}$ (left) and $0.6 - 0.8 M_{\odot}$ (right) mergers with varying initial orbital separation: 0.9 (red), 1.0 (green), and 1.1 (blue) times the value used for the parameter space study.	32
2.12 As Fig. 2.10, but for $0.6 - 0.6 M_{\odot}$ (left) and $0.6 - 0.8 M_{\odot}$ (right) mergers, comparing our default, irrotational case (blue) with that assuming synchronous rotation (red).	34
2.13 As Fig. 2.10, but for $0.6 - 0.6 M_{\odot}$ (left) and $0.6 - 0.8 M_{\odot}$ (right) mergers, comparing properties for our default simulation time of 6 initial orbital periods (blue) with those obtained after 8 orbital periods (red).	36
2.14 As Fig. 2.10, but comparing simulations of a $0.6 - 0.8 M_{\odot}$ merger with different viscosity prescriptions (left) and simulations of a $0.625 - 0.65 M_{\odot}$ merger with different numbers of particles (right). For the viscosity, we compare fixed low viscosity ($\alpha = 0.05, \beta = 0.1$; blue), standard variable viscosity (green), and fixed high viscosity ($\alpha = 1.0, \beta = 2.0$; red). For particle numbers, we show simulations at one quarter (red), half (orange), and double (blue) the default number of particles, as well as the default simulation (lime) and a rerun of the default simulation (green) to determine the effect of order-of-execution differences, round-off errors and other such numerical effects.	38
2.15 Specific thermal energy as a function of enclosed mass for a $0.4 - 0.8 M_{\odot}$ (blue) and a $0.7 - 0.8 M_{\odot}$ merger (red), shown both along the equatorial plane (solid curves) and along the rotational axis (dot-dashed). Also shown are the (spherical) profiles found for an isolated $0.8 M_{\odot}$ white dwarf (dashed) simulated using the same parameters, and for the same completion times (six initial orbital periods, equivalent to 489 s and 224 s). Spurious heating is estimated to be responsible for nearly all the thermal energy in the core of the $0.4 - 0.8 M_{\odot}$ remnant, and for about one third in the core of the $0.7 - 0.8 M_{\odot}$ remnant. It is not important in regions heated by interaction. (The “hook” in the outer layers of the white dwarf profile reflects the high initial temperature chosen; in a merger, this is erased by the interaction.)	40
2.16 Comparison of our results with those of LIG09, for a $0.6 - 0.6 M_{\odot}$ (left) and a $0.6 - 0.8 M_{\odot}$ (right) merger. Shown are surface density, remnant (solid) and Keplerian (dashed) angular frequency, and temperature, with profiles from LIG09 in blue, and our equivalent ones in red and orange. Here, the former are for our default completion time of 6 initial orbital periods and the latter for their completion times (514 s or 10.9 orbital periods for the $0.6 - 0.6 M_{\odot}$ merger, and 164 s or 3.4 orbits for the $0.6 - 0.8 M_{\odot}$ merger).	42

2.17 Left: merger remnant maximum temperature T_{\max} and corresponding density $\rho(T_{\max})$ for all merger remnants. Values along the equatorial plane are marked with circles, with lines connecting points with the same accretor mass, while values along the rotational axis (only plotted for similar-mass mergers) are marked with triangles (for all, colors indicate accretor mass, encoded as in Fig. 2.3). For similar-mass mergers, equatorial temperatures have been adjusted to account for mixing in convectively unstable cores. Right: maximum temperatures and corresponding densities following estimated post-merger evolution. The estimate assumes that the remnant spins down completely, that all rotational energy is used to drive matter to large distances, and that the remainder adjusts adiabatically (see text). Also shown are contours of constant neutrino cooling timescale $\tau^* \equiv C_P T / \varepsilon_\nu$ and carbon fusion heating timescale $\tau_{\text{cc}} \equiv C_P T / \varepsilon_{\text{CC}}$, both in years, as well as entropy S in erg K^{-1} . (Here, C_P is the heat capacity at constant pressure and ε the specific energy loss/gain rate.) The lines labeled $\tau_{\text{cc}} = \tau^*$ and $\tau_{\text{cc}} = \tau_{\text{dyn}}$ denote where the carbon fusion heating timescale balances the neutrino cooling and dynamical timescales, respectively. Finally, the $P = 2P(T=0)$ line is shown as an approximate upper bound of the region where degeneracy pressure dominates. All quantities were calculated using MESA (Paxton et al. 2011).

45

2.18 Estimate of post-merger viscous evolution for $0.4 - 0.8 M_\odot$ (top) and $0.6 - 0.6 M_\odot$ (bottom) mergers. In blue are shown the temperature-density structure of the merger remnant, on the equatorial plane before (dotted) and after (solid) correction for convection, as well as along the rotational axis (dot-dashed), with points marking the hottest locations (circles and squares) and steps of $0.2 M_\odot$ in spherical enclosed mass (triangles pointing up and down). In red, estimates of the structure following viscous evolution are shown, where it is assumed that the remnant spins down completely, that all rotational energy is used to drive matter to large distances, and that the remainder adjusts adiabatically (see text). For reference, also shown as dotted curves are the contours of constant entropy from Fig. 2.17 (green), as well as the lines where $\tau_{\text{cc}} = \tau^*$ (magenta), $\tau_{\text{cc}} = \tau_{\text{dyn}}$ (red), and $P = 2P(T=0)$ (black).

46

2.19 Post-viscous degenerate core mass $M_{\text{c,pv}}$, estimated using the simple viscous evolution prescription in Sec. 2.6.1, as a function of remnant total mass M_{tot} , for the simulated systems of Z13 (points; colors have the same meaning as in Fig. 2.17) and the $0.625 - 0.65 M_\odot$ remnant from the AREPO MHD simulation (Ch. 4; red-blue star). Also plotted are estimates of $M_{\text{c,pv}}$ from Schwab et al. (2012; using $M_{\text{c}} + M_{\text{tp}}$ in their Table 3) and Ji et al. (2013; estimated from integrating its spherical density profile to $r = 2 \times 10^9 \text{ cm}$). The dotted line is a best fit to the Z13 points.

53

3.1 PLACEHOLDER!!!

3.2 Evolution of total z -axis angular momentum $L_{z,\text{tot}}$ (top cluster of lines in each panel) and that within a cylinder of radius $\omega = 10^9 \text{ cm}$, $L_{z,\omega < 9}$ (bottom cluster), for various simulations in 2013-2014, before AREPO was updated to better conserve angular momentum. All curves are shifted in time by $t_{\max(L_z)}$, the time in each simulation at which $L_{z,\omega < 9}$ achieved its maximum value, to synchronize the start of post-merger evolution. In the top panel, red and magenta lines represent the low and standard-resolution AREPO simulations, respectively, while the cyan and blue ones represents low and standard-resolution GASOLINE ones, respectively. Dotted lines represent angular momentum balance $L_{\text{bal}}(\omega < 10^9 \text{ cm})$, which should be flat in the absence of spurious angular momentum losses. (Slightly different initial amounts of total angular momentum between AREPO and GASOLINE runs are due to inconsistencies in their initial conditions that have subsequently been solved.) In the bottom panel, the red line is again the low-resolution AREPO simulation, while the green line is for an AREPO low-resolution run where the mesh is held static after $t = 114 \text{ s}$. The dashed black line is a FLASH simulation that uses the AREPO low-resolution run at $t = 114 \text{ s}$ for initial conditions; its loss of total angular momentum is due to having outflow boundaries.	67
3.3 Evolution of total z -axis angular momentum $L_{z,\text{tot}}$ (top cluster of lines) and that within a cylinder of radius $\omega = 10^9 \text{ cm}$, $L_{z,\omega < 9}$ (bottom cluster) for the AREPO-RKLSF simulations. All curves are shifted in time by t_c (rather than $t_{\max(L_z)}$), the time when average separation between donor and accretor material reaches a tenth of its initial value. Colors indicate initial resolution: green is for 5.1×10^4 cells, red for 2.5×10^5 , magenta for 1.3×10^6 and black for 2.5×10^6	69
3.4 Series of equatorial (xy) plane density (left two columns) and temperature (right two columns) intensity plots for five snapshots in time (rows; the time for each snapshot is indicated at the top left of the density plots) during the GASOLINE and AREPO simulations. xz -plane plots are also included for the final snapshot.	71
3.5 Merger remnant profiles from the GASOLINE (red), AREPO (blue) and AREPO MHD (gray; Zhu et al. 2015) simulations 99 s after coalescence (around row four of Fig. 3.4). The profiles are, from top to bottom, density ρ , angular rotation speed Ω , temperature T , specific degeneracy energy e_{deg} , specific thermal energy e_{th} , and specific rotational energy e_{rot} , all as a function of the ratio of spherical enclosed to total mass M/M_{tot} . Solid lines represent profiles on the original binary’s orbital plane, while dash-dotted lines represent profiles along the rotational axis.	72
3.6 Time evolution of z -axis angular momentum L_z for AREPO (solid lines) and GASOLINE (dotted) simulations. The purple line represents total L_z , while the others represent angular momentum within concentric cylinders aligned along the rotation axis and with radii $\omega = 5 \times 10^8$ (red), 7.5×10^8 (yellow), 1×10^9 (green), 1.5×10^9 (cyan), 3×10^9 (blue) and $6 \times 10^9 \text{ cm}$ (magenta).	74
3.7 Merger remnant profiles, as in Fig. 3.5, for GASOLINE (left column) and AREPO (right) simulations of various (initial, for AREPO) mass resolutions. Resolutions include $5 \times 10^{28} \text{ g}$ (equivalent to 5.1×10^4 particles/cells; red lines), $1 \times 10^{28} \text{ g}$ (2.6×10^5 ; green) $2 \times 10^{27} \text{ g}$ (1.3×10^6 ; cyan) and $1 \times 10^{27} \text{ g}$ (2.6×10^6 ; blue).	76

4.1	Series of temperature T (left column) and magnetic field strength $ B $ (right) logarithmic intensity profiles in the equatorial plane of the merger for four snapshots in time (rows; time indicated at the top left of each row).	82
4.2	Total magnetic energy E_B over time, with a best fit to the rapid exponential growth (dashed $E_B \propto e^{t/6.4s}$ line).	83
4.3	From leftmost to rightmost column, equatorial plane (top row) and polar (bottom) logarithmic intensity profiles of density ρ , temperature T , magnetic field strength $ B $ and ratio of magnetic to rotational energy density e_B/e_{rot} for the simulation at 400 s (~ 170 s after coalescence). The equatorial plane density plot includes a linear profile of the remnant core (with the same x and y scale as the logarithmic profile) to show its shape. Arrows in the magnetic field strength plots indicate field directions, with their lengths equal to the fraction of the field that lies along the xy plane (top frame) and xz plane (bottom).	84
4.4	Total magnetic energy E_B over time for the fiducial (solid blue; $m_{\text{cell}} \approx 1 \times 10^{-6} M_{\odot}$, equatorial surface field strength 10^3 G) simulation and the robustness tests. Dashed lines represent low (green; $m_{\text{cell}} \approx 5 \times 10^{-6} M_{\odot}$) and high resolution (red; $m_{\text{cell}} \approx 2 \times 10^{-7} M_{\odot}$) simulations. Dotted lines represent 1 G (magenta) and 10^{-3} G (cyan) low initial field simulations.	85
4.5	From top to bottom, equatorial plane intensity profiles for the magnetic field strength, relative divergence error (linear scale) and absolute relative divergence error (logarithmic) for the simulation at 200 s.	90

Chapter 1

Introduction

1.1 White Dwarf Mergers

1.1.1 The Panopoly of Stellar Mergers

Approximately two out of every three stars are born into a binary system. A substantial fraction of these stars will interact, some due to their orbital separation at birth, while others following the expansion of one or both constituent stars as they evolve off of the main sequence. These interactions primarily take form as mass transfer between the stars (Yungelson 2005), and if mass transfer becomes unstable (increases exponentially over time), it ends with the violent coalescence of the two stars into one. These stellar mergers, like other forms of binary interaction, disrupt single star evolution and create merged products, or “merger remnants”, with unusual properties including blue stragglers (eg. Andronov et al. 2006; Knigge et al. 2009), luminous blue variables (Justham et al. 2014), subdwarf OB and R Corona Borealis stars. They also liberate tremendous amounts of energy and eject significant amounts of mass, giving rise to a cornucopia of electromagnetic and gravitational-wave transients ranging from luminous red novae (from the merger of two (post-) main-sequence stars; eg. V838 Monocerotis and V1309 Scorpii (Tylenda et al. 2011; Nandez et al. 2014)) to short gamma-ray bursts (from two neutron stars; eg. Rosswog (2015)) and the gravitational wave outburst from coalescing stellar-mass black holes (as recently found by the LIGO detector; Abbott et al. 2016). Indeed, with current deep and short-cadence optical/near-infrared survey projects such as the Palomar Transient Factory (Rau et al. 2009) and Pan-STARRS (Kaiser et al. 2010) continuing to uncover more rare and even hitherto-unknown transients, and the ambitious Large Synoptic Survey Telescope (LSST Science Collaboration et al. 2009) under construction, a much more complete picture of merger-generated transients will form over the next decade.

1.1.2 Mergers of WD Binaries

One common end-product of binary stellar evolution is the merger of two white dwarfs (WDs) in a close binary orbit. Close WD binaries are formed as a result of at least two phases of mass transfer (at least one of which is a common envelope event) during the binary’s prior stellar evolution. These mass transfer phases act to sap the orbital angular momentum of the

A few percent of all white dwarfs (WDs) will eventually merge with another white dwarf. The

outcome of such mergers will depend on the compositions of the WDs involved. For two helium WDs, a low-mass helium star might result, which would be observed as an sdOB star. For a helium WD merging with a carbon-oxygen one, a helium giant could form, observable as a hydrogen-deficient giant or R CrB star. For two carbon-oxygen WDs (CO WDs), the outcome could vary between simply a more massive WD, a carbon-burning star, an explosion, or collapse to a neutron star, depending on whether stable or unstable carbon fusion is ignited, and whether the total mass exceeds the critical mass for pycnonuclear ignition or electron captures (both close to the Chandrasekhar mass M_{Ch}). For mergers involving an oxygen-neon WD, the mass will always be high, and explosive demise or transmutation seems inevitable.

White dwarf (WD) binaries are common end products of binary stellar evolution. Gravitational wave emission, magnetic braking or the influence of a third body will cause a fraction of these to merge, producing a diversity of unusual stars and electromagnetic transients. In particular, for double carbon-oxygen (CO) WD mergers, the final outcome could be a massive and rapidly rotating WD (eg. Segretain et al. 1997), an accretion-induced collapse into a neutron star (NS) (Saio & Nomoto 1985), or a nuclear explosion that might resemble a type Ia supernova (SN Ia).

1.2 The Mystery of Type Ia Supernovae

The outcome of the merger of two CO WDs is uncertain in part because during the merger temperatures do not become hot enough to ignite significant carbon fusion (e.g., Lorén-Aguilar et al. 2009, LIG09 hereafter), except possibly for masses above $\sim 0.9 M_{\odot}$ (Pakmor et al. 2011b; 2012). Hence, the final fate depends on subsequent evolution, in which differential rotation is dissipated, the remnant disk accretes, and the whole remnant possibly spins down. Due to these processes, the remnant could be compressed and heated, which, if it happens faster than the thermal timescale, would lead to increased temperatures and thus potentially to ignition.

So far, efforts have focused on merging binaries with total mass $M > M_{\text{Ch}}$. The end result of such mergers is believed to be either stable off-center carbon ignition, which would turn the merger remnant into an oxygen-neon WD and possibly eventually result in accretion-induced collapse (Saio & Nomoto 1998), or slow accretion, which allows the remnant to stay cool and eventually ignite at high central density (Yoon et al. 2007). Less massive mergers were usually thought to result in more massive, rapidly rotating CO WDs (Segretain et al. 1997; Külebi et al. 2010), but more recently it has been realized these might eventually become hot enough to ignite (van Kerkwijk et al. 2010, vK10 hereafter; Shen et al. 2012; Schwab et al. 2012). Indeed, vK10 argue that type Ia supernovae result generally from mergers of CO WDs with similar masses, independent of whether or not their total mass exceeds M_{Ch} (see below). For all these studies, the conclusions on whether and where ignition takes place depend critically on the structure of the merger remnant.

The merger of two white dwarfs (WDs) originally in a short-period binary is estimated (eg. Badenes & Maoz 2012) to occur about once every century in a Milky Way-like galaxy, making the products of such events common throughout the universe. They have been held responsible for producing a variety of stars with strange properties, including helium-burning sdOB stars (Saio & Jeffery 2000; Justham et al. 2011), RCrB stars (eg. Webbink 1984; Clayton et al. 2007; Clayton 2013), and massive and highly magnetized WDs (eg. Segretain et al. 1997; García-Berro et al. 2012; Külebi et al. 2013) that could resemble the hot DQ WDs (eg. Dunlap & Clemens 2015), Dunlap and Clemens in preparation).

They may, however, also be responsible for spectacular transient events including accretion-induced collapses (eg. [Saio & Nomoto 1985](#); [Abdikamalov et al. 2010](#)) and type Ia supernovae (SNe Ia; eg. [Howell 2011](#); [Hillebrandt et al. 2013](#); [Maoz et al. 2014](#)). Determining the final outcome of a particular merger requires an understanding of the detailed dynamics of the merging process, which cannot directly be seen using current observational capabilities. Thus, studies of merger physics have primarily utilized hydrodynamic simulations.

1.2.1 Properties and Traditional Formation Channels of SNe Ia

1.2.2 Traditional Shortfalls

The traditional method of generating an SN Ia involves slow accretion of material over $\sim 10^6$ yr onto the CO WD from either a non-degenerate companion or an accretion disk following a merger with another WD. As the CO WD approaches the Chandrasekhar mass M_{Ch} , its central density becomes sufficiently high that the rate of energy generation from pycnonuclear carbon-carbon nuclear fusion exceeds that at which neutrino cooling can transport it away. The resulting increase in central entropy establishes a convection zone that transports the heat of the nuclear burning region to much of the WD interior. The WD is highly degenerate, however, and does not expand and cool in response to heating. Instead, a nuclear runaway ensues over the next thousand years as the WD grows ever hotter, a period of evolution referred to as the “simmering phase”. M_{Ch} WDs eventually become hot enough that the timescale for nuclear burning becomes shorter than the dynamical time – we refer to this as “dynamical burning” – at which point an explosion becomes inevitable.

This scenario is beset by several issues ([van Kerkwijk et al. 2010](#), henceforth vK10, and references therein). The first is that, in order to match the observed SN Ia rate, $\sim 1\%$ of all WDs formed (of any composition and regardless of binarity) must produce SNe Ia (?). Compared to this relatively large number, there is an apparent paucity – by a factor of at least a few – of both CO WDs accreting efficiently from non-degenerate companions (?) and merging CO - CO WD binaries whose total mass exceeds M_{Ch} ([Badenes & Maoz 2012](#)). The second is the difficulty for the thermonuclear explosion of an M_{Ch} mass CO WD to replicate the properties and population-level trends of ordinary SN Ia (such as the ? relation between peak luminosity and brightness decay time), without appealing to an *ad-hoc* deflagration-to-detonation transition (?). Recent years have also revealed substantial populations of sub and superluminous SNe Ia (eg. ?). If these SNe are also generated by exploding CO WDs, then either the classical scenario above is robust enough to explain them, or alternative channels to exploding WDs must also occur in nature.

The challenge posed by these issues has spurred research into alternative scenarios where CO WDs with masses significantly *below* M_{Ch} can also explode. This obviously bolsters substantially the number of CO WDs that could be SN Ia progenitors. Sub- M_{Ch} explosions also do not need to appeal to the deflagration-to-detonation transition: simulations of pure detonations of sub- M_{Ch} CO WDs ([Shigeyama et al. 1992](#); [Sim et al. 2010](#)) are competitive with M_{Ch} explosion models for reproducing the light curves and spectra of SNe Ia (?). Some SN Ia population trends, most notably the Phillips relation and the correlation between SN Ia luminosity and host stellar population age (eg. ?), can also naturally be explained by exploding CO WDs with a range of masses (vK10).

1.2.3 Brave New Channels

1.3 The vK10 SN Ia Channel

Hydrodynamic simulations (Lorén-Aguilar et al. 2009) suggest that a $0.6 - 0.6 M_{\odot}$ merger never achieves temperatures high enough to ignite fusion (more recent work (eg. (Pakmor et al. 2011b; Dan et al. 2012)) suggest $\sim 0.9 M_{\odot}$ as the minimum accreting WD mass for this to occur); moreover, the remnant central density, $\sim 2.5 \times 10^6 \text{ g cm}^{-3}$, is too low to produce ^{56}Ni in an explosion. Following coalescence, however, the remnant, which is differentially rotating, enters a period of rapid angular momentum redistribution due to hydrodynamically or magnetically-mediated viscosity. Using the standard α -viscosity prescription Shakura & Sunyaev (1973) – i.e. $\nu = \alpha c_s H_P$, where c_s is the sound speed and H_P the pressure scale height – the timescale for viscous evolution can be estimated as

$$\begin{aligned} t_{\text{visc}} &= \frac{R_{\text{disk}}^2}{\nu} \sim \frac{1}{\alpha} \frac{R_{\text{disk}}^2}{H_P^2} \tau_{\text{dyn}} \\ &\sim 3 \times 10^4 \text{ s} \left(\frac{10^{-2}}{\alpha} \right) \left(\frac{R_{\text{disk}}/H_P}{10} \right)^2 \left(\frac{R_{\text{disk}}}{10^9 \text{ cm}} \right)^{3/2} \left(\frac{M_{\text{enc}}}{1 M_{\odot}} \right)^{-1/2}, \end{aligned} \quad (1.1)$$

where M_{enc} is we have used $\tau_{\text{dyn}} \approx H_P/c_s$ and inserted a fiducial viscosity and typical numbers for remnants (Shen et al. 2012). Thus the vast majority of the remnant’s angular momentum is transported away, and the remnant (including its disk) loses its rotational support against gravity, over a period $\sim 10^4 \text{ s}$.¹ This loss of rotational support combined with increasing weight from newly accreted disk material leads to compression and heating of the remnant core. Since $\sim 10^4 \text{ s}$ is far shorter than either the neutrino cooling timescale of $\tau_{\nu} \sim 10^3 \text{ yr}$ or the thermal adjustment timescale of $\sim 10^4 \text{ yr}$ (Shen et al. 2012), compressional heating is adiabatic, and vK10 estimates that for the $0.6 - 0.6 M_{\odot}$ remnant it leads both the central density and temperature to increase to $\gtrsim 1.5 \times 10^7 \text{ g cm}^{-3}$ and $\gtrsim 10^9 \text{ K}$, at which point a carbon nuclear runaway is inevitable.

Thus, the vK10 channel is both attractive for its many advantages and plausible given the order-of-magnitude estimates above. Investigating whether these estimates hold under detailed scrutiny, and to determine which, if any, systems in the CO WD binary parameter space could follow the channel, is the purpose of this PhD thesis.

1.3.1 Hot DQs, High-Field Magnetic WDs, and Other Oddities

1.4 Thesis Overview

The chapters are ordered in accordance with the proposed evolution of the vK10 channel. In Chapter 2, we consider the range of possible merger remnant configurations to arise from the parameter space of merging CO WD binaries. In

For the most part, I have reproduced exactly the texts of Z13, Z15 and ? in their respective chapters. The exceptions are the chapter introductions, where I have excised certain paragraphs to eliminate the

¹This is notably in contrast to earlier work (eg. (Nomoto & Iben 1985; Yoon et al. 2007)) that assume any rotationally-supported material will slowly accrete onto the dense core of the remnant at a near-Eddington mass accretion rate of $\dot{M} \sim 10^{-5} M_{\odot} \text{ yr}^{-1}$. Remnants are prone to magnetic instability (Sec. ??), and will almost certainly evolve over the much shorter timescale given by the α -viscosity estimate.

redundancy of having multiple paragraphs repeating an overview of the vK10 channel. The papers' abstracts have also been modified into chapter overviews, and certain figures reformatted for readability. Any additional changes are noted at the start of each chapter. Most prominently, we have added a postscript to Chapter 2 (Sec. ??) that considers our simple semi-analytical prescription for post-merger viscous evolution in light of new results, and we included an extensive appendix to Chapter ?? that details our calculation of convective suppression in magnetized, rotating WDs.

1.5 The Physics of Pre-Merger Evolution

To preface Chapter 2, which focuses on the merger remnants, we briefly cover a few topics related to evolution of the CO WD binary leading up to mass transfer, and the early stages of mass transfer leading up to the merger proper (which we refer to as "coalescence").

1.5.1 Stable and Unstable Mass Transfer

In Chapter 2, every single one of our simulated binaries merge, as we use approximate initial conditions that place unperturbed, spherical WDs at separations that guarantee immediate Roche lobe overflow. An order of magnitude estimate, however, would suggest that binaries with sufficiently small mass ratios would not merge at all.

1.5.2 Are Merging WDs Co-Rotating?

While this question is something that we shall discuss at length in Ch. 2 (and is also considered in other works such as ? and [Ji et al. \(2013\)](#)) the results of Ch. ?? suggest that it is likely unimportant for the configuration of the merger remnant (at least to first order).

Check Schwab+12 intro for synchronization links.

Chapter 2

A Parameter-Space Study of Carbon-Oxygen White Dwarf Mergers

Chenchong Zhu, Philip Chang, Marten H. van Kerkwijk and James Wadsley
The Astrophysical Journal, Volume 767, Issue 2 - article id. 164, 32 pp., 2013
([Z13](#))

As we discussed in Sec. ??, the merger of two carbon-oxygen white dwarfs can lead either to a spectacular transient, stable nuclear burning or a massive, rapidly rotating white dwarf. Previous simulations of mergers have shown that the outcome strongly depends on whether the white dwarfs are similar or dissimilar in mass ([Lorén-Aguilar et al. 2009](#)). In the similar-mass case, both white dwarfs merge fully and the remnant is hot throughout, while in the dissimilar case, the more massive, denser white dwarf remains cold and essentially intact, with the disrupted lower mass one wrapped around it in a hot envelope and disk.

In order to determine what constitutes “similar in mass” and more generally how the properties of the merger remnant depend on the input masses, we simulated unsynchronized carbon-oxygen white dwarf mergers for a large range of masses using smoothed-particle hydrodynamics. We find that the structure of the merger remnant varies smoothly as a function of the ratio of the central densities of the two white dwarfs. A density ratio of 0.6 approximately separates similar and dissimilar mass mergers. Confirming previous work, we find that the temperatures of most merger remnants are not high enough to immediately ignite carbon fusion. During subsequent viscous evolution, however, the interior will likely be compressed and heated as the disk accretes and the remnant spins down. We find from simple estimates that this evolution can lead to ignition for many remnants. For similar-mass mergers, this would likely occur under sufficiently degenerate conditions that a thermonuclear runaway would ensue.

Aside from redundant parts of the introduction, we also do not reproduce here the extensive Appendix to [Z13](#), which contains tables of binary input parameters and remnant properties for the simulations.

2.1 Introduction

Until recent years, efforts to find SN Ia progenitors among merging CO WD binaries have focused on those with total mass $M > M_{\text{Ch}}$. The end result of such mergers is believed to be either stable off-center carbon ignition, which would turn the merger remnant into an oxygen-neon WD and possibly eventually result in accretion-induced collapse (Saio & Nomoto 1998), or slow accretion, which allows the remnant to stay cool and eventually ignite at high central density (Yoon et al. 2007). Less massive mergers were usually thought to result in more massive, rapidly rotating CO WDs (Segretain et al. 1997; Külebi et al. 2010), but more recently it has been realized these might eventually become hot enough to ignite (van Kerkwijk et al. 2010, vK10 hereafter; Shen et al. 2012; Schwab et al. 2012). Indeed, vK10 argue that type Ia supernovae result generally from mergers of CO WDs with similar masses, independent of whether or not their total mass exceeds M_{Ch} . For all these studies, the conclusions on whether and where ignition takes place depend critically on the structure of the merger remnant.

The merging process, and the merger remnant, have been studied quite extensively, mostly using smoothed-particle hydrodynamics (SPH; e.g. Monaghan 2005). These simulations have shown that the outcome strongly depends on whether the WDs are similar or dissimilar in mass. In the similar-mass case, both WDs disrupt fully and the remnant is hot throughout, while in the dissimilar case, the more massive, denser WD remains essentially intact and relatively cold, with the disrupted lower mass one wrapped around it in a hot envelope and disk. Less clear, however, is what constitutes “similar-mass,” and, more generally, how the merger remnant properties depend on the initial conditions.

In principle, for cold WDs of given composition, the remnant properties should depend mostly on the two WD masses, with a second-order effect due to rotation. In this paper, we try to determine these dependencies using simulations of WD mergers with the Gasoline SPH code, covering the entire range of possible donor and accretor masses, but limiting ourselves to non-rotating WDs. Our primary aim is to identify trends between mergers of different masses, both to guide analytical understanding and to help scale other, perhaps more precise simulations. Here, our hope is that while the results of individual simulations may suffer from uncertainties related to the precise techniques and assumptions used, the trends should be more robust. We also try to provide sufficient quantitative detail on the properties of merger remnants that it becomes possible to make analytical estimates or construct reasonable numerical approximations without having to run new simulations.

Our work is complementary to the recent surveys of remnant properties by Raskin et al. (2012) and Dan et al. (2012), in that they focus on different scientific questions (e.g., orbital stability; possible detonation). In contrast to our work, they assume that the WDs are co-rotating with the orbit. Whether this is a better assumption than no rotation depends on the strength of tidal dissipation, which unfortunately is not yet known (see Marsh et al. 2004; Fuller & Lai 2012).

This chapter is organised as follows. In Section 2.2, we describe the SPH code we used, as well as our initial conditions. In Section 2.3, we present our results and give trends for a number of pertinent remnant properties. In Section 2.4, we test the robustness of our results, and in Section 2.5 compare our results with those of LIG09 and others. Lastly, in Section 2.6, we speculate on the further evolution of our remnants, considering in particular whether, as suggested by vK10, some might lead to type Ia supernovae.

2.2 Code and Input Physics

We simulate the mergers by placing non-rotating white dwarfs in a circular orbit with an initial separation a_0 chosen such that rapid mass transfer begins immediately. We then follow the merger for six orbits, at which time the remnant has become approximately axisymmetric. As in prior work, the morphology of all merger remnants is similar, consisting of a dense, primarily degeneracy-supported center surrounded by a partly thermally-supported hot envelope (called a “corona” by LIG09) and a thick, sub-Keplerian disk. We will use the terms “core”, “envelope” and “disk” throughout this work. We also quite often refer to both the core and envelope simultaneously as the “core-envelope”.

We use simulation techniques and initial conditions that are standard in the field of WD merger simulations, both in order to compare with previous work, as well as to not introduce novel numerical effects into our simulations. We detail our code and initial conditions below so that they can easily be reproduced.

2.2.1 The SPH Code

With smoothed-particle hydrodynamics, one uses particles as a set of interpolation points to determine continuum values of the fluid and model its dynamics. SPH is a Lagrangian method, meaning movement is automatically tracked, and regions of high density contain more particles and therefore are automatically more resolved. Moreover, SPH inherently conserves angular momentum in three dimensions, which is difficult to reproduce in grid codes except under specific coordinate systems and symmetries. SPH therefore allows one to efficiently simulate complex phenomena with a large range of lengthscales. It has become the method of choice for merger simulations, and so we chose it as well.

For our simulations, we use Gasoline (Wadsley et al. 2004), a modular tree-based SPH code that was designed and has been used for a wide range of astrophysical scenarios, from galaxy interactions to planet formation. It aims for tight controls on force accuracy and integration errors. Gasoline implements the Hernquist & Katz (1989) kernel – we use 100 neighbors – and uses the asymmetric energy formulation (Wadsley et al., Eqn. 8) to evolve particle internal energy. In our simulations, total energy is on average conserved to 0.3%, and angular momentum to 0.006%.

By default, Gasoline uses the usual Monaghan and Gingold formulation for artificial viscosity (see Monaghan 2005), together with a Balsara switch (a standard feature of WD merger SPH simulations) to reduce viscosity in non-shocking, shearing flows. Guerrero et al. (2004) found that such a prescription did not reduce viscosity sufficiently, resulting in excess spin-up of the remnant core and associated shear heating. Yoon et al. (2007), in addition to a Balsara switch, used variable coefficients for the linear and quadratic viscosity terms in the SPH equations of motion and energy, setting these values to $\alpha = 0.05$ and $\beta = 0.1$, respectively, where shocks are absent, and around unity where they are present. A similar formulation was used in Dan et al. (2011; 2012). Since Gasoline includes it as well, we have used it for our study. Excess viscosity nevertheless remains a potential problem; we investigate its effects further in Sec. 2.4.5.

We modified Gasoline to include support for degenerate gas through the Helmholtz equation of state (EOS)¹ (Timmes & Swesty 2000). This code, also used in Raskin et al. (2012) and Dan et al. (2012)’s simulations, interpolates the Helmholtz free energy of the electron-positron plasma, along with analytical expressions for ions and photons, to determine pressure, energy and other properties

¹ Available at <http://cococubed.asu.edu/>.

from density and temperature. It is fast, spans a large range of density and temperature, and has, by construction, perfect thermodynamic consistency. To obtain quantities as a function of density and internal energy, we utilized a Newton-Raphson inverter. To keep the energy-temperature relation positive-definite, we did not disable Coulomb corrections in cases where total entropy became negative.

Gasoline keeps track of the internal energy of particles, using it to determine other thermodynamic properties for fluid evolution. A particle’s energy will naturally fluctuate due to noise, but for nearly zero-temperature particles this could result in their energy dipping below the Fermi energy. In such situations we keep the pressure at the Fermi pressure, while letting the energy freely evolve. A consequence of the floor is that a small amount of excess energy is injected into the system through mechanical work, which eventually manifests as additional thermal energy. The accumulated energy over a simulation is typically a small fraction of the internal energy, and therefore does not significantly affect the dynamics of the merger or most properties of the remnant. In cold, degeneracy-dominated material, however, a small change in internal energy corresponds to a large temperature change, at times comparable to the physically expected values, and thus the temperatures near the centers of some of our simulations have been affected. We characterize this spurious heating in Sec. 2.4.6 and show that it does not unduly affect our work’s conclusions. However, it makes it difficult to run much longer simulations.

We also place an energy floor at half the Fermi energy. This is to prevent particle energies from approaching zero (and consequently calling for tiny timesteps), which under rare circumstances occurs when particles perform a great deal of mechanical work. We find this happens primarily for particles that are flung out of the system by the merger and are cooling rapidly, and therefore are confident it has only a very minor effect on our simulations.

In our work, we ignore outer hydrogen and helium layers, composition gradients, and any nuclear reactions. This is mainly because previous work has found that nuclear processing was unimportant during the merger. For instance, LIG09 found fusion released $\sim 10^{41}$ erg for their $0.6 - 0.8 M_{\odot}$ merger, orders of magnitude smaller than the $\sim 10^{50}$ erg binding energy of the remnant. Only for mergers involving very massive, $\gtrsim 0.9 M_{\odot}$ WDs might this assumption break down, with the possibility of carbon detonations arising (Pakmor et al. 2010; 2011b; 2012; but see Raskin et al. 2012; Dan et al. 2012). Similarly, Raskin et al. (2012), who included standard helium envelopes of $\sim 1 - 2\%$ of the WD mass in their simulations, found that only for accretors with masses above $\sim 1 M_{\odot}$ did it make a substantial difference: a helium detonation would inject $\sim 10^{49}$ erg into the merger remnant. While this led to additional heating, it was insufficient to trigger much carbon burning or unbind any portion of the remnant (helium detonations have also been found for lower-mass accretors with CO-He hybrid donors; Dan et al. 2012).

2.2.2 Initial Conditions

We created spherical white dwarfs using pre-relaxed cells of particles rescaled to follow the appropriate enclosed mass-radius relation determined using the Helmholtz equation of state. We assumed a composition of 50% carbon and 50% oxygen by mass, and a uniform temperature of 5×10^6 K. The stars were then relaxed in Gasoline for 81 s ($\sim 10 - 40$ dynamical times, depending on the white dwarf mass) with thermal energy and motion damped (to 5×10^6 K and 0 cm s^{-1} , respectively) during the first 41 s, and left free during the remaining 40 s. Particle energy noise prevented cooling of $\gtrsim 5 \times 10^6 \text{ g cm}^{-3}$ material to below 10^7 K. We checked that the density profile of each star after relaxation was consistent

with the solution from hydrostatic equilibrium, and found this was the case – central densities, for example, agreed to within 2%. The radii of the relaxed stars, as defined by the outermost particle of a relaxed WD, on the other hand were on average about 7% too small, reflecting our inability to model the tenuous WD outer layers².

We used a constant particle mass of 10^{28} g, so that a $0.4 M_{\odot}$ WD has 8×10^4 particles, and a $1.0 M_{\odot}$ WD has 2×10^5 . These numbers are similar to those used by LIG09 and Yoon et al. (2007), and exceed the $\sim 2 \times 10^4$ particles per star used by Dan et al. (2012). Raskin et al. (2012) performed a resolution test for a merger of two $0.81 M_{\odot}$ WDs, varying the number of particles per star from 10^5 to 2×10^6 . They found differences of $\sim 2\%$ in the mass of the core plus envelope, disk half-mass radius, and inner disk rotation frequency. The one qualitative difference they found was that at their highest particle resolution, the WDs failed to break symmetry and disrupt (note that they assumed co-rotating WDs, making such a stable contact configuration possible). We perform our own test in Sec. 2.4.7 and find similar results.

We relaxed $0.4, 0.5, 0.55, 0.6, 0.65, 0.7, 0.8, 0.9$ and $1.0 M_{\odot}$ white dwarfs, and combined them in all possible permutations to form our parameter space of binaries. These values were chosen to represent the range of possible CO WD masses, with greater resolution near the empirical peak at $\sim 0.65 M_{\odot}$ of the mass distribution of (single) CO WDs (Tremblay & Bergeron 2009). We also performed additional simulations with $0.575 - 0.65, 0.625 - 0.65$ and $0.64 - 0.65 M_{\odot}$ binaries to explore the outcomes of similar-mass mergers. We thus simulated 48 mergers in total.

We placed two relaxed, irrotational WDs in a circular orbit. We chose the initial separation a_0 such that the donor WD just fills its Roche lobe, taking the location of the donor’s outermost particle as its radius and using the Roche lobe approximation (for a synchronized binary) from Eggleton (1983).

This simple initial condition is similar to that of Pakmor et al. (2010), and implies that the binary system as a whole is not equilibrated. Therefore, as the simulation begins, the two WDs react to the tides, become stretched, and strong Roche lobe overflow ensues because the donor overshoots its Roche radius (in a widely separated binary, the donor would start to pulsate). As a result, the donor disrupts after just one to two orbits. For synchronized binaries, Dan et al. (2011) showed that the onset of mass transfer is much more gentle if the WDs are relaxed in the binary potential, disruption occurring only after several dozen orbital periods. They also showed that this results in systematic changes in the merger remnants. It is not clear whether the same will hold for unsynchronized binaries, since the accretion stream hits a surface that, in its frame, counterrotates, and therefore accretion is always much less gentle than for synchronized WDs. The difference is particularly dramatic for similar-mass binaries, where, in the synchronized case, the WDs can come into gentle contact, while in the unsynchronized case, any contact is violent. Unfortunately, it is difficult to test the effect of proper equilibration for unsynchronized binaries, since one has to relax to non-trivial initial conditions. A better approximation was attempted by LIG09 and Guerrero et al. (2004), who started their WDs further out and reduced the separation artificially until mass transfer began. In their simulations, disruption still followed very quickly. Given that, and wanting to avoid any partial synchronization, we kept our simpler setup, and tested it by running simulations with varying a_0 . We will discuss these tests in Sec. 2.4.2 and compare our results with those of others in Sec. 2.5.

²Our relaxed WDs also show evidence of sub-kernel radial banding of particles, which does not appear in any interpolated quantities. We do not believe this banding has an effect on our simulations except for a possible reduction in effective resolution, but will investigate remedies in future work.

2.2.3 Merger Completion Time

It is difficult to decide when a merger is “complete”, since for some cases remnant properties continue to evolve long after the two WDs coalesce, with (artificial) viscosity redistributing angular momentum and heating the remnant. As a visually inspired criterion, we decided initially to use the degree of non-axisymmetry, continuing simulations until they were less than 2.5% non-axisymmetric, as measured from the ratio of zeroth to largest non-zero Fourier coefficient of particles binned in azimuth. However, this had its own issues: in dissimilar-mass mergers – where most of the particles are in the accretor, already roughly axisymmetric following the merger – our convergence criterion was achieved while the outer disk was still obviously non-axisymmetric. In equal-mass mergers, which are inherently more axisymmetric, completion also was too soon, before the densest material had reached the center of the remnant.

For the majority of our systems, however, the time required to reach 2.5% non-axisymmetry was roughly constant in units of the initial orbital period, at 6.1 ± 1.2 . For about the same time, axisymmetry was also achieved (by subjective visual inspection) for both dissimilar-mass mergers (except, in extreme dissimilar-mass cases, the outermost regions of their disks) and for equal-mass mergers (where the densest material had reached the center). We therefore use 6 orbital periods of the initial binary as the completion time of our simulations. In Sec. 2.4.4, we discuss the effect of continuing our simulations for 2 further orbital periods.

2.3 Results

With our 48 simulated mergers in hand, we try to determine scaling relations of global quantities such as the remnant and disk mass, highest temperature, etc., and look for homologies in the remnant profiles. For our analysis, we use a cylindrical (ω, ϕ, z) coordinate system centered on the remnant core. Properties on the equatorial (ω, ϕ) plane – defined as the original orbital plane – are averaged over ϕ using particles within $\frac{1}{2}h_z$ of the equatorial plane, where h_z is the remnant’s rotational axis ($\omega = 0$) central scaleheight (see Sec. 2.3.2). Properties along the rotational (z) axis are averaged within a cylinder $\omega < \frac{1}{2}h_z$. We use $\frac{1}{10}h_z$ as the bin size along both the equatorial plane and rotational axis. We determine properties mostly as a function of enclosed mass $M(r)$, which we define spherically³. Thus, we show, e.g., equatorial plane temperature $T(\omega)$ as a function of $M(r = \omega)$, the mass enclosed within a sphere with radius $r = \omega$.

2.3.1 Representative Mergers

As found for previous simulations, qualitatively the most important factor controlling the merger outcome is whether the WD masses are “dissimilar” or “similar”. In the former case, where the donor is significantly less massive than the accretor, only the donor overflows its Roche lobe,⁴ is disrupted, and accretes onto the accretor. The accreted material is heated on impact, lifting degeneracy. Hence, the merger remnant consists of a partly non-degenerate hot envelope and small, thick sub-Keplerian disk, both surrounding a cold core containing the largely unaffected accretor.

³Arguably, enclosed mass is more properly defined within equipotential surfaces, but this makes comparison with other simulations harder. For dissimilar-mass mergers, the difference is slight.

⁴The lower mass WD is larger and thus always fills its (smaller) Roche lobe first.

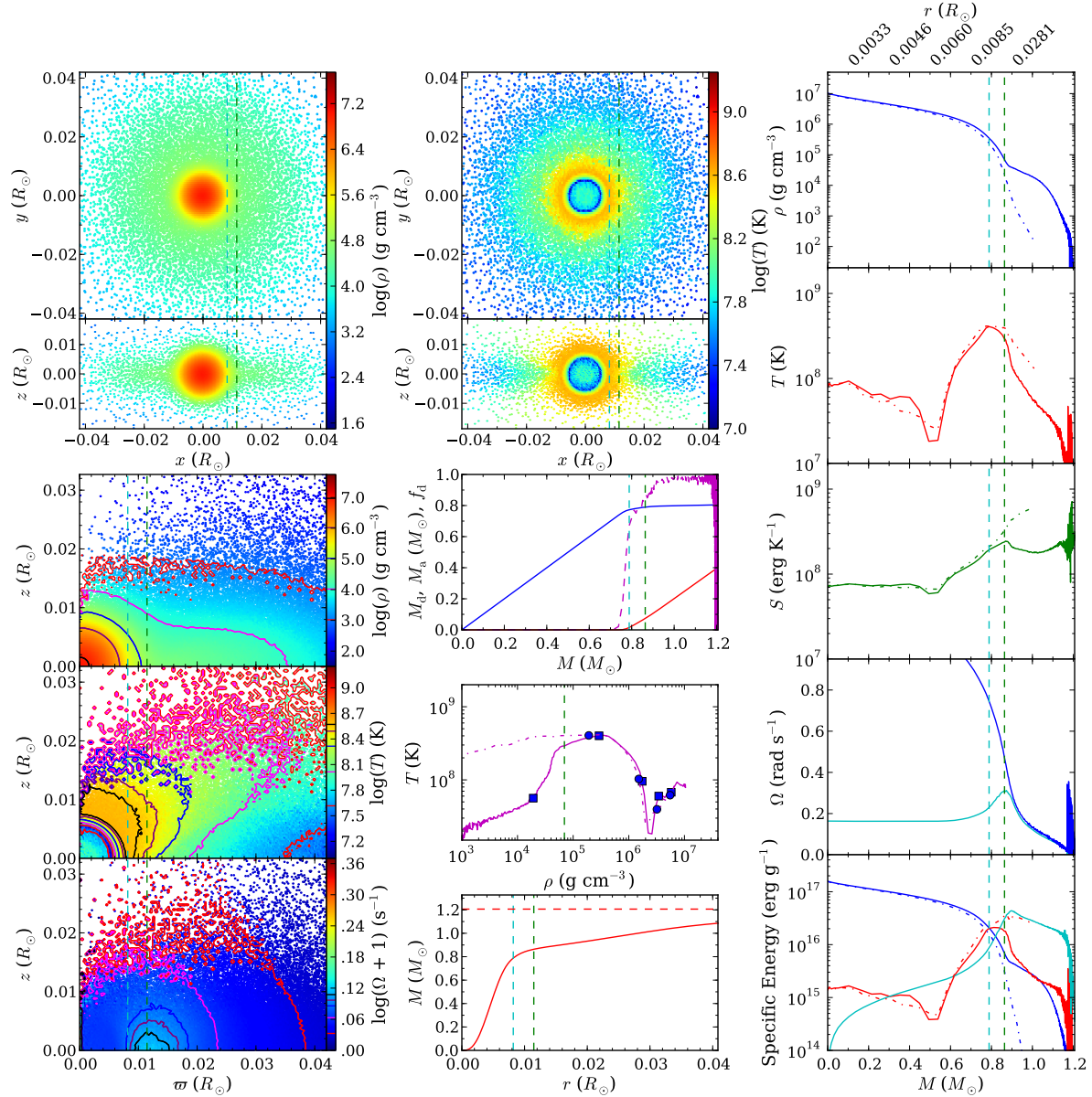


Figure 2.1: Structure of a $0.4 - 0.8 M_{\odot}$ merger remnant, representing the general outcome of a merger of white dwarfs with dissimilar mass. Upper left and middle – binned maps of density ρ and temperature T along slices in the xy and xz -planes. Lower left – binned maps and contours of density, temperature, and angular frequency Ω in the (ω, z) plane, averaged over cylindrical coordinate ϕ and over $\pm z$ (with 1 added to Ω to avoid problems with the logarithmic intensity scale). Middle – enclosed masses of donor and accretor material M_{d} and M_{a} (solid red and blue, resp.), and fraction of donor material f_{d} at a particular mass shell (dashed magenta). Middle, one but lowest – temperature-density profile with enclosed masses in $0.2 M_{\odot}$ increments indicated, both along the equatorial plane (solid curve, squares) and along the rotational axis (dot-dashed curve, circles). Middle, bottom – enclosed mass as a function of r , with the total mass indicated by the horizontal dashed red line. Right-hand column, top to bottom - density, temperature, entropy, angular (cyan) and Keplerian (blue) frequency, and degeneracy (blue), thermal (red) and rotational (cyan) specific energies as a function of enclosed mass M , both along the equatorial plane and along the rotational axis (solid and dot-dashed curves, respectively). In all graphs, the start of the disk (where the centrifugal acceleration equals half the gravitational one) and the equatorial radius (or mass enclosed within) of maximum temperature are marked by vertical green and blue dashed lines, respectively. [See the electronic edition of the Journal for Figs. 1.1–1.48.]

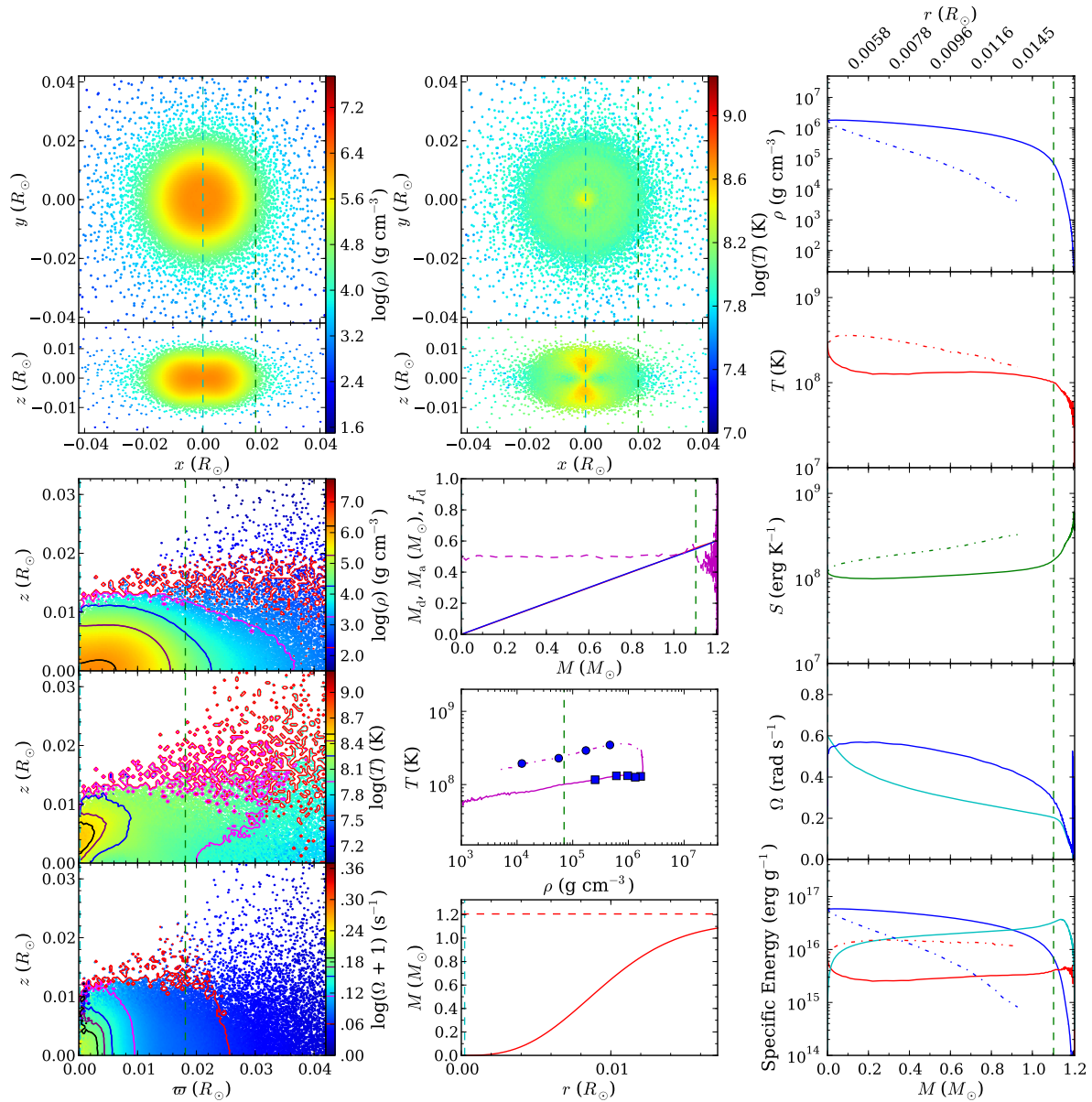


Figure 2.2: As Fig. Set 2.1, but for a $0.6 - 0.6 M_{\odot}$ merger remnant, representing the general outcome of a similar-mass merger.

In the latter case of a similar-mass merger, there is a large degree of mixing between the two stars. For exactly equal masses, both stars are disrupted simultaneously, and their accretion streams impact each other near the system's barycenter. Material from the centers of both stars initially forms a thick, cold, dense torus orbiting the barycenter; this torus slowly shrinks due to viscous drag, pushing the accretion stream material above and below the equatorial plane. When the stars have slightly different mass, the lower-mass one disrupts first, forming an accretion stream (or series of streams) that mixes with accretor material down to the center of the accretor (regardless of whether or not the other also disrupts).

We show the differences between similar and dissimilar-mass merger remnants using two representative examples in Figs. 2.1 and 2.2: a $0.4 - 0.8 M_{\odot}$ highly dissimilar and a $0.6 - 0.6 M_{\odot}$ equal-mass merger, respectively. One sees that the remnant morphologies are very different, consistent with previous work. The $0.4 - 0.8 M_{\odot}$ merger features a cold, nearly non-rotating and thus spherically symmetric remnant core, surrounded by a hot envelope with roughly equal degeneracy and thermal support, which itself is surrounded on the equatorial plane by a rotationally supported non-degenerate thick disk that holds most of the angular momentum. The accretor forms the core, largely undisturbed by the merger, while the envelope and disk are composed almost entirely out of donor material. The hottest points are on the interface between the core and the envelope.⁵ The $0.6 - 0.6 M_{\odot}$ remnant, on the other hand, has a massive, hot, partly rotationally supported and thus ellipsoidal core, and a very small but thick disk, both of which consist of material from both stars. No distinct envelope is formed. The hottest points are within the remnant core, just above and below the equatorial plane, arising from accretion stream material pushed out by the shrinking dense torus.

A good way to visualize how mergers transition between dissimilar and similar-mass is to look at changes in the remnant properties with varying donor mass. In Fig. 2.3, we show curves for accretors of 0.65 (left) and $1.0 M_{\odot}$ (right). One sees that remnants of highly dissimilar-mass mergers, with mass ratio $q_m \equiv M_d/M_a \lesssim 0.5$, have properties resembling the $0.4 - 0.8 M_{\odot}$ merger: their donor and accretor barely mixed, their temperature curves have off-center hot plateaus, and their angular velocity profiles feature an off-center bump. The equal-mass, $q_m = 1$ cases resemble the $0.6 - 0.6 M_{\odot}$ remnant: they have flat temperature profiles and centrally peaked angular velocity profiles. Intermediate cases have intermediate profiles, with the bumps in the temperature and angular velocity profiles widening with increasing q_m . The $0.4 - 0.8 M_{\odot}$ and $0.6 - 0.6 M_{\odot}$ remnants therefore lie at the extremes of what merger remnants look like.

The similarity between some of the curves for the 0.65 and $1.0 M_{\odot}$ accretors in Fig. 2.3 suggests a homology. The similarity is closest for mergers with the same mass difference ΔM , as can be seen in Fig. 2.4. For equal-mass mergers, all profiles are similar, simply scaled by a factor that depends on the total mass (except the $1.0 - 1.0 M_{\odot}$ merger; see below). As ΔM increases, the profiles are slightly less similar: with increasing total binary mass, the degree of mixing decreases, and the temperature and angular velocity maxima drift to slightly lower fractional enclosed mass. Nevertheless, the profiles still resemble one another far more closely than they resemble curves with other ΔM . The same holds for profiles along the rotational axis.

It may seem surprising that the controlling parameter between these approximate homologies is the mass difference ΔM rather than the mass ratio q_m . Empirically, however, the case is clear: e.g., the $0.4 - 0.5$ (second column, yellow) and $0.8 - 1.0 M_{\odot}$ (third column, black) mergers have the same

⁵The higher temperatures near the core are spurious; see Sec. 2.4.6

q_m , but different ΔM , and their structures clearly differ from one another. The same is true for the 0.4 - 0.6 (third column, cyan) and 0.6 - 0.9 (fourth column, brown) M_\odot mergers. As we discuss below, the similarity of mergers of similar ΔM likely reflects the close relation between the ratio of central densities and mass difference.

Before discussing the homologies and trends further, we should note the one dramatic exception. The 1.0 - 1.0 M_\odot simulation differs fundamentally from its fellow $\Delta M = 0$ mergers. During the evolution of this system, unlike for all other equal-mass mergers, one WD was fully disrupted before the other, and as a result material from one star (arbitrarily designated the “donor” before the start of simulation, hence the “inverted” mixing profile in Figs. 2.3 and 2.4) preferentially resides near the center of the remnant. This system also often appears as an outlier in Sec. 2.3.2 below. The 0.9 - 0.9 M_\odot merger also did not have equal mixing between the two stars, though the difference is much smaller. Raskin et al. (2012) noticed the same effect in their simulations, and concluded it reflected the fact that more massive WDs are much more concentrated and therefore harder to disrupt. This seems a likely explanation.

2.3.2 Merger Trends

A major goal of our work is to establish how various global properties of the merger remnant, such as remnant core and disk mass, maximum temperature, and maximum angular velocity, vary as a function of accretor and donor mass. By quantifying these trends, we hope to help develop a parametrized model of merger remnants. Before discussing trends, however, we stress that they are necessarily *approximate* - second order effects, numerical noise and our choice of stopping time all affect the remnant properties. Moreover, while integrated values like total thermal energy do not fluctuate from timestep to timestep, values at specific points in the remnant do (as noted the following sections). For instance, the mass enclosed within the radius of peak equatorial temperature becomes ill-defined for similar-mass mergers because these have rather flat temperature profiles (Fig. 2.3). To partly mitigate these fluctuations, the values presented below were determined by averaging frames from the simulation over an eight second span, centered on the time corresponding to six orbits of the initial binary.

As might be expected from the approximate homologies described above, we found that many properties scaled well with ΔM . Of course, a scaling with a dimensional mass difference makes little sense; we believe its success reflects the fact that over the range of $0.4 - 1.0 M_\odot$, the central density ρ_c depends approximately exponentially on mass, with $\rho_c \simeq 3.3 \times 10^7 \text{ g cm}^{-3} \exp[5.64(M/M_\odot - 1)]$ (see Fig. 2.5). Hence, a given mass difference ΔM corresponds to a given ratio of central densities, $\rho_{c,d}/\rho_{c,a}$. As argued in Sec. 2.3.2, $\rho_{c,d}/\rho_{c,a}$ has a straightforward interpretation: it characterizes the degree of mixing between the donor and accretor. We therefore discuss trends as a function of $q_\rho \equiv \rho_{c,d}/\rho_{c,a}$ from hereon. Where necessary, we refer to the mass ratio as q_m .

What Constitutes Similar-Mass?

As q_ρ increases from a small value toward unity, the merger remnant’s morphology shifts from resembling Fig. 2.1 (dissimilar-mass) to resembling Fig. 2.2 (equal-mass). From Fig. 2.3, ones sees that there is no particular q_ρ at which one transitions from “dissimilar” to “similar.” Nevertheless, we can determine a rough critical value of q_ρ that separates mergers in which the core is largely unaffected from those in which it is changed significantly, a separation that likely affects the outcome

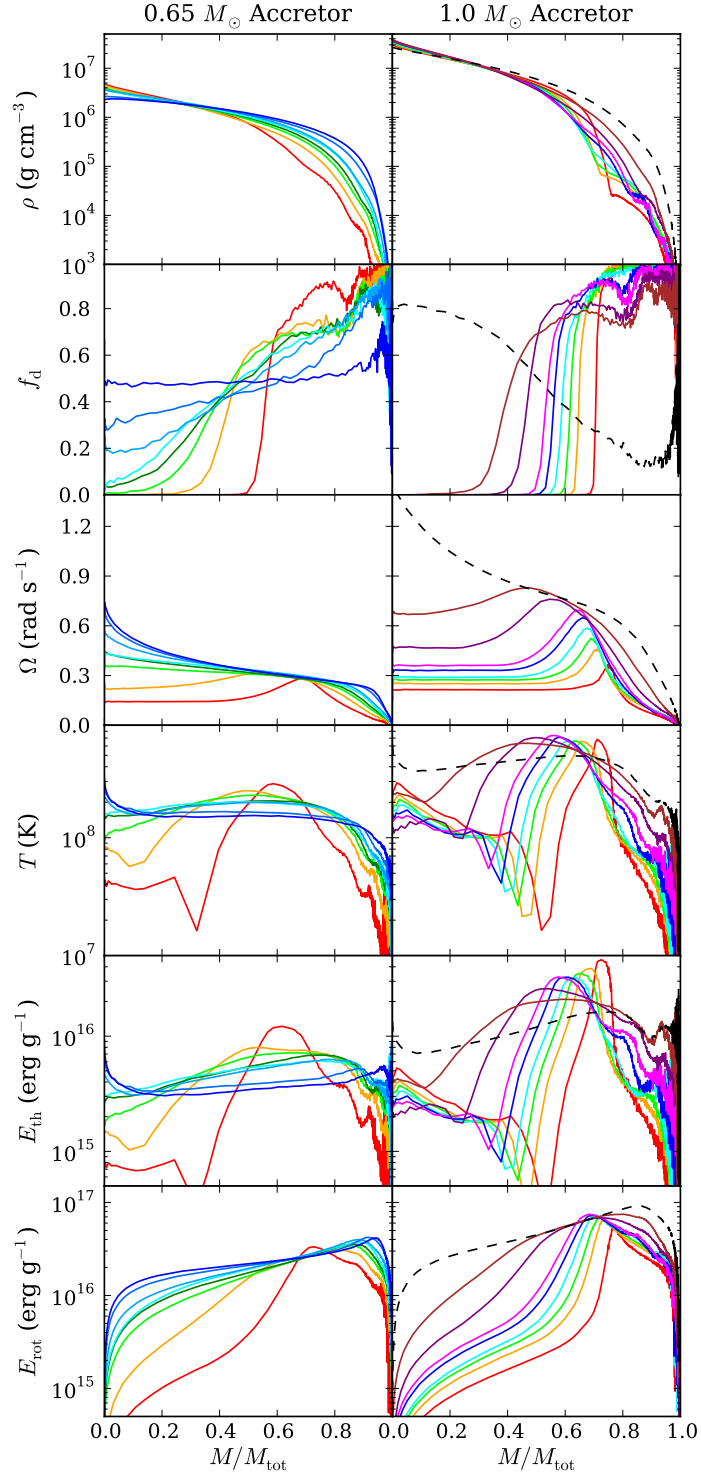


Figure 2.3: Properties of mergers with $0.65 M_{\odot}$ (left) and $1.0 M_{\odot}$ (right) accretors, for donor masses of 0.4 (red), 0.5 (orange), 0.55 (lime), 0.575 (green), 0.6 (cyan), 0.625 (light blue), 0.64 (blue), 0.65 (dark blue), 0.7 (magenta), 0.8 (purple), 0.9 (brown), and $1.0 M_{\odot}$ (black). Shown are, from top to bottom, density ρ , fraction of donor material f_d , angular frequency Ω , temperature T , specific thermal energy E_{th} , and specific rotational energy E_{rot} , all as a function of fractional enclosed mass M/M_{tot} . All properties are determined along the equatorial plane, except for f_d which is defined spherically. The $1.0 - 1.0 M_{\odot}$ merger (dashed black line) is an outlier; see text.

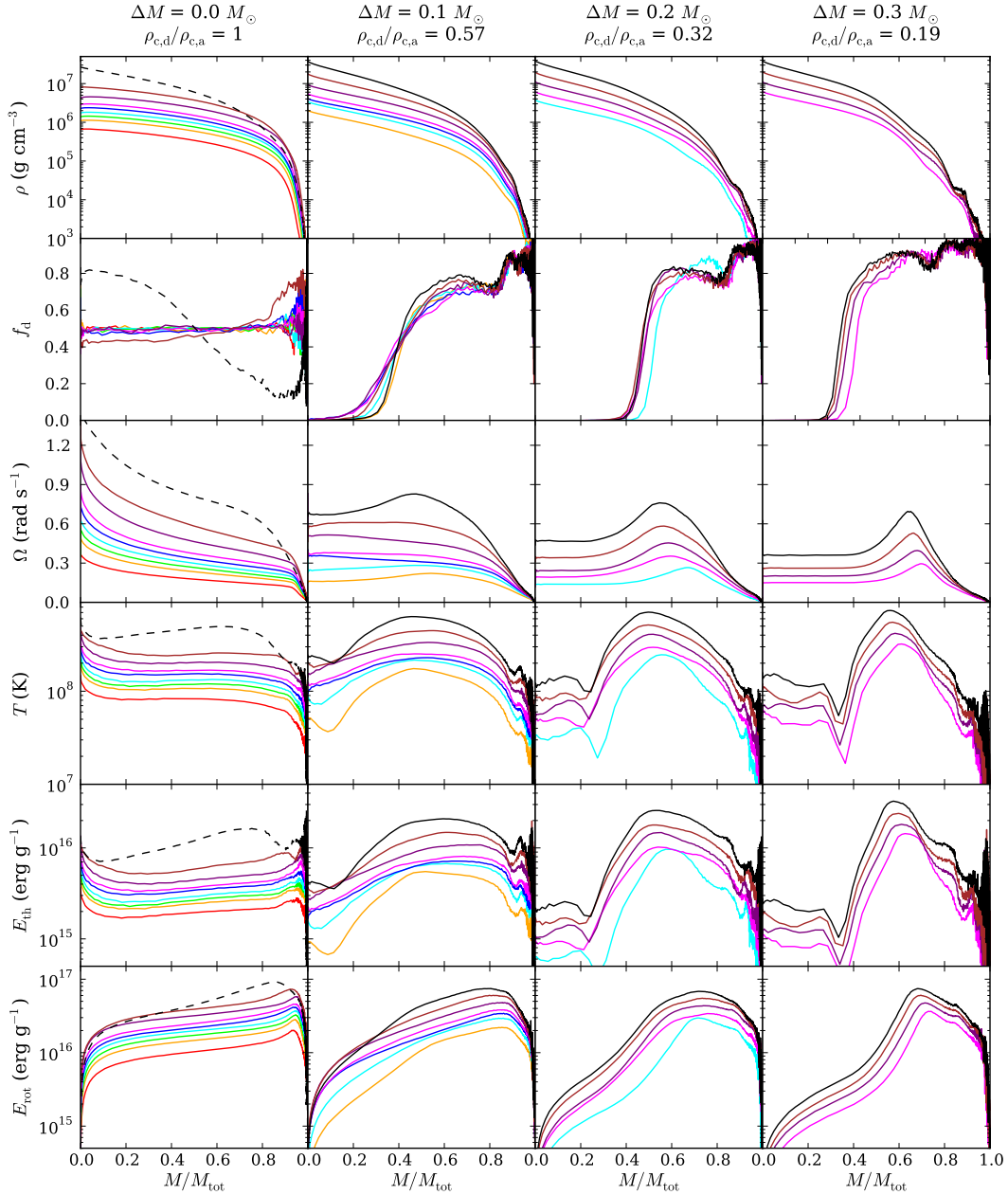


Figure 2.4: Dependence of the properties of mergers on mass difference, with, from left to right, $\Delta M \equiv M_a - M_d = 0.0, 0.1, 0.2$, and $0.3 M_\odot$ mergers. Properties shown, coloring, and line styles are as in Fig. 2.3, except color represents accretor mass.

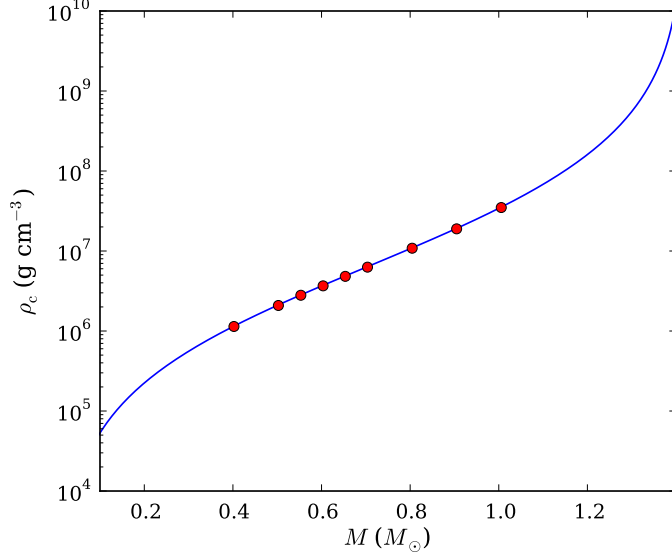


Figure 2.5: Relation between central density ρ_c and mass M for carbon-oxygen white dwarfs, showing both the results of relaxing white dwarf models in Gasoline (red points), and integrating hydrostatic equilibrium directly for spherically symmetric, non-rotating CO WDs with $T = 5 \times 10^6$ K (blue line). For the mass range considered, the central density depends roughly exponentially on mass.

of post-merger evolution.

To determine the critical value, we show in Fig. 2.6 the ratio of central to maximum temperature, T_c/T_{\max} , central to maximum angular velocity, Ω_c/Ω_{\max} , and the fraction of donor to accretor material within the central core, $(f_d/f_a)_{\text{cc}}$, where we define the central core as a sphere with radius h_z . All three properties are measures of the extent to which the core has been affected: mixed regions tend to be hotter and more spun up, and contain material from both stars.

From Fig. 2.6, one sees that Ω_c/Ω_{\max} approaches unity at $q_\rho \simeq 0.6$; at higher values, the angular velocity profile has a plateau or central peak rather than an off-center bump. Also at $q_\rho \simeq 0.6$, $(f_d/f_a)_{\text{cc}}$ starts to deviate from zero, i.e., donor material begins to penetrate the central core. The temperature points show the transition is not abrupt: T_c/T_{\max} starts to deviate from its downward trend (which reflects spurious heating in the most dissimilar-mass mergers; Sec. 2.4.6) around $q_\rho \simeq 0.3$ and continues to increase until $q_\rho = 1.0$; at $q_\rho \simeq 0.6$, $T_c/T_{\max} \simeq 0.5$. Overall, this suggests that while the dependence is gradual, the morphology changes most around $q_\rho \simeq 0.6$. This conclusion is confirmed by looking at the two-dimensional remnant temperature structures (Figs. 2.1 and 2.2). At $q_\rho \ll 0.6$, the remnant core has a large, spherically symmetric cold region, the nearly unperturbed accretor. This cold region shrinks with increasing q_ρ , and at $q_\rho \simeq 0.6$, spherical symmetry is broken. For still larger q_ρ , the cold region becomes a flat slice sandwiched between hotspots off the equatorial plane.

Given the above, we define “similar-mass” mergers as those with donor to accretor central density ratio $q_\rho > 0.6$, and “dissimilar-mass” mergers as those with $q_\rho < 0.6$. This critical density ratio corresponds to a mass difference $\Delta M \simeq 0.1 M_{\odot}$.

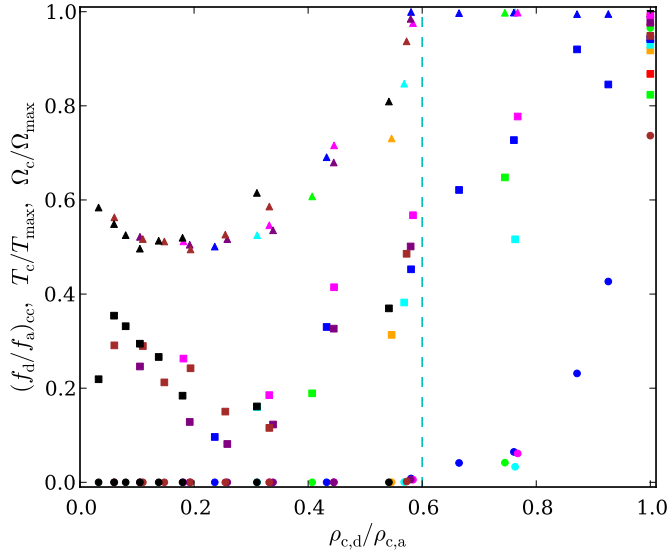


Figure 2.6: Dependence of merger core properties on the ratio of the donor and accretor central densities, $\rho_{c,d}/\rho_{c,a}$. Shown are the ratio of central to maximum temperature T_c/T_{\max} (squares), central to maximum angular velocity Ω_c/Ω_{\max} (triangles), and central core donor to accretor mass fraction $(f_d/f_a)_{cc}$ (circles), with colors representing different accretor masses, encoded as in Fig. 2.3. The vertical line marks $q_\rho \equiv \rho_{c,d}/\rho_{c,a} = 0.6$, where Ω_c/Ω_{\max} reaches unity, $(f_d/f_a)_{cc}$ becomes non-zero, and $T_c/T_{\max} \simeq 0.5$. We suggest it separates “dissimilar” from “similar” mass mergers.

Structural Trends

Here and in the following subsections of 2.3.2, we describe various trends of remnant properties in detail, hoping to help attempts to interpolate between different simulations and motivate analytical and semi-analytical depictions of the merger. Readers not requiring this level of detail may wish to skip to Sec. 2.3.3. We begin our discussion of trends with size and density parameters.

The rotational axis central scaleheight. We define the rotational axis central scaleheight h_z as the characteristic width σ of a Gaussian fit to the density distribution along the z axis at $\omega = 0$. h_z is a measure of the vertical extent of the remnant. We find that the ratio h_z/h_a , where h_a is the central scaleheight of the accretor, is reasonably well-approximated by,

$$\frac{h_z}{h_a} = 1.03 - 0.17 q_\rho^{1/2} \quad (\pm 0.02), \quad (2.1)$$

where the uncertainty listed in parentheses represents the root-mean-square (RMS) of the residuals around the approximation (see Fig. 2.7a). For highly dissimilar-mass mergers, h_z approximately equals the scaleheight of the accretor, while for similar-mass mergers, h_z is lower due to rotational support.

The vertical scaleheight increases with increasing ω : the scaleheight at the location of maximum temperature, $h(T_{\max})$, ranges from h_z to $1.21h_z$, and the scaleheight at maximum angular velocity $h(\Omega_{\max})$ ranges from h_z to $1.88h_z$. The prefactor for both heights increases with increasing accretor mass M_a and decreasing q_ρ .

The equatorial plane central scaleheight. Similar to h_z we define h_ω – the characteristic width of a Gaussian fit to the density distribution along the equatorial plane – as a measure of the equatorial extent of the remnant. The ratio h_ω/h_a can be parametrized by

$$\frac{h_\omega}{h_a} = 0.96 + 0.89q_\rho^2 \quad (\pm 0.08), \quad (2.2)$$

where we excluded the $1.0 - 1.0 M_\odot$ merger remnant for our fit (see Fig. 2.7a). The dependence on increasing q_ρ reflects the increased rotational support of the remnant core.

The central density of the remnant. The central density, ρ_c , is always within a factor two of the central density of the accretor, $\rho_{c,a}$. In Fig. 2.7b, one sees that for given accretor mass, $\rho_c/\rho_{c,a}$ increases with increasing q_ρ for highly dissimilar-mass mergers due to increasing compression of the remnant core, but begins to decrease because of increasing rotational support around $q_\rho \simeq 0.3$. We could not find a simple parametrization for these curves. Note that for some systems, as we continue running our simulations $\rho_c/\rho_{c,a}$ continues to increase. As discussed in Sec. 2.2.3, this is probably because artificial viscosity forces the merger remnant to undergo accelerated viscous evolution.

Mass Distributions

The merger mixes material between the donor and accretor. Here, we describe how this changes as a function of q_ρ , as well as how the material is distributed between the pressure-supported core and envelope and the rotationally supported disk.

The masses of the core-envelope and disk. We formally define the core-envelope as the part of the remnant inside the inner disk radius ω_{disk} , i.e., that is supported primarily by pressure (degeneracy for the core, thermal for the envelope) and not rotation. Since in every merger very little mass is ejected, a trend for either the core-envelope or the disk mass (M_{ce} and M_{disk} , resp.) suffices to determine both. The ratio of M_{ce} to the accretor mass M_a is well described by,

$$\frac{M_{\text{ce}}}{M_a} = 1 + 0.81q_\rho \quad (\pm 0.03), \quad (2.3)$$

if the $1.0 - 1.0 M_\odot$ merger is neglected, and the fit's y-intercept is forced to unity. See Fig. 2.8a.

(see the dashed green line in Figs. 2.1 and 2.2)

The mass enclosing 50% of the donor material. The further the donor penetrates, the smaller will be the mass enclosing half the donor's material, $M_{\text{enc}}(\frac{1}{2}M_d)$. For mergers with $q_\rho \lesssim 0.8$, $M_{\text{enc}}(\frac{1}{2}M_d)/M_a \simeq 1.30$, with an RMS residual of 0.03 (Fig. 2.8c). We present this trend mostly because we discuss similar thermodynamic and rotational enclosed masses, but it is somewhat difficult to interpret physically, since $M_{\text{enc}}(\frac{1}{2}M_d)$ increases with donor mass but decreases with mixing, which also depends on donor mass. The trend is easier to interpret using enclosed accretor mass rather enclosed total mass, as done below.

The accretor mass enclosing 50% of the donor material. As a different measure of the depth to which the donor penetrates, we consider just the accretor material within the mass enclosing half the

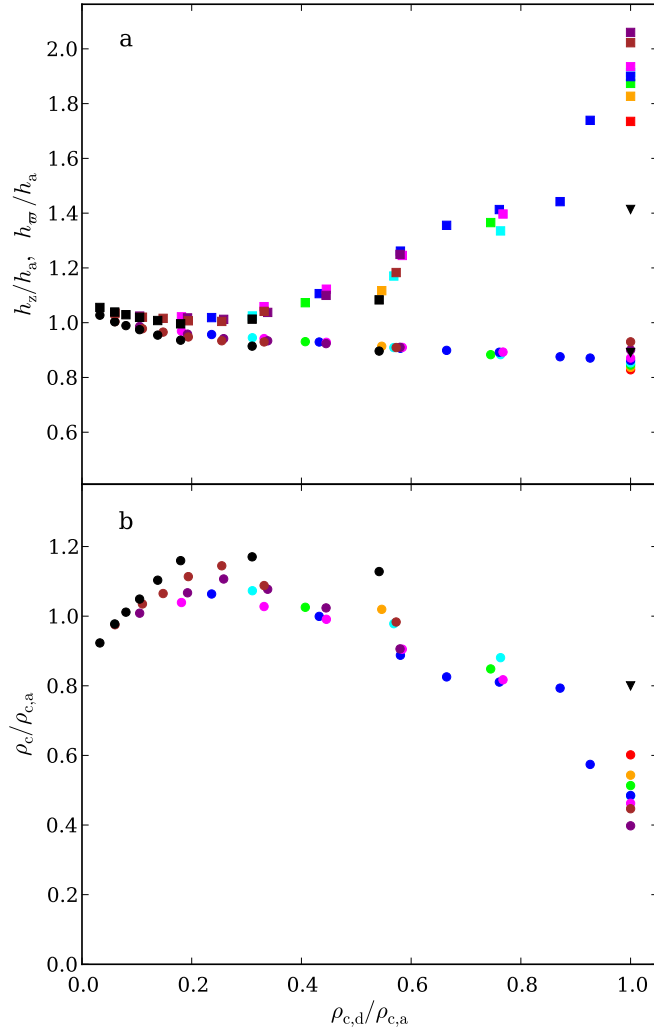


Figure 2.7: Structural properties of mergers. (a) Central scaleheights along the rotational axis (circles) and along the equatorial plane (squares) scaled to the scaleheight of the accretor, h_z/h_a and h_ω/h_a . (b) Central density of the merger remnant scaled to the central density of the accretor, $\rho_c/\rho_{c,a}$. Colors represent different accretor masses, encoded as in Fig. 2.3. Triangles represent the outlying $1.0 - 1.0 M_\odot$ merger.

donor, $M_{\text{enc}}(\frac{1}{2}M_d) - \frac{1}{2}M_d$. This should equal the accretor mass if the donor is deposited above the accretor, and half the accretor mass if the two stars are completely mixed. For $q_\rho \lesssim 0.8$, it can be approximated by (Fig. 2.8b),

$$\frac{M_{\text{enc}}(\frac{1}{2}M_d) - \frac{1}{2}M_d}{M_a} = 1 - 0.190q_\rho \quad (\pm 0.009), \quad (2.4)$$

where we forced the intercept to be unity. In this regime, roughly half of the donor remains outside of the accretor, though the trend discussed next indicates that the other half which does penetrate the accretor is spread across a much larger region at higher q_ρ . When $q_\rho \gtrsim 0.8$, the ratio drops sharply downward, indicative of the more thorough mixing expected for the similar-mass case. However, the existence and exact location of this drop may be a function of initial conditions (see Sect. 2.4.2).

The region over which the donor is spread. As a measure of the thickness of the region affected by the merger, we use the difference of the mass enclosing 75% of the donor material with that enclosing 25% of the donor material, i.e., $\Delta M_{\text{enc}}(M_d) = M_{\text{enc}}(\frac{3}{4}M_d) - M_{\text{enc}}(\frac{1}{4}M_d)$. Since 50% of the donor is within this range, $\Delta M_{\text{enc}}(M_d) - \frac{1}{2}M_d$ is a measure of the amount of accretor mixed with the donor. For $q_\rho \lesssim 0.8$, the ratio of the latter to the total accretor mass follows,

$$\frac{\Delta M_{\text{enc}}(M_d) - \frac{1}{2}M_d}{M_a} = 0.30q_\rho \quad (\pm 0.02), \quad (2.5)$$

while for $q_\rho \gtrsim 0.8$ the trend curls upward until it reaches 0.5, the value expected for completely mixed remnants. See Fig. 2.8d.

Combining the two above trends, we can formulate a qualitative picture of mixing. For $q_\rho \lesssim 0.8$, the donor can be thought of as being deposited onto the accretor and mixing with the accretor's outer layers, while for $q_\rho \gtrsim 0.8$, the accretor also disrupts substantially, leading to a regime where both stars mix more uniformly. The region over which the donor is spread, or thickness of the mixed layer, in both cases depends on q_ρ , which suggests that the relative densities of the donor and accretor govern mixing, i.e., the donor mixes significantly with all accretor material up to some fraction of the central density of the donor. Additional evidence of this will be seen in the thermodynamic trends below.

One might consider an alternate picture in which the donor dredges up a constant fraction of its own mass in accretor material. If this were the case, we would expect $(\Delta M_{\text{enc}}(M_d) - \frac{1}{2}M_d)/M_d$ to roughly be constant. Our results, however, show that for $q_\rho \lesssim 0.8$ this quantity is nearly a straight line that is close to zero for small q_ρ ($(\Delta M_{\text{enc}}(M_d) - \frac{1}{2}M_d)/M_d = 0.35q_\rho \pm 0.02$). This seems more consistent with mixing being determined by density.

Energy Balance

The energy balance of the remnants indicate their primary means of support. Since the remnants are virialized, we consider how the ratio of degeneracy, thermal, and rotational energy to the total internal energy of the remnants varies with q_ρ .

Energy balance of the entire remnant. The support against gravity changes from being due mostly to degeneracy pressure at low q_ρ to having a substantial rotational contribution at $q_\rho \simeq 1$. This is

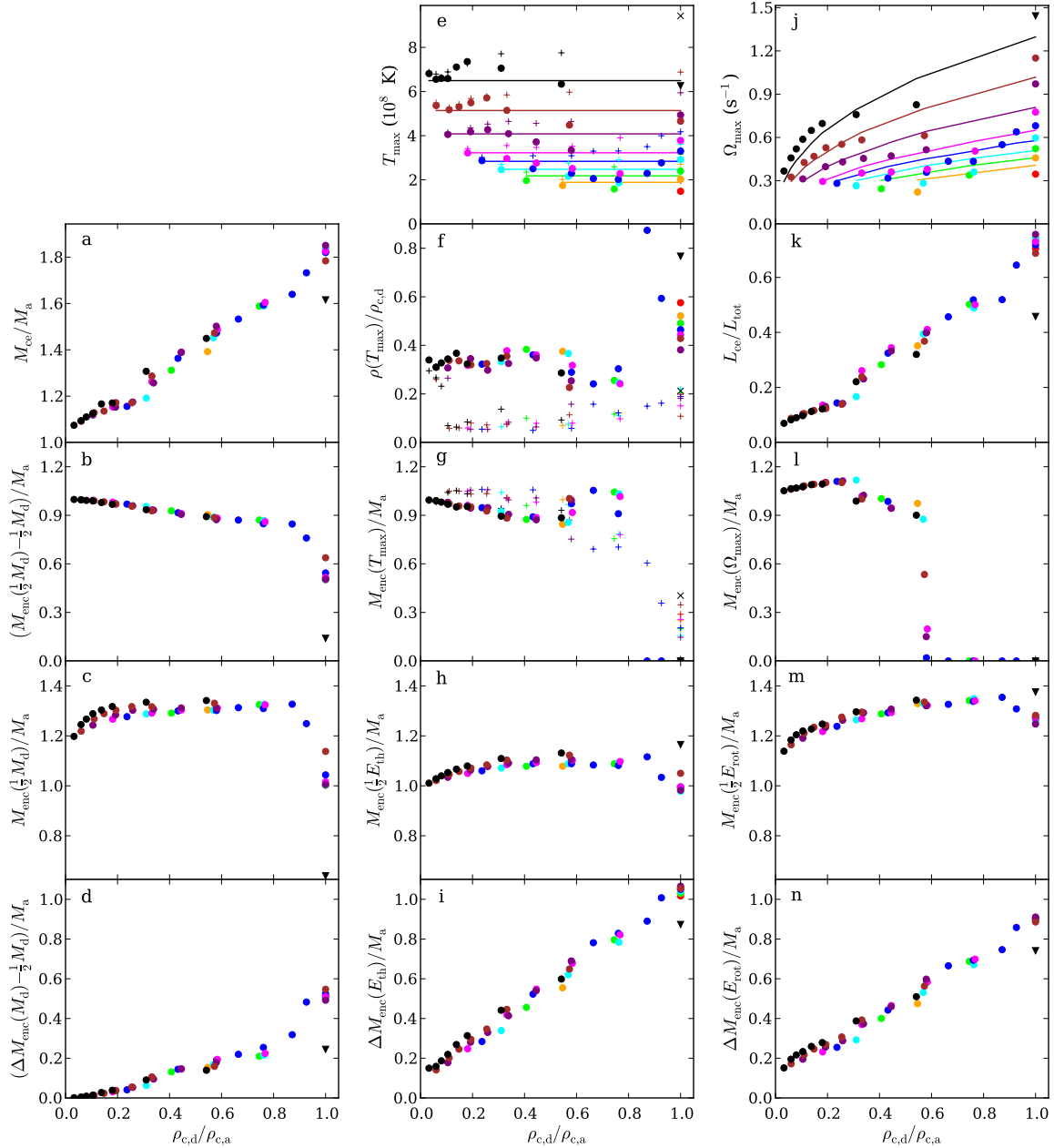


Figure 2.8: Mixing, heating, and spin-up (left to right) for mergers. (a) Scaled mass of the remnant core-envelope (where scaling here and below is to the accretor mass). (b) Fraction of the accretor within the mass enclosing half the donor mass. (c) Scaled remnant mass enclosing half the donor mass. (d) Fraction of the accretor mass within the region enclosing 25–75% of the donor mass. (e) Maximum equatorial temperature T_{max} (circles), with the approximation $T_{\text{max}} = 0.20GM_a m_p / k_B R_a$ overdrawn. Maximum temperatures along the rotational axis are shown with crosses. (f) Scaled density at the location of T_{max} (symbols as above). (g) Scaled mass enclosed within the radius of T_{max} (symbols as above). (h) Scaled mass enclosing half of the remnant thermal energy. (i) Scaled mass of the region enclosing 25 – 75% of the remnant thermal energy. (j) Maximum angular velocity Ω_{max} (circles) with best fit $\Omega_{\text{max}} = 3.8\Omega_{\text{orb}}$ overdrawn. (k) Fraction of the angular momentum in the core-envelope. (l) Scaled mass enclosed within the radius of maximum angular velocity. (m) Scaled mass enclosing half of the total remnant rotational energy. (n) Scaled mass of the region enclosing 25 – 75% of the remnant rotational energy. Colors represent different accretor masses, encoded as in Fig. 2.3. Triangles represent equatorial plane values, and x-marks rotational axis values, of the $1.0 - 1.0 M_\odot$ merger.

because for highly dissimilar-mass mergers most of the internal energy is locked up within the accretor, which is hardly heated or spun up. For similar-mass mergers, however, donor material mixes, to some degree, with the entire accretor, causing heating and spin-up throughout the entire remnant.

The total gravitational potential energy of the merger remnant can be described adequately by a constant fraction of GM_{tot}^2/R_a ,

$$\frac{-E_{\text{pot}}}{GM_{\text{tot}}^2/R_a} = 0.49 \quad (\pm 0.01). \quad (2.6)$$

From the virial theorem, the internal energy should be related to the potential energy by $3(\langle\gamma\rangle - 1)E_I = -E_{\text{pot}}$, where $\langle\gamma\rangle$ is an appropriately averaged equivalent to the adiabatic index. Since our remnants have cores where the electrons are becoming relativistic, one has $\langle\gamma\rangle$ somewhat smaller than $5/3$, especially for the more massive remnants. We find that the ratio $E_I/|E_{\text{pot}}|$ can be described by,

$$\frac{E_I}{|E_{\text{pot}}|} = 0.18 \frac{M_a}{M_\odot} + 0.42 \quad (\pm 0.01), \quad (2.7)$$

which is ~ 0.5 and ~ 0.6 for low and high M_a , respectively.

The fraction of the internal energy carried by degeneracy and rotation is fairly well described by,

$$\frac{E_{\text{rot}}}{E_I} = 0.31q_\rho^{1/2} \quad (\pm 0.01), \quad (2.8)$$

$$\frac{E_{\text{deg}}}{E_I} = 0.92 - 0.34q_\rho^{1/2} \quad (\pm 0.02). \quad (2.9)$$

With these, the fraction carried by thermal energy can also be calculated; as shown in Fig. 2.9a, the fraction in thermal energy first increases with increasing q_ρ , but turns over at $q_\rho \simeq 0.7$, decreasing afterwards. This reflects the competition between increased thermal energy from the two stars mixing, and increased rotational support from the spin-up of the core.

Overall, for highly dissimilar-mass mergers, the internal energy is partitioned into degeneracy, rotational and thermal energy with a ratio of approximately 8:1:1, reflecting that, as stated above, such mergers are almost entirely supported by degeneracy pressure. Similar-mass mergers, on the other hand, partition their internal energies with the ratio 6:3:1, i.e., rotational support is significant.

Energy balance of the core-envelope. Since the variations with q_ρ seen for the remnant as a whole are almost entirely due to variations in the core and envelope rather than in the disk, the trends we find for the core-envelope are very similar to those we found above for the entire remnant,

$$\frac{E_{\text{rot}}^{\text{ce}}}{E_I^{\text{ce}}} = 0.28q_\rho \quad (\pm 0.02), \quad (2.10)$$

$$\frac{E_{\text{deg}}^{\text{ce}}}{E_I^{\text{ce}}} = 0.94 - 0.32q_\rho \quad (\pm 0.02). \quad (2.11)$$

Note the dependency on q_ρ , rather than on $q_\rho^{1/2}$ as was found for the entire remnant. See Fig. 2.9b.

Energy balance of the disk. For the disk, we find very little dependence on q_ρ , consistent with the idea that most of the changes in the partitioning of energy have to do with increased mixing between the donor and accretor, which affects the core and envelope much more than the disk. Averaged over

all mergers, we find

$$\frac{E_{\text{rot}}^{\text{disk}}}{E_{\text{I}}^{\text{disk}}} = 0.74 \quad (\pm 0.03), \quad (2.12)$$

$$\frac{E_{\text{th}}^{\text{disk}}}{E_{\text{I}}^{\text{disk}}} = 0.19 \quad (\pm 0.02), \quad (2.13)$$

$$\frac{E_{\text{deg}}^{\text{disk}}}{E_{\text{I}}^{\text{disk}}} = 0.07 \quad (\pm 0.02). \quad (2.14)$$

Hence, the disk is composed of non-degenerate, primarily rotationally-supported material. See Fig. 2.9c. (Note that we do not try to define a ratio of internal to potential energy of the disk or core-envelope, since the potential energy of either is not straightforward to determine.)

Temperature and Thermal Energy

Since heating of the remnant is achieved through shocks and viscous dissipation, the most heavily mixed regions should also be the hottest. We focus on equatorial thermodynamic values, but consider the rotational axis as well for similar-mass mergers.

The maximum temperature. We find that the maximum temperature on the equatorial plane, T_{\max} , scales with the potential of the accretor (Fig. 2.8e),

$$\frac{kT_{\max}}{GM_{\text{a}}m_{\text{p}}/R_{\text{a}}} = 0.20 \quad (\pm 0.03). \quad (2.15)$$

This scaling is natural in the limit of highly dissimilar-mass merger – for each nucleon, of order $GM_{\text{a}}m_{\text{p}}/R_{\text{a}}$ is liberated and converted into thermal energy. The temperature and thermal energy profiles in Fig. 2.3 show that with increasing q_{ρ} , additional thermal energy is deposited into the remnant, but this energy is spread over a larger region, such that the maximum temperature remains roughly the same even as q_{ρ} approaches unity.

For a dissimilar-mass merger, the highest temperature along the rotational axis, T_{\max}^z , is found at the tenuous outer edge of the hot envelope. It is slightly higher than the maximum temperature found in the equatorial plane. With increasing q_{ρ} , however, the difference increases noticeably due to the two off-center hot spots found along the rotational axis in similar-mass mergers. Fitting T_{\max}^z , we find $kT_{\max}^z/(GM_{\text{a}}m_{\text{p}}/R_{\text{a}}) = 0.24 \pm 0.03$, though this does not capture the upturn for similar masses well.

All remnants with $q_{\rho} \gtrsim 0.8$ have convectively unstable cores along the equatorial plane. Artificially mixing these cores to make them isentropic decreases their maximum temperatures by 10 – 50% (not shown in Fig. 2.8, but see the left panel of Fig. 2.17). All remnants are stable against convection along the rotational axis.

The density at the point of maximum temperature. For dissimilar-mass mergers, the density at the hottest equatorial point, $\rho(T_{\max})$, depends mostly on the donor (see Fig. 2.8f). For $q_{\rho} \lesssim 0.5$, we find

$$\frac{\rho(T_{\max})}{\rho_{\text{c,d}}} = 0.34 \quad (\pm 0.02). \quad (2.16)$$

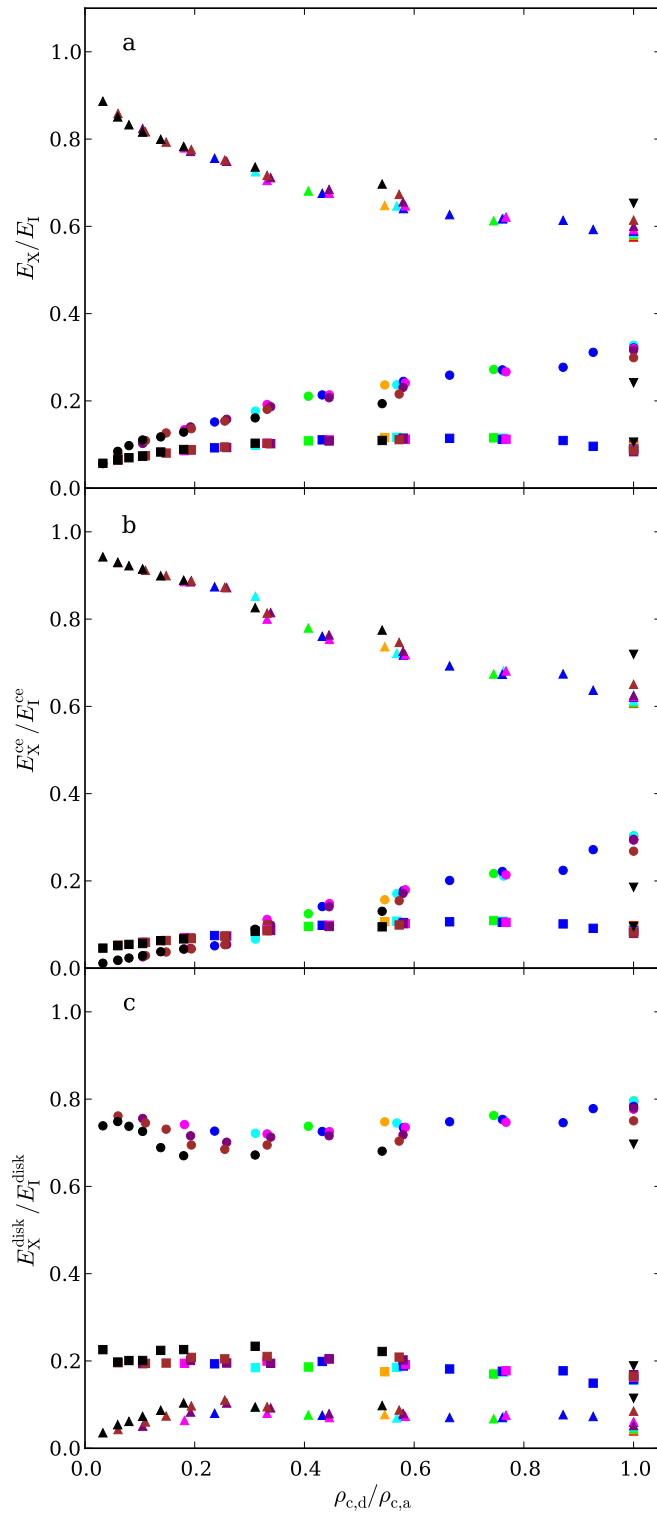


Figure 2.9: Partition of energies in (a) the overall merger remnant, (b) the remnant core plus envelope, and (c) the remnant disk. In each panel, the fraction of total energy carried in degeneracy (triangles), thermal (squares), and rotational (circles) energy is shown. Colors represent different accretor masses, encoded as in Fig. 2.3. Triangles represent the $1.0 - 1.0 M_\odot$ merger.

This proportionality again suggests that, at least for dissimilar-mass mergers, the donor mixes with the accretor up to a fraction of the central density of the donor, as alluded to earlier.

At $q_\rho \gtrsim 0.6$, the dependence becomes less obvious, with $\rho(T_{\max})$ varying from $\sim 25 - 90\%$ of $\rho_{c,d}$. Since for these density ratios, the donor material starts to penetrate the central core of the accretor – and the accretor starts to disrupt as well – the simple picture of the donor mixing up to a fraction of its own central density may be breaking down. Furthermore, part of the spread in density reflects that for high q_ρ the equatorial temperature profiles become nearly flat (see Fig. 2.3, left column), thus increasing the sensitivity to noise in the determination of the location (but not the value) of maximum temperature. This also affects our results for the enclosed mass, $M_{\text{enc}}(T_{\max})$, below.

Since for dissimilar-mass mergers, T_{\max}^z is located near the tenuous outermost regions of the hot envelope, where particle noise is high, the density at the point of maximum rotational axis temperature, $\rho(T_{\max}^z)$ (plus symbols in Fig. 2.8f), varies wildly between about $\rho(T_{\max})$ and one order of magnitude below $\rho(T_{\max})$. For similar-mass mergers, $\rho(T_{\max}^z)$ appears to be $\sim 20 - 50\%$ of $\rho(T_{\max})$.

The mass enclosed within the radius of maximum temperature. For dissimilar-mass mergers, the radius of maximum temperature occurs at an enclosed mass of $M_{\text{enc}}(T_{\max}) \simeq M_a$, while for mergers with $q_\rho \gtrsim 0.8$, maximum temperature occurs at the center and $M_{\text{enc}}(T_{\max}) \simeq 0$ (see Fig. 2.8g). For $q_\rho \lesssim 0.5$, we find

$$\frac{M_{\text{enc}}(T_{\max})}{M_a} = 1 - 0.28q_\rho \quad (\pm 0.01), \quad (2.17)$$

where the fit's y-intercept is forced to unity. Note that maximum temperature occurs near the bottom of the mixed zone, which is why $M_{\text{enc}}(T_{\max})$ is substantially smaller than $M_{\text{enc}}(\frac{1}{2}M_d)$. The reasons it starts to deviate from a tight trend at $q_\rho \simeq 0.6$ are the same as those for $\rho(T_{\max})$: the break-down of the simple mixing picture and the difficulty in determining the location of peak temperature for a broader plateau.

Since $M_{\text{enc}}(T_{\max}) < M_a$, it may be surprising that $\rho(T_{\max})$ is not higher than $\rho_{c,d}$. This is because the additional thermal and rotational support against gravity reduces the density gradient that would be required if degeneracy pressure were the only source of support.

For dissimilar-mass mergers, $M_{\text{enc}}(T_{\max}^z)$ is only slightly higher than $M_{\text{enc}}(T_{\max})$, since the remnant core is nearly spherically symmetric, apart from the fact that the hot envelope is slightly more extended in the vertical direction. For similar-mass mergers, the difference increases, reflecting the development of the off-center hot spots, until $M_{\text{enc}}(T_{\max}^z)/M_a \simeq 0.25$ for equal-mass mergers.

The mass enclosing half the remnant thermal energy. As a more robust measure of where thermal energy is deposited during the merger, we consider the mass enclosing half the remnant thermal energy, $M_{\text{enc}}(\frac{1}{2}E_{\text{th}})$ (see Fig. 2.8h). We find this is very close to the mass of the accretor,

$$\frac{M_{\text{enc}}(\frac{1}{2}E_{\text{th}})}{M_a} = 1.06 \quad (\pm 0.04), \quad (2.18)$$

if the $1.0 - 1.0 M_\odot$ merger is neglected. One sees turnovers at the extremes, for $q_\rho \lesssim 0.2$ and $q_\rho \gtrsim 0.8$. The former likely is because thermal energy is deposited into a narrow strip right on the surface of the accretor, while the latter is probably due to the disruption of the accretor.

While smaller than $M_{\text{enc}}(\frac{1}{2}M_d)$, $M_{\text{enc}}(\frac{1}{2}E_{\text{th}})$ is always larger than $M_{\text{enc}}(T_{\max})$. This reflects that

high density degenerate material has lower specific heat, so that for the same energy per unit mass the temperature is higher (see Fig. 2.3).

The width of the remnant thermal energy. The mass enclosed between the 25th and 75th percentiles of thermal energy, $\Delta M_{\text{enc}}(E_{\text{th}}) = M_{\text{enc}}(\frac{3}{4}E_{\text{th}}) - M_{\text{enc}}(\frac{1}{4}E_{\text{th}})$, is a measure of the extent of the remnant that has been heated (see Fig. 2.8i). Ignoring the 1.0 - 1.0 M_{\odot} merger, it can be fit by,

$$\frac{\Delta M_{\text{enc}}(E_{\text{th}})}{M_a} = 0.11 + 0.94q_{\rho} \quad (\pm 0.03). \quad (2.19)$$

Here, we did not force the y-intercept to go to zero, which is expected physically but gives a substantially poorer trend.

Angular Velocity and Rotational Energy

For a dissimilar-mass merger, the donor carries most of the angular momentum. As a result, the hot envelope contains more angular momentum and features higher angular velocities than the core, since the envelope is where most of the accreted donor material resides. Spin-up of the accretor is accomplished through shocks, PdV work and shearing forces. For a similar-mass merger, the two stars carry similar amounts of angular momentum and thoroughly mix. Conservation of angular momentum then implies that the entire remnant rotates rapidly.

The maximum angular velocity. On the equatorial plane, the highest angular velocity, Ω_{max} , scales linearly with the orbital angular velocity of the pre-merger binary, $\Omega_{\text{orb}} = 2\pi/P_{\text{orb}}$ (see Fig. 2.8j),

$$\frac{\Omega_{\text{max}}}{\Omega_{\text{orb}}} = 3.8 \quad (\pm 0.6). \quad (2.20)$$

The ratio of core-envelope to total angular momentum. For more similar-mass mergers, more angular momentum is deposited in the accretor and ends up in the core and envelope (see Fig. 2.8k). The ratio of core-envelope to total angular momentum, $L_{\text{ce}}/L_{\text{tot}}$, is approximately,

$$\frac{L_{\text{ce}}}{L_{\text{tot}}} = 0.70q_{\rho} \quad (\pm 0.03), \quad (2.21)$$

where we fit only for $q_{\rho} > 0.25$ and ignore the 1.0 - 1.0 M_{\odot} merger. For $q_{\rho} \lesssim 0.25$, the trend becomes shallower, resulting in a non-zero intercept. This suggests that even in cases where the donor has negligible mass some angular momentum is transferred to the accretor.

The mass enclosed inside the radius of maximum angular velocity. For dissimilar-mass mergers, both $M_{\text{enc}}(\Omega_{\text{max}})$ and $M_{\text{enc}}(T_{\text{max}})$ are about equal to M_a , with $M_{\text{enc}}(\Omega_{\text{max}})$ slightly larger than $M_{\text{enc}}(T_{\text{max}})$: for $q_{\rho} \lesssim 0.55$, $M_{\text{enc}}(\Omega_{\text{max}})/M_a = 1.05 \pm 0.06$. This is consistent with the idea that the hottest and most spun-up regions are those where the donor mixed most strongly with the accretor. For $q_{\rho} \simeq 0.6$, the off-center angular velocity peak is replaced by a plateau, and $M_{\text{enc}}(\Omega_{\text{max}})$ becomes ill-defined; for even larger q_{ρ} , the highest velocities occur in the center, and $M_{\text{enc}}(\Omega_{\text{max}}) \simeq 0$. See Fig. 2.8l.

The mass enclosing half the remnant rotational energy. Like for the thermal energy, for very dissimilar masses, the mass enclosing half the rotational energy, $M_{\text{enc}}(\frac{1}{2}E_{\text{rot}})$, is similar to the accretor mass (see Fig. 2.8m). For $q_\rho \lesssim 0.8$, we find

$$\frac{M_{\text{enc}}(\frac{1}{2}E_{\text{rot}})}{M_a} = 1.12 + 0.27q_\rho^{1/2} \quad (\pm 0.01) \quad (2.22)$$

Note that unlike $M_{\text{enc}}(\Omega_{\text{max}})$, $M_{\text{enc}}(\frac{1}{2}E_{\text{rot}})$ continues to increase with q_ρ (except for exactly equal-mass mergers), a consequence of particles with lower angular velocity but large lever arm that carry substantial rotational energy (see Fig. 2.3). Near $q_\rho \simeq 0.8$, the trend breaks as both stars are significantly disrupted. However, even exactly equal-mass mergers have more of their rotational energy stored in the outskirts (otherwise one would have $M_{\text{enc}}(\frac{1}{2}E_{\text{rot}})/M_a \simeq 1$).

The width of the remnant rotational energy. We measure the extent to which the remnant is affected by spin-up through the difference between the masses enclosing 25 and 75% of the rotational energy, $\Delta M_{\text{enc}}(E_{\text{rot}}) = M_{\text{enc}}(\frac{3}{4}E_{\text{rot}}) - M_{\text{enc}}(\frac{1}{4}E_{\text{rot}})$ (see Fig. 2.8n). Ignoring the $1.0 - 1.0 M_\odot$ merger, it is well-described by,

$$\frac{\Delta M_{\text{enc}}(E_{\text{rot}})}{M_a} = 0.12 + 0.77q_\rho \quad (\pm 0.03). \quad (2.23)$$

Like for the thermal energy, one sees that for more similar-mass mergers, rotational energy is spread more widely throughout the remnant.

2.3.3 A Qualitative Picture of the Merger

From our empirical results above, a qualitative picture of a merger emerges. A dissimilar-mass merger has the donor overflowing its Roche lobe and forming an accretion stream. This stream mixes with the accretor up to approximately the central density of the donor pre-merger, $\rho_{c,d}$. Those layers of the accretor that are denser than $\rho_{c,d}$ are hardly affected, and form the cold core of the merger remnant, while the mixed material will form a partly-thermally supported outer envelope, which somewhat compresses the core, as well as a rotationally supported disk.

At $q_\rho \gtrsim 0.6$, the above picture begins to break down, as portions of the donor start to penetrate to the center of the accretor. This results in substantial heating and spin-up of the central core: the merger becomes a similar-mass merger. As the masses become more similar, the distinction between donor and accretor is lost and both stars disrupt and form accretion streams. For all $q_\rho \gtrsim 0.6$, the remnants are similar: a large, ellipsoidal and partly rotationally supported hot core with two hotspots off the equatorial plane, surrounded by a small, hot disk.

For all mergers, the maximum temperature reached by dissipation of orbital energy is proportional to the accretor's gravitational potential energy. For increasing q_ρ , the maximum temperature remains similar, but the region over which the thermal energy is deposited widens. The density at maximum temperature is of the same order of magnitude as the central density of the donor, consistent with the mixing picture discussed above. The latter no longer holds for $q_\rho \gtrsim 0.6$, when the entire remnant is mixed and heated.

For a dissimilar-mass merger, the angular momentum remains in the outer regions, since most of it was originally carried by the donor. Angular momentum can be transferred between regions

through shocks, PdV work or shearing forces, all of which becomes increasingly important as the donor penetrates deeper. As a result, with increasing q_ρ , the remnant core is spun up further. Where both WDs disrupt, leading to colliding accretion streams, even the densest regions of the remnant have high rotational velocities.

2.4 Variation of Merger Parameters and Robustness of Results

In our parameter space study, we focused on the effects of varying the masses of the two WDs, fixing the initial separation a_0 , merger completion time criterion, and WD composition. To determine how robust our results are, we ran simulations varying these assumptions.

2.4.1 Changing the Composition

Ignoring fusion, WD mergers should be insensitive to changes in composition, since the dominant electron degeneracy pressure only depends on the mean molecular weight per electron, which is close to $\mu_e \simeq 2$ for all likely compositions. To confirm this, we ran simulations assuming pure helium and pure magnesium for an equal-mass case ($0.4 - 0.4 M_\odot$) and an dissimilar one ($0.4 - 0.8 M_\odot$). The results are shown in Figure 2.10. One sees that most quantities indeed have very similar profiles.

The set of profiles showing most variation are those of the temperature. These have similar shape, but different normalization. Since the thermal energy curves are very similar, it is clear that this reflects differences in heat capacity, which does depend on composition: for He composition, there are more (non-degenerate) ions than for our standard CO mixture, boosting the heat capacity (and thus lowering the temperature for given thermal energy), while for Mg composition, there are fewer, lowering the heat capacity (and increasing the temperature). As a result, the maximum equatorial plane temperatures for the $0.4 - 0.4 M_\odot$ simulations are 0.95, 1.48 and 1.68×10^8 K for He, CO, and Mg, respectively, while for the $0.4 - 0.8 M_\odot$ simulations, they are 2.92, 4.05, and 4.47×10^8 K.

The smaller differences seen for the other profiles reflect small differences in initial conditions. All WDs are constructed assuming $T = 5 \times 10^6$ K throughout, which implies more thermal energy for higher heat capacity. As a result, the relaxed He and Mg WDs are slightly larger and smaller, respectively, than the CO WD. These slight differences in radius translate into differences in initial separation, which in turn cause small differences in the angular velocity and rotational energy curves.

2.4.2 Varying the Initial Binary Separation

For our simulations, we chose an initial orbital separation a_0 for which a co-rotating donor would fill its Roche lobe. Since our (non-rotating) WDs are equilibrated in isolation, once the simulation starts they immediately begin to adjust to the tides and hence disrupt quickly. Ideally, one would allow them to adjust to the binary potential and start mass transfer properly. For non-synchronous rotation, however, this is not straightforward (see Sec. 2.5.2). Nevertheless, we try to get a sense of the influence of this by running simulations for two cases – $0.6 - 0.6 M_\odot$ and $0.6 - 0.8 M_\odot$ – with a_0 increased and decreased by 10% (see Fig. 2.11).

Our default simulations were considered complete at 6 orbits of the initial binary. For runs where a_0 was changed, we used 2.5% non-axisymmetry, and a requirement for the density to be highest at the

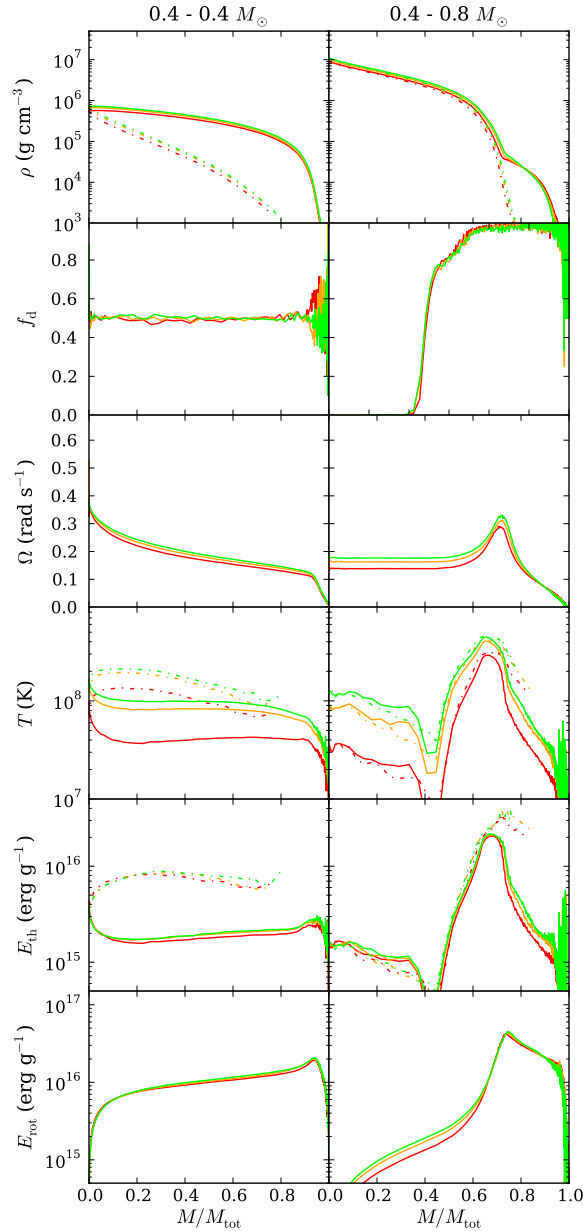


Figure 2.10: As Fig. 2.3, but for $0.4 - 0.4 M_{\odot}$ (left) and $0.4 - 0.8 M_{\odot}$ (right) mergers with different compositions: pure ${}^4\text{He}$ (red), CO (orange), and pure ${}^{24}\text{Mg}$ (lime). Dash-dotted lines represent profiles along the rotational axis rather than the equatorial plane.

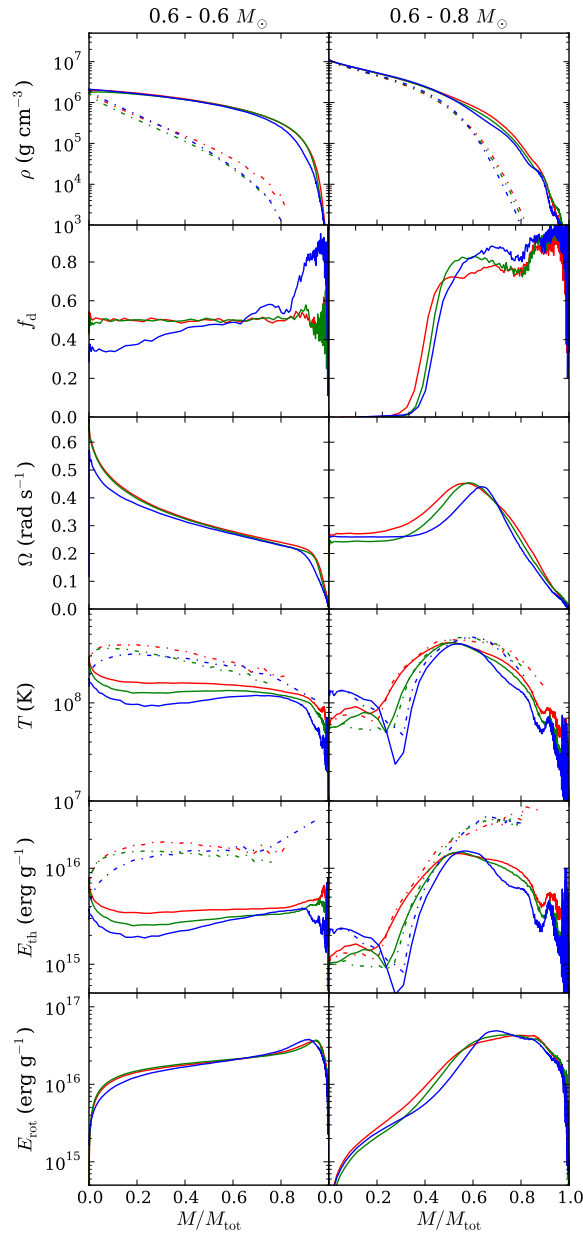


Figure 2.11: As Fig. 2.10, but for $0.6 - 0.6 M_{\odot}$ (left) and $0.6 - 0.8 M_{\odot}$ (right) mergers with varying initial orbital separation: 0.9 (red), 1.0 (green), and 1.1 (blue) times the value used for the parameter space study.

remnant's center, as the completion criteria⁶. Not surprisingly, runs with larger a_0 needed longer to achieve these criteria: with a 10% increase, the $0.6 - 0.8 M_{\odot}$ merger required 861 seconds, or ~ 15 orbits, to complete, while the one with a 10% decrease required 230 s, or ~ 5.5 orbits. Similarly, the $0.6 - 0.6 M_{\odot}$ merger with a 10% increase in a_0 required ~ 13 orbits (725 s) to complete, compared to the 7 orbits of a 10% decrease (283 s). In both cases, the increase simply reflects that it takes longer for the donor to be disrupted fully if a_0 is increased⁷. For instance, for the $0.6 - 0.8 M_{\odot}$ binary with increased separation, it took almost a dozen orbits before full disruption, while at the standard separation disruption occurred after just 1.5 orbits. This feature is of particular interest because for mergers of synchronously rotating WDs [Dan et al. \(2011; 2012\)](#) and [Raskin et al. \(2012\)](#) all note almost immediate disruption of the donor when approximate initial conditions are used, and much delayed disruption for more accurate initial conditions (up to ~ 30 orbits; see Sec. 2.5.2).

We find that the density profiles of the merger remnants are remarkably insensitive to varying a_0 (ρ_c changing by $\lesssim 2\%$ for the $0.6 - 0.8 M_{\odot}$ merger, and $\sim 20\%$ for the $0.6 - 0.6 M_{\odot}$ merger), and show substantial systematic changes only in the outer regions. The latter can be understood from the mixing and rotational profiles, where one sees that with increasing a_0 , donor material is mixed less deeply into the accretor, and rotational energy is shifted outward, causing the rotational frequency to peak at lower values and larger radii. This reflects the increase in angular momentum with increasing a_0 , which creates a more rotationally supported remnant (for both our systems, a 10% increase (decrease) in a_0 results in a 5% increase (decrease) in angular momentum). In the $0.6 - 0.8 M_{\odot}$ merger, the decreased mixing causes the accretor to be spun up less, thus lowering the rotational energy of the core, and narrowing the thermal energy plateau. These effects are also seen in the similar-mass case, where the center of the remnant receives less rotational support and becomes denser with increasing separation, and the mixing becomes less uniform.

Qualitatively, with increasing a_0 , the properties change in a way that is similar to the changes seen with decreasing q_{ρ} , i.e., similar to mergers with more dissimilar mass: reduced mixing, larger disks and less core rotational support, and shifts in the thermal and rotational energies toward larger radii. The converse is also true, decreasing a_0 has similar effects as increasing q_{ρ} , i.e., the mergers become similar to those with more equal masses. The changes are substantial at times: e.g. with a 10% increase in a_0 for the $0.6 - 0.6 M_{\odot}$ remnant, the maximum equatorial temperature is reduced by 40%, while the corresponding density increases by 25% (for the rotational axis hotspots, the values are a 13% and 30% reduction, respectively), and the mass of the disk increases by 65%. Similar, though far less extreme, changes are seen for the properties of the $0.6 - 0.8 M_{\odot}$ remnant. All this makes a_0 one of the parameters our mergers are most sensitive to.

2.4.3 Synchronization

In our simulations, the WDs have zero spin, i.e., we assume that tidal dissipation is too weak to synchronize their rotation. Whether or not this is correct is currently unknown, but to see what the effect could be, we ran simulations assuming synchronized rotation for $0.6 - 0.6 M_{\odot}$ and $0.6 - 0.8 M_{\odot}$ binaries (see Fig. 2.12). We used approximate initial conditions for these systems, identical to those of Sec. 2.2.2 except that the stars rotate at the orbital angular frequency.

⁶The 2.5% non-axisymmetry convergence time is 312 s (6.6 orbits) for our default $0.6 - 0.6 M_{\odot}$ run, and 250 s (5.2 orbits) for our default $0.6 - 0.8 M_{\odot}$ run.

⁷Of course, if placed far enough, the binary does not merge. For a $0.6 - 0.8 M_{\odot}$ binary, no mass transfer occurred within 500 s if a_0 was increased by 20%.

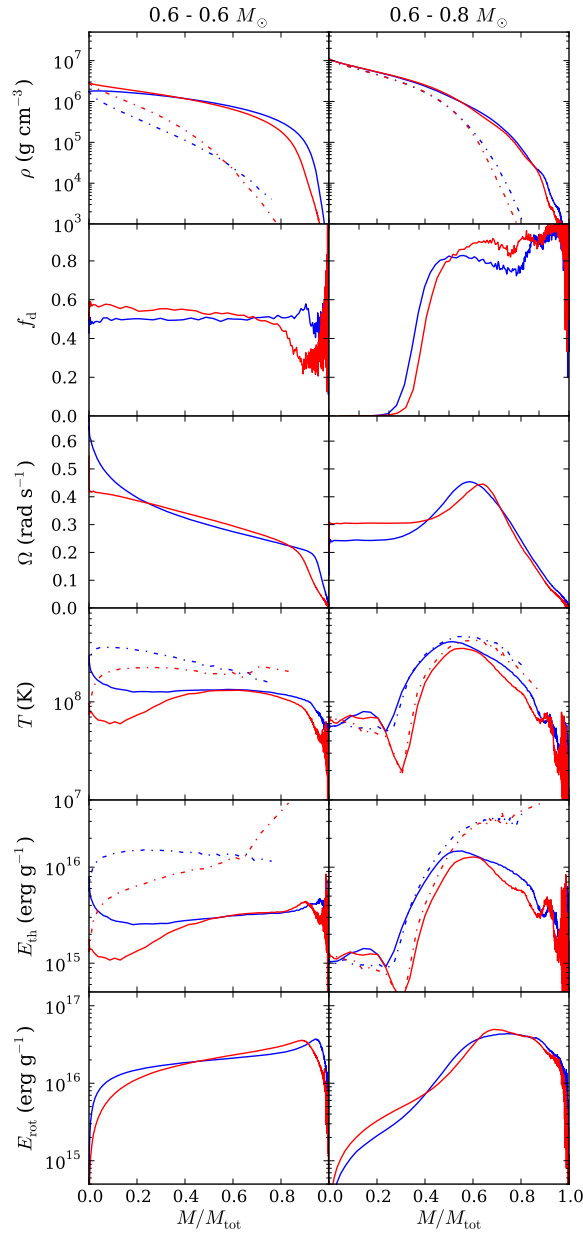


Figure 2.12: As Fig. 2.10, but for $0.6 - 0.6 M_{\odot}$ (left) and $0.6 - 0.8 M_{\odot}$ (right) mergers, comparing our default, irrotational case (blue) with that assuming synchronous rotation (red).

As in Sec. 2.4.2, our unsynchronized runs are from our parameter space study, and use 6 orbits as their completion criterion, while our synchronized runs use 2.5% non-axisymmetry, and a requirement for the density to be highest at the remnant’s center. Completion occurred at 407 s (~ 8.5 orbits) for the synchronized $0.6 - 0.6 M_{\odot}$ simulation, and 314 s (~ 6.5) orbits for the synchronized $0.6 - 0.8 M_{\odot}$.

The asynchronous and synchronous mergers differ mostly in the amount of heating and spin-up. This has two causes. First, for the synchronized binary, the total amount of angular momentum is about 10% larger, and high angular momentum material has more difficulty penetrating the accretor, as is evident in the $0.6 - 0.8 M_{\odot}$ mixing profile (because of the larger amount of angular momentum, the mergers also take about 1.5 orbits longer to achieve 2.5% non-axisymmetry). Second, in a synchronized binary, the donor and accretor have much less differential rotation with respect to each other, leading to much less spin-up and heating.

Both effects are largest for the equal-mass case. In particular, in a synchronized, equal-mass binary contact can occur without any friction, while in an unsynchronized one it involves shocks at the full orbital velocity. In consequence, for the synchronized case, rotational support is weaker in the center and stronger in the outskirts, causing the central density of our $0.6 - 0.6 M_{\odot}$ remnant to increase by $\sim 70\%$ and the disk mass to increase by a factor of 2. Furthermore, while for the non-synchronized case, the maximum temperature along the equatorial plane was found in the center, for the synchronized case it is found in the outskirts, and is more than a factor two lower (1.3×10^8 K instead of 2.9×10^8 K). The hotspots on the rotational axis also have much reduced temperature, 2.3×10^8 K instead of 3.6×10^8 K.

For the dissimilar-mass merger, the effects of synchronization are less dramatic: the accretor still spins up substantially, and rotational and thermal energy are deposited in roughly the same way. The main difference is that the synchronized case has slightly less mixing, causing a drop in total thermal energy and maximum temperature (from 4.1×10^8 K to 3.5×10^8 K on the equatorial plane, and from 4.6×10^8 K to 4.3×10^8 K on the rotational axis).

2.4.4 Running the Simulation Longer

We considered our mergers completed after 6 orbits, since in that time they on average had reached our convergence criterion of 2.5% non-axisymmetry (see Sec. 2.2.3). To test the robustness of our results, we also determined properties attained after 8 orbits. In Fig. 2.13, we compare the 6 and 8 orbit results for $0.6 - 0.6 M_{\odot}$ and $0.6 - 0.8 M_{\odot}$ binaries.

We find our mergers show little evolution between 6 and 8 orbits, with the largest changes seen for the angular velocity profiles. For the $0.6 - 0.8 M_{\odot}$ merger, the rigidly rotating core sped up and the off-center peak decreased in height and moved out, while for the $0.6 - 0.6 M_{\odot}$ merger, the center spun down and the rotational profile became flatter. In the dissimilar-mass merger, T_{\max} and $\rho(T_{\max})$ changed by $\lesssim 5\%$ and the density and temperature structures nearly overlap, while in the equal-mass merger T_{\max} and $\rho(T_{\max})$ changed by $\sim 20\%$ (2.9 to 2.3×10^8 K and 1.7 to 2.0×10^6 g cm $^{-3}$), reflecting an increase in central density and a shifting of the temperature profile, with temperature decreasing in the center but increasing elsewhere. The evolution of all properties is consistent with viscous evolution – expected to follow the merger proper – with the core driven into rigid rotation, and angular momentum transferred outward to the disk. In the dissimilar-mass merger, the net effect is spin-up of the core and spin-down of the envelope, while in the equal-mass case it is the reverse. Of course, in the process, rotational energy is turned into thermal energy, heating the remnants.

One curious aspect for equal-mass mergers is the evolution of the off-center hot spots (Fig. 2.2).

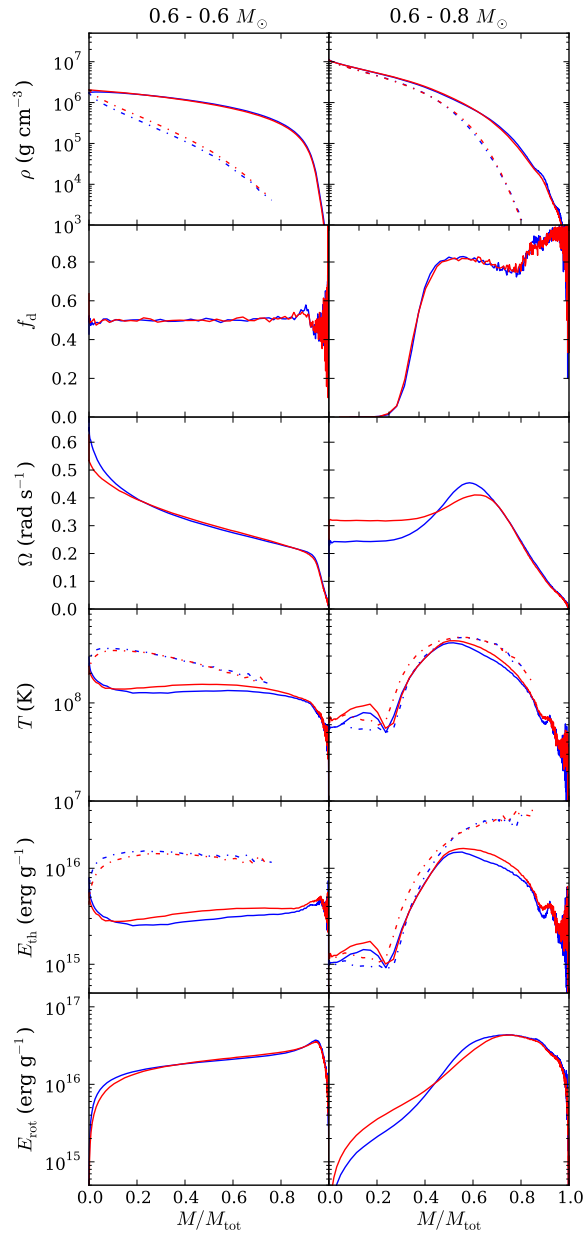


Figure 2.13: As Fig. 2.10, but for $0.6 - 0.6 M_{\odot}$ (left) and $0.6 - 0.8 M_{\odot}$ (right) mergers, comparing properties for our default simulation time of 6 initial orbital periods (blue) with those obtained after 8 orbital periods (red).

Over time, these broaden parallel to the equatorial plane, yet become narrower along the rotational axis. As a result, the hourglass shape is lost, and the center of the remnant stops being one of the hottest point in the system. After 8 orbits, the system resembles more closely what we find for typical similar-mass mergers, which have more pancake-shaped hot spots flanking a colder, denser region on the equatorial plane.

Comparing more broadly the 6 and 8-orbit results, we find changes at the $\sim 5\%$ level. The trends presented in Sec. 2.3.2 continue to hold to within $\sim 10\%$ except for h_ω (which becomes $h_\omega/h_a = 0.98 + 0.74q_\rho^2 (\pm 0.07)$), the fraction of disk energy in degeneracy energy ($E_{\text{deg,disk}}/E_{\text{L,disk}} = 0.07 (\pm 0.02)$), mass enclosed within the radius of maximum temperature ($M_{\text{enc}}(T_{\text{max}})/M_a = 1 - 0.21q_\rho (\pm 0.01)$), maximum rotational frequency ($\Omega_{\text{max}}/\Omega_{\text{orb}} = 3.4 (\pm 0.5)$) and the widths of the regions in which thermal and rotational energy are deposited ($\Delta M_{\text{enc}}(E_{\text{th}})/M_a = 0.13 + 0.87q_\rho (\pm 0.03)$; $\Delta M_{\text{enc}}(E_{\text{rot}})/M_a = 0.15 + 0.70q_\rho (\pm 0.02)$). Changes to these trends are consistent with the viscous evolution described above: the remnant is beginning to spin down, lose its rotational support, and energy is being redistributed.

2.4.5 Viscosity Prescription

The addition of artificial viscosity is required in SPH to accurately capture shocks, but no consensus exists on how best to implement it. We ran two additional simulations of a $0.6 - 0.8 M_\odot$ merger to check the robustness of our results with respect to changes in the viscosity, one with small and one with large artificial viscosity (fixed $(\alpha, \beta) = (0.05, 0.1)$ and $(1, 2)$, respectively). As before, these additional runs use 2.5% non-axisymmetry and a requirement for the density to be highest at the remnant's center as their completion criteria, and the low viscosity run completed at 198 s while the high completed at 242 s. Here, we expect that low values of α will lead to large particle noise and inaccurate shock capturing, while high values result in large viscous heating and rapid loss of differential rotation. Our results confirm this (Fig. 2.14): the simulation with low artificial viscosity leads to a remnant with stronger differential rotation, with the disk carrying 34% more rotational energy (and the remnant 33% less) than in the standard variable α simulation. Lower viscosity also leads to greater mixing of donor and accretor material, reflecting the stronger diffusion associated with the larger particle noise inherent to low viscosity.

Aside from the mixing and spin-up, the results for the three different viscosity prescriptions do not differ greatly. While one might have expected greater dissipation of rotational into thermal energy for higher viscosity, the maximum temperatures and rotation rates vary by $\lesssim 10\%$, and the thermal and rotational profiles are quite similar. The density profiles are virtually identical except near the outer parts, where the low viscosity simulation leaves matter with greater rotational support.

2.4.6 Spurious Heating

As discussed in Sec. 2.2.1 and throughout Sec. 2.3, noise combined with a pressure floor in the equation of state lead to small increases in internal energy. While this energy has a negligible effect on most remnant properties, in the most degenerate regions of the remnant it can cause significant temperature increases. Here, we discuss the extent to which spurious heating affects our results.

As a comparison for the spurious heating seen in some of the simulations, we relaxed a $0.8 M_\odot$ isolated white dwarf for 489 s longer than the standard 81 s we used for relaxing single stars. While the

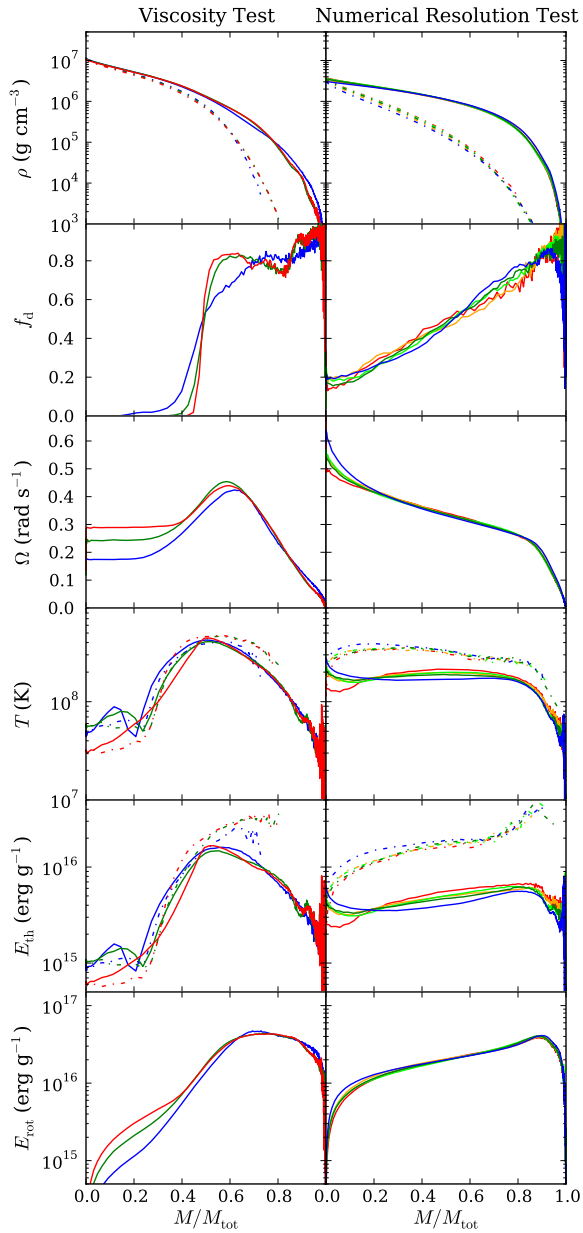


Figure 2.14: As Fig. 2.10, but comparing simulations of a $0.6 - 0.8 M_{\odot}$ merger with different viscosity prescriptions (left) and simulations of a $0.625 - 0.65 M_{\odot}$ merger with different numbers of particles (right). For the viscosity, we compare fixed low viscosity ($\alpha = 0.05, \beta = 0.1$; blue), standard variable viscosity (green), and fixed high viscosity ($\alpha = 1.0, \beta = 2.0$; red). For particle numbers, we show simulations at one quarter (red), half (orange), and double (blue) the default number of particles, as well as the default simulation (lime) and a rerun of the default simulation (green) to determine the effect of order-of-execution differences, round-off errors and other such numerical effects.

total energy of the WD (potential, degeneracy and thermal energy combined) increased by $\sim 1\%$ of the original total energy over the additional period of time, the change in thermal energy was enough to raise the central WD temperature from 1.2×10^7 K (increased from 5×10^6 K due to particle noise) to 1.2×10^8 K. In Fig. 2.15, we compare the thermal energy profile of this isolated $0.8 M_\odot$ WD with those of a $0.4 - 0.8 M_\odot$ and a $0.7 - 0.8 M_\odot$ merger, with the times for the isolated WD taken at 489 and 224 s (the mergers' respective completion times) longer than the standard 81 s. The total thermal energy generated in the WD at an additional 489 s is $\sim 10\%$ of the thermal energy generated in a $0.4 - 0.8 M_\odot$ merger.⁸ Indeed, given how well the specific thermal energy profiles match in the interior, it is clear that spurious heating dominates there.

Spurious heating is much less important for the $0.7 - 0.8 M_\odot$ merger, since its core has mixed to much greater extent and less time was needed for the merger to complete. The total thermal energy generated in the isolated WD at 224 s is only $\sim 3\%$ of the thermal energy generated during merger, and even at the very center spurious heating contributes $\sim 35\%$ (rather than nearly all) of the thermal energy. As a result, the central temperature of the merger, 1.4×10^8 K, is substantially higher than that of the isolated WD, 7.8×10^7 K. It is important to note this comparison overestimates spurious heating, since the isolated WD will have had many more particles that dip below the Fermi energy than the much hotter merger remnant core.

Overall, we conclude that spurious heating is present, but is recognized fairly easily and does not influence our conclusions. In particular, its effects on remnants should be small in both high-density regions with $T \gtrsim 3 \times 10^8$ K and in lower-density $\lesssim 10^6 \text{ g cm}^{-3}$ regions. Other simulations may suffer from spurious heating as well. In this respect, it is intriguing that our equatorial temperature curves for a $0.6 - 0.8 M_\odot$ merger are a good match those of LIG09, even in the center (Fig. 2.16; Sec. 2.5.1).

2.4.7 Resolution

To determine whether or not the numerical resolution matters for our results, we ran three additional simulations of a $0.625 - 0.65 M_\odot$ merger, with roughly a quarter, half, and double the number of particles (63,736, 127,525 and 510,047, respectively), corresponding to 0.63, 0.79 and 1.26 times the SPH smoothing length (resolution) we normally use. We also ran a second simulation with the same number of particles (255,035 particles). Here, we chose $0.625 - 0.65 M_\odot$ to see if numerical resolution has any effect on whether a merger is “similar-mass”. All simulations were considered complete at 6 orbits of the initial binary, though we also checked the 2.5% non-axisymmetry convergence times.

From Fig. 2.14, one sees that the two runs using the same number of particles – and identical initial conditions and the same version of Gasoline – still give slightly different results. This is due to the inherent non-linear nature of fluid dynamics, coupled with small, random perturbations, e.g., from differences in the order of force addition in parallel processing, round-off errors and slight inconsistencies in converting thermal energy to temperature. Overall, merger remnant properties change by $\sim 3.5\%$ between the two runs. The most prominent differences are seen in properties determined from low numbers of particles, such as T_c (varies by $\sim 10\%$), and those involving finding maxima of temperature plateaus, such as $\rho(T_{\max}^z)$ (40%) and $\rho(T_{\max}^{cv})$ (a factor of 3 – in one case convection shifts the temperature maximum off-center).

⁸A $\sim 10\%$ increase in thermal energy corresponds to $\sim 1\%$ increase in the overall energy of the $0.4 - 0.8 M_\odot$ remnant, somewhat larger than the typical $\sim 0.3\%$ level at which Gasoline conserves total energy in our simulations. We find that similar-mass simulations tend to lose total energy at the 0.05% level, while some of the low q_ρ mergers gain more than 1% in total energy due to spurious heating.

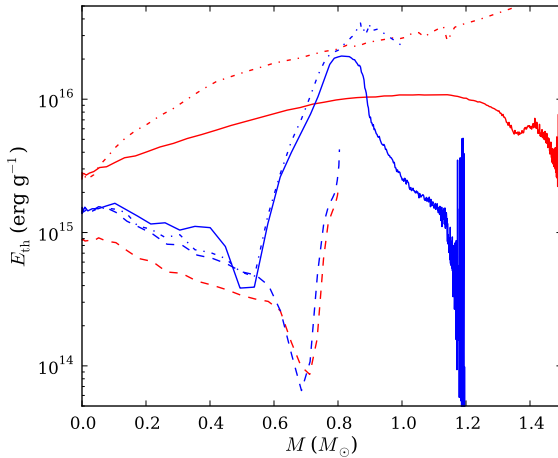


Figure 2.15: Specific thermal energy as a function of enclosed mass for a $0.4 - 0.8 M_{\odot}$ (blue) and a $0.7 - 0.8 M_{\odot}$ merger (red), shown both along the equatorial plane (solid curves) and along the rotational axis (dot-dashed). Also shown are the (spherical) profiles found for an isolated $0.8 M_{\odot}$ white dwarf (dashed) simulated using the same parameters, and for the same completion times (six initial orbital periods, equivalent to 489 s and 224 s). Spurious heating is estimated to be responsible for nearly all the thermal energy in the core of the $0.4 - 0.8 M_{\odot}$ remnant, and for about one third in the core of the $0.7 - 0.8 M_{\odot}$ remnant. It is not important in regions heated by interaction. (The “hook” in the outer layers of the white dwarf profile reflects the high initial temperature chosen; in a merger, this is erased by the interaction.)

The differences for different resolutions are larger. While to first order, the equatorial density and mixing profiles are very similar, there is a systematic $\sim 20\%$ drop in the equatorial density – $\sim 25\%$ in the rotational axis density – near the center of the remnant with increasing numerical resolution (top right panel of Fig. 2.14). The angular velocity and rotational energy profiles are again very similar, except in the central regions, where there is a $\sim 20\%$ increase in Ω_{\max} . For the temperature the effects are larger: with higher resolutions, most of the equatorial plane is colder, with a $\sim 20\%$ drop in the value of the temperature plateau near $M/M_{\text{tot}} = 0.5$. The temperatures along the rotational axis, however, increase with increasing resolution, by $\sim 10\%$ across the range of resolutions, as does the upturn in equatorial temperature near the center of the remnant, by $\sim 50\%$ ($\sim 30\%$ if we do not include the lowest resolution run). The latter effects are due to increasing prominence of the off-center hotspots at higher resolutions, which also tend to look more hourglass-shaped. Indeed, for our lowest resolution, the densest material in the two stars remains relatively cold throughout the entire merger, resembling the synchronized systems described in Sec. 2.4.3. Finally, we find that if we do not consider the lowest resolution run, the disk half-mass radius varies by 4%, angular velocity at the half-mass radius varies by 4%, and the core-envelope mass changes by 3%. This is similar to the results of the resolution tests of Raskin et al. (2012).

The 2.5% non-axisymmetry convergence times for the half and double-particle number runs are within 14 s of the 275 s non-axisymmetry convergence time of the default run, a small difference that implies a negligible amount of post-merger evolution. Only the quarter-particle number run deviated substantially, converging 57 s earlier. This may simply reflect the smaller number of particles in the disk, where the system is most asymmetric.

We stress that even though the order-of-magnitude change in particle number (factor of two change in resolution) generates 10 – 30% variations in some remnant properties, the overall shapes of the profiles in Fig. 2.14 are very similar. In particular, the merger remnant does not look more or less “similar-mass” (except, arguably, the temperature curve at the lowest resolution). Exact values of properties, therefore, will vary depending on resolution (and will vary on similar or larger levels if initial conditions like a_0 are changed), but the overall picture of the merger and trends should be more robust.

2.5 Comparison With Others

2.5.1 Comparison With Lorén-Aguilar et al. (2009)

[LIG09](#) simulated a number of WD mergers, and gave detailed temperature, surface density, and rotational frequency curves for three. In Fig. 2.16, we compare their results (from their Figs. 3 and 4) with ours for two of these, $0.6 - 0.6 M_{\odot}$ and $0.6 - 0.8 M_{\odot}$ (the third was a $0.4 - 0.8 M_{\odot}$ He - CO WD merger, whose temperature profile cannot be compared directly). We note that they used different initial conditions, starting their systems with an orbital separation too large for mass transfer to begin, and then slowly reducing the separation until it does. This point defines their $t = 0$ and the start of the merger simulation proper. Given this different setup, their merger completion times cannot be compared directly to ours. In their simulations, however, coalescence (the final consolidation of the two WDs into one) also occurs after just about one orbit, so the differences should not be too large. To give a sense of the effect of different completion criteria, we compare their results both with our standard results, taken after 6 orbits, and our results taken at their merger completion times.

For both mergers, the surface density curves are similar, although in their $0.6 - 0.6 M_{\odot}$ merger, the central peak is $\sim 30\%$ higher ($\sim 10\%$ if we use their completion time of 514 s). For the $0.6 - 0.8 M_{\odot}$ merger, the temperature profiles are also very similar, with maxima⁹ differing by only $\sim 10 - 15\%$, and having nearly identical shapes. Larger differences are seen for the $0.6 - 0.8 M_{\odot}$ rotational frequency profile, where the angular velocity peaks further out and at lower value ($\sim 0.3 \text{ s}^{-1}$ compared to our 0.45 s^{-1} – or 0.50 s^{-1} using their completion time of 164 s). Indeed, our entire remnant is more spun-up than theirs.

For the $0.6 - 0.6 M_{\odot}$ merger, [LIG09](#) have a plateau in their angular frequency profile, with $\Omega_{\max} \simeq 0.25 \text{ s}^{-1}$, while our profile is much more peaked and reaches a much higher frequency, of 0.60 s^{-1} . By their completion time, our rotation curve is not as sharply peaked, but still reaches 0.44 s^{-1} . The temperature profiles are also much less similar: our maximum temperature in the equatorial plane is a factor of 2 lower than theirs (factor of 3.3 at their completion time), and even our maximum temperature along the rotational axis is a factor 1.6 lower (factor 1.9 at their completion time).

Finally, we can compare how mass is distributed. In both our simulations and those of [LIG09](#), negligible mass is lost, so only the distribution between disk and core-envelope matters. For our $0.4 - 0.8 M_{\odot}$, $0.6 - 0.6 M_{\odot}$, and $0.6 - 0.8 M_{\odot}$ simulations, we infer disk masses of 0.31 , 0.10 , and $0.40 M_{\odot}$, respectively, which are reasonably close to the 0.28 , 0.10 , and $0.30 M_{\odot}$, respectively, listed by [LIG09](#) (their Table 1), especially considering that we likely use a different definition of what is “disk”.

⁹Maximum temperatures given in Table 1 of [LIG09](#) refer to hot spots in their simulations, and are about a factor of 2 higher than the hottest points on their temperature curves. As we have not done hot-spot finding, we cannot compare with those values.

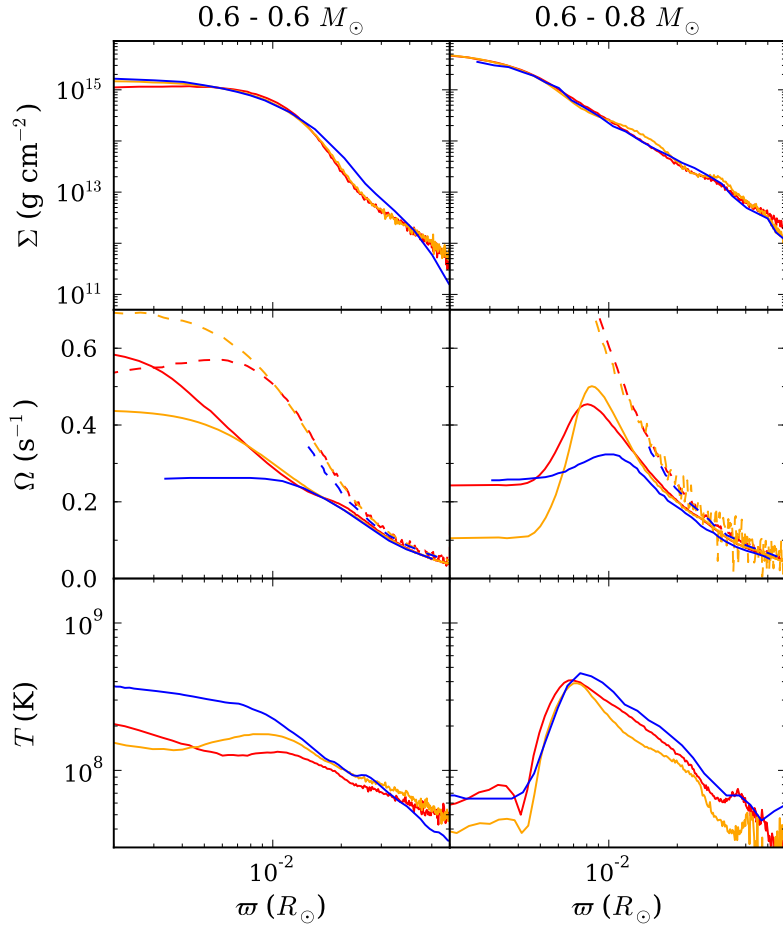


Figure 2.16: Comparison of our results with those of LIG09, for a $0.6 - 0.6 M_{\odot}$ (left) and a $0.6 - 0.8 M_{\odot}$ (right) merger. Shown are surface density, remnant (solid) and Keplerian (dashed) angular frequency, and temperature, with profiles from LIG09 in blue, and our equivalent ones in red and orange. Here, the former are for our default completion time of 6 initial orbital periods and the latter for their completion times (514 s or 10.9 orbital periods for the $0.6 - 0.6 M_{\odot}$ merger, and 164 s or 3.4 orbits for the $0.6 - 0.8 M_{\odot}$ merger).

Overall, the primary differences between our simulations appear to be the amount of spin-up and heating of the equal-mass merger. We believe it is unlikely that this reflects differences in initial conditions: we found much smaller changes in the angular velocity profile with increasing a_0 (see Fig. 2.11), and in the simulation of LIG09 the stars still seem to be quite close to spherically symmetric at the start and disrupt quickly (their Fig. 1), even though they were more properly relaxed. Instead, we believe the more likely explanation is that the viscosity prescription of LIG09, based on Riemann solvers, yields larger effective viscosity. This would explain both the reduction in angular velocity and increase in temperature (since viscous evolution converts rotational into thermal energy), as well as the fact that similar-mass mergers are affected more (they mix more, and LIG09 ran their equal-mass merger for a very long time). If we ran our simulations longer and thus included further viscous evolution, the similarity with their simulations would likely be closer.

2.5.2 Comparison with Others

Simulations of WD mergers have also been presented by Yoon et al. (2007), Pakmor et al. (2010; 2011b; 2012), Dan et al. (2011; 2012), and Raskin et al. (2012). Unfortunately, comparison with those results is difficult, since, unlike LIG09, all these authors are sparse with quantitative details about their results.

An exception is the $0.81 - 0.9 M_{\odot}$ merger simulated by Dan et al. (2012), shown in their Fig. 1. While that simulation is for synchronized WDs, it is still particularly useful to compare with, since Dan et al. show results for both approximate and accurate initial conditions. We find that their spherically enclosed mass profile is very similar to ours, with, e.g., $M = 0.9 M_{\odot}$ at 4.5×10^8 cm in both (though since spherically enclosed mass is a cumulative quantity, significant structural differences can remain hidden). Our spherically averaged density profile looks most similar to the profile they found using approximate initial conditions. Our central density, 1.9×10^7 g cm $^{-3}$, is within $\sim 10\%$ of theirs, and the density profile remains similar up to $r \simeq 5 \times 10^8$ cm ($\rho \simeq 10^6$ g cm $^{-3}$). Beyond, their profile becomes shallower while ours continues to decline; at $r = 10^9$ cm, they find $\rho \simeq 3 \times 10^5$ g cm $^{-3}$, while we find $\rho \simeq 10^5$ g cm $^{-3}$. This may be a consequence of the additional angular momentum associated with synchronized rotation. With accurate initial conditions, a difference with our results is that the density profile becomes flat beyond 10^9 cm.

Comparing temperature profiles, we roughly reproduce their spherically averaged one for approximate initial conditions, including the off-center peak – their T_{\max} is $\sim 20\%$ lower (to be expected since their binary is synchronized; see Sec. 2.4.3), but is also located at 4×10^8 cm (or $M_r \simeq 0.9 M_{\odot}$). However, our central temperature (2.2×10^8 K) is an order of magnitude higher than theirs (2×10^7 K) and at $r \gtrsim 10^9$ cm our temperatures are systematically hotter, perhaps a result of the much larger dissipation expected for non-rotating WDs. With accurate initial conditions they found an even narrower temperature peak than the one with approximate conditions, which thus deviates even more from our curve. This trend is similar to what we see when increasing a_0 (Sec. 2.4.2), so it seems likely we would reproduce their simulations more closely if we used the same initial conditions.

2.5.3 The Importance of Accurate Initial Conditions

Many of the recent simulations (Dan et al. 2011; 2012; Raskin et al. 2012) assume co-rotating WDs. This assumption is numerically convenient, in that it is relatively straightforward to start the simulation in the physically correct state: since in the co-rotating frame there are no flow velocities, one can easily relax a simulated binary within an appropriate potential in the co-rotating frame, damping out any velocities resulting from an initial mismatch.

As a result, it has been possible to study the onset of mass transfer in detail. As first pointed out by D’Souza et al. (2006) from simulations using a grid code, the disruption of the donor is preceded by a rather long – dozens of orbits – phase of mass transfer. Further simulations by Dan et al. (2011; 2012) showed that in this initial phase a significant fraction, $\sim 10\%$ of the donor mass, is transferred. As a result, e.g., the disk is substantially colder and more extended. The remnant core seems more subtly affected, in that its appearance becomes “more dissimilar”, reflecting that coalescence is between two WDs whose masses have become more disparate than they were initially. As a consequence, e.g., even for similar-mass binaries, the hottest point of the merger is found to be well outside the center. Indeed, Raskin et al. (2012) find that even for equal-mass binaries, the final outcome for more massive mergers is one where the core of one of the WDs is virtually undisturbed.

At present, it is not clear how important accurate initial conditions would be for asynchronous mergers. Qualitatively, we expect the effects to be smaller than for synchronous mergers, for three reasons. First, from the analytic study of Lai et al. (1994), in which tidal and rotational distortion are approximated by ellipsoids, co-rotating binaries always reach contact or Roche lobe overflow before becoming dynamically unstable, while irrotational binaries become dynamically unstable first. While an exact treatment of the irrotational case found that, in fact, Roche contact preceded dynamical instability (Uryū & Eriguchi 1998), it suggests that WDs in irrotational binaries will disrupt much sooner. Second, the simulations of LIG09 use initial conditions that should be quite close to correct, yet their WDs disrupt quickly (see Sec. 2.5.1). Third, the two components are counterrotating in the rotating frame. Hence, any mass transferred will hit the accretor with a larger relative velocity than would be the case for co-rotating WDs. Indeed, in the limit of equal-mass WDs, very little would happen for co-rotating WDs when one reaches contact, while a strong shock would be expected for the irrotational case. In general, one expects part of the shocked material to enter a high-entropy halo around the accretor. For co-rotating WDs, Dan et al. (2011) found that this halo helps remove angular momentum from the orbit, leading to a shorter start-up phase. For the irrotational case, given the stronger expected shocks, the start-up phase would likely be reduced even further. On the other hand, we saw in Sec. 2.4.2 that remnant properties are sensitive to changes in angular momentum content through changes in a_0 . Simulating more realistically the onset of mass transfer through accurate initial conditions will likely change a_0 .

Ideally, one would still simulate the initial mass transfer phase accurately. Unfortunately, even though the equilibrium solution is known (Uryū & Eriguchi 1998), it is not straightforward to set up the initial binary properly, since it is difficult to relax to a state that includes substantial fluid motion, and to slowly evolve such a state to contact, while ensuring viscosity remains low enough that there is no artificial tidal dissipation. Such dissipation is seen in our tests with varying initial distance a_0 in Sec. 2.4.2 (and may affect the simulations of LIG09 as well). Prior to coalescence, strong dissipation of tidal bulges heats the outer envelope of the donor (both stars for similar-mass mergers), and spin-orbit coupling due to both tides and the direct-impact accretion stream result in both donor and accretor becoming 25 - 50% synchronized by coalescence.

Since it significantly affects the merger and merger outcome, whether or not tidal dissipation causes real CO WD binaries to synchronize before the merger remains a major source of uncertainty. For the radiative stellar envelopes appropriate for WDs, tidal dissipation is expected to be inefficient, with a timescale 10^{12} to 10^{15} yrs, suggesting that WDs do not synchronize (Marsh et al. 2004, and references therein). However, coupling of the tides to pulsations may dramatically increase dissipation (Fuller & Lai 2012). Fortunately, it may be possible to determine the rate of synchronization observationally. For instance, Piro (2011) suggested that tidal dissipation is responsible for the relatively high temperature of the primary WD in the 13-minute eclipsing binary SDSS J065133.33+284423.3, predicting that it would be about halfway to being synchronized. This could be tested by either measuring the rotational broadening of the narrow cores of the hydrogen lines, or looking for velocity deviations through the transit of the more massive secondary.

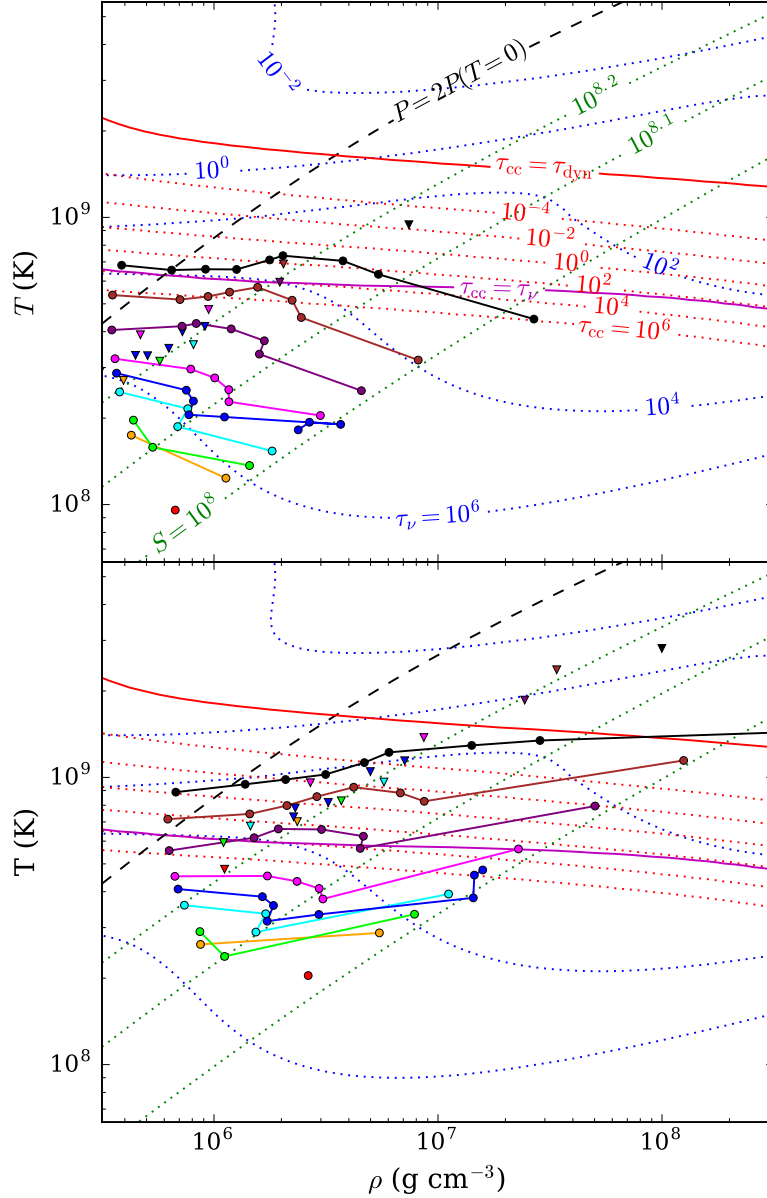


Figure 2.17: Left: merger remnant maximum temperature T_{\max} and corresponding density $\rho(T_{\max})$ for all merger remnants. Values along the equatorial plane are marked with circles, with lines connecting points with the same accretor mass, while values along the rotational axis (only plotted for similar-mass mergers) are marked with triangles (for all, colors indicate accretor mass, encoded as in Fig. 2.3). For similar-mass mergers, equatorial temperatures have been adjusted to account for mixing in convectively unstable cores. Right: maximum temperatures and corresponding densities following estimated post-merger evolution. The estimate assumes that the remnant spins down completely, that all rotational energy is used to drive matter to large distances, and that the remainder adjusts adiabatically (see text). Also shown are contours of constant neutrino cooling timescale $\tau_{\nu} \equiv C_P T / \epsilon_{\nu}$ and carbon fusion heating timescale $\tau_{cc} \equiv C_P T / \epsilon_{CC}$, both in years, as well as entropy S in erg K $^{-1}$. (Here, C_P is the heat capacity at constant pressure and ϵ the specific energy loss/gain rate.) The lines labeled $\tau_{cc} = \tau_{\nu}$ and $\tau_{cc} = \tau_{dyn}$ denote where the carbon fusion heating timescale balances the neutrino cooling and dynamical timescales, respectively. Finally, the $P = 2P(T=0)$ line is shown as an approximate upper bound of the region where degeneracy pressure dominates. All quantities were calculated using MESA (Paxton et al. 2011).

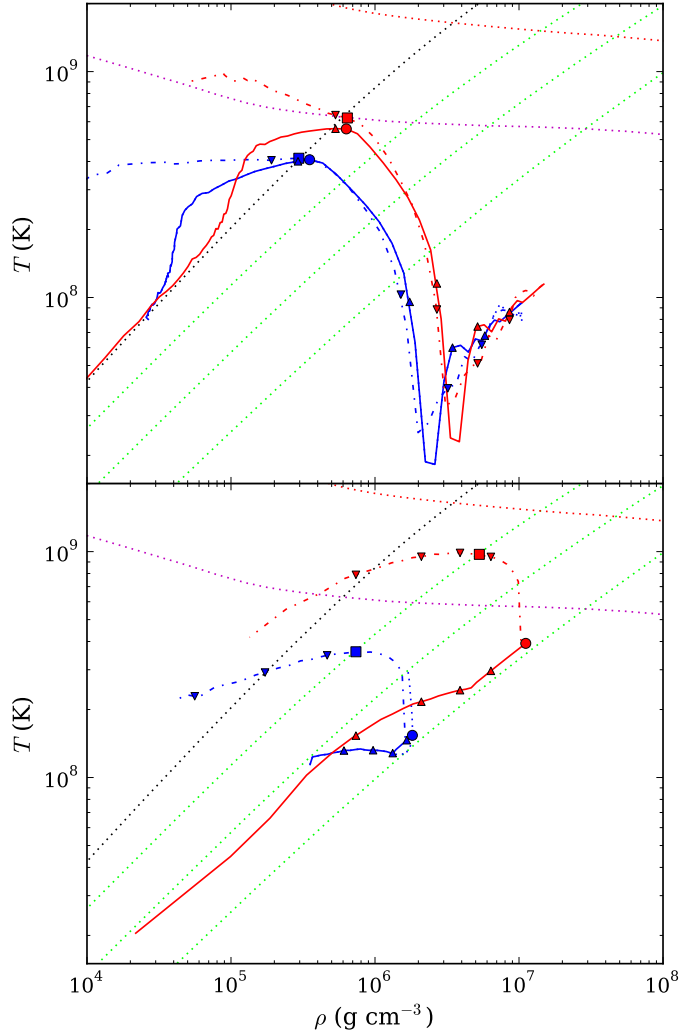


Figure 2.18: Estimate of post-merger viscous evolution for $0.4 - 0.8 M_{\odot}$ (top) and $0.6 - 0.6 M_{\odot}$ (bottom) mergers. In blue are shown the temperature-density structure of the merger remnant, on the equatorial plane before (dotted) and after (solid) correction for convection, as well as along the rotational axis (dot-dashed), with points marking the hottest locations (circles and squares) and steps of $0.2 M_{\odot}$ in spherical enclosed mass (triangles pointing up and down). In red, estimates of the structure following viscous evolution are shown, where it is assumed that the remnant spins down completely, that all rotational energy is used to drive matter to large distances, and that the remainder adjusts adiabatically (see text). For reference, also shown as dotted curves are the contours of constant entropy from Fig. 2.17 (green), as well as the lines where $\tau_{cc} = \tau^{\circ}$ (magenta), $\tau_{cc} = \tau_{dyn}$ (red), and $P = 2P(T=0)$ (black).

2.6 Post-Merger Evolution

We now turn to the question of how our merger remnants will evolve. To set the stage, we show in the left panel of Fig. 2.17 for all remnants the maximum temperature T_{\max} found along the equatorial plane¹⁰ as a function of the corresponding density $\rho(T_{\max})$. Here, for the similar-mass mergers for which we found convectively unstable cores (Sec. 2.3.2), we show the (lower) temperatures reached after artificially mixing them. For those mergers, the much higher temperatures reached along the rotational axis are shown as well (triangles). One sees the trends identified earlier: T_{\max} is mostly set by the accretor, while $\rho(T_{\max})$ depends more strongly on the donor. As a result, maximum temperature occurs in less degenerate conditions for dissimilar-mass mergers, crossing the degeneracy line for our most disparate cases. One also sees that for all but the most massive accretors, carbon fusion will not start: the neutrino cooling time is shorter than the fusion heating time. This is consistent with what was found in previous work (see Sec. 2.1).

2.6.1 Viscous Evolution and Possible Spin Down

Following the merger, processes that happen on timescales slower than the dynamical time can become important. These include viscous evolution, neutrino emission, radiative or convective thermal adjustment, and magnetic dipole radiation spin-down. Out of these, convection acts on the fastest timescale, and we already included its effect on the core in Fig. 2.17 left. Next fastest would almost certainly be viscous evolution. The merger remnant is unstable to both the magneto-rotational instability (Balbus & Hawley 1991) and Tayler-Spruit dynamo (Spruit 2002). Radiative adjustment is expected to be much slower, except at the surface, where radiative losses may also lead to convection in some systems (Shen et al. 2012; Schwab et al. 2012; Raskin et al. 2012). Using the standard Shakura & Sunyaev (1973) α -prescription for the viscosity $\nu = \alpha c_s H$, where c_s is the local soundspeed and H is the scale height of the system, the viscous evolution timescale for the remnant disk is

$$t_{\text{visc}} = \frac{R_{\text{disk}}^2}{\nu} = \frac{1}{\alpha} \left(\frac{R_{\text{disk}}}{H} \right)^2 t_{\text{dyn}} \sim \frac{10}{\alpha} t_{\text{dyn}}, \quad (2.24)$$

implying a timescale $t_{\text{visc}} \sim 10^3 - 10^5$ s for $\alpha \sim 10^{-3} - 10^{-1}$ and $t_{\text{dyn}} \sim 10$ s. This is orders of magnitude smaller than both the neutrino loss timescale ($\gtrsim 10^3$ yrs; see Fig. 2.17 left) and thermal adjustment timescale ($\gtrsim 10^4$ yrs; Shen et al. 2012).

It is possible that the strong differential rotation during a merger results in substantial amplification of magnetic fields. The one known probable WD merger remnant, RE J0317–853, has a surface magnetic field of 3.4×10^8 G (Barstow et al. 1995; Külebi et al. 2010). If mergers lead to strongly magnetized WDs, and these WDs additionally drive an ionized outflow, the magnetic coupling between the outflow and the WD could serve to transport angular momentum out of the system, spinning down the WD. The timescale for such a spin-down is roughly given by,

$$t_{\text{msd}} \sim \frac{L}{\dot{M} R_A^2 \Omega} \sim \frac{L}{(\dot{M} \Omega)^{3/5} (B^2 R^6)^{2/5}}, \quad (2.25)$$

¹⁰The central temperatures for the $0.625 - 0.65 M_{\odot}$ and $1.0 - 1.0 M_{\odot}$ mergers are $\sim 4\%$ and 10% lower than their respective maximum temperatures. In both cases, however, the center is much denser than the off-center hotspot, and since our estimated post-merger evolution more greatly affects central material, we show the central equatorial density and temperature for these two systems in Fig. 2.17 left, rather than the maximum.

where L is the angular momentum of the remnant, \dot{M} the mass loss rate, R_A the Alfvén radius, and Ω the angular spin frequency. For the second approximation, we used that $R_A \sim (B^2 R^6 / \dot{M} \Omega)^{1/5}$, with B the surface magnetic field and R the remnant radius. Scaling to $B = B_8 10^8$ G and $\dot{M} = \dot{M}_7 10^{-7} M_\odot \text{ yr}^{-1}$ (similar to what is observed for RE J0317–853 – see above – and [WR] cores of planetary nebulae [Hamann 1997]), and using the properties inferred for a $0.6 - 0.6 M_\odot$ remnant ($L \simeq L_{\text{tot}} \simeq 10^{50.5} \text{ g cm}^2 \text{ s}^{-1}$, $R \simeq R_{\text{disk}} \simeq 10^9 \text{ cm}$, $\Omega \simeq \Omega_{\text{max}} \simeq 10^{-0.3} \text{ s}^{-1}$, we find $t_{\text{msd}} \simeq 8 \times 10^3 B_8^{-4/5} \dot{M}_7^{-3/5} \text{ yr}$, which is of the same order as the neutrino cooling timescale of $\sim 10^4 \text{ yr}$ at the ignition line (for the whole range of remnants, $2 \times 10^3 \lesssim t_{\text{msd}} \lesssim 5 \times 10^4 \text{ yr}$).

Accretion from the disk, loss of rotational support, and possible cooling of the hot envelope could all compress and heat the remnant core. A detailed study of this is beyond the scope of this paper, but we can make first-order estimates of the effects on our merger remnants, and compare these with the more detailed analysis of Schwab et al. (2012) in one specific case.

For our estimates, we make four assumptions: (i) spin-down and accretion are much faster than thermal processes, and do not lead to local dissipation (i.e., particles entropies are constant in time); (ii) all angular momentum is carried away to large distances; and (iii) corresponding matter ends up with zero total energy (i.e., is at large distances and has negligible kinetic and internal energy). From energy conservation, the last assumption implies that the remaining object will have the same total energy as our merger remnant (but a lower mass), the first that it will have the same entropy structure, and the second that it has no rotational support. To determine the properties, we first determine the entropy profile of the merger remnant, by averaging entropy over isopotential surfaces. We then use this entropy profile and an estimated central density to construct a spherically symmetric (non-spinning) hydrostatic model, iterating on the central density until it has the correct total energy (inside of the zero-pressure surface). This automatically gives the mass contained in this object, which will be lower than our remnant mass, the remainder representing material that, due to dissipation of rotational energy, has expanded out to large distances and therefore provides negligible weight. To determine the evolution of hot spots, we order remnant particles by potential, and map them to their new positions in the final object, calculating new temperatures from the new densities, again assuming their entropy did not change (entropy is not constant over isopotential surfaces, so these temperatures are not strictly consistent with the hydrostatic model).

In Fig. 2.18, we show the results of our evolutionary estimate for our fiducial $0.4 - 0.8$ and $0.6 - 0.6 M_\odot$ systems. For the former case, the core-envelope, originally $0.90 M_\odot$, accretes $0.06 M_\odot$ from the disk, the remaining $0.25 M_\odot$ going to large distances. The central core is not significantly heated, while the lower-density hot envelope is, with the outer hot envelope along the rotational axis passing the ignition line. Since this material is almost non-degenerate, the resulting nuclear burning will likely be stable, or be extinguished by expansion. Thus, not unexpectedly, the hot envelopes of dissimilar-mass mergers are not good candidates for a nuclear runaway.

For the $0.6 - 0.6 M_\odot$ system, the center of the final, spun-down object is at much higher density and temperature than the remnant, while much of the outer regions have become less dense and cool. The latter happens because similar-mass mergers have strong rotational support, and if this is removed their binding energy increases significantly. To compensate for this, a large amount of mass has to expand to large distances, causing the core-envelope mass to decrease from $1.11 M_\odot$ to $0.91 M_\odot$. In the final object, the hottest point on the equatorial plane does not reach the ignition line, but the significantly hotter points above and below the equatorial plane do, at densities under which degeneracy pressure

still dominates. Hence, if the hot spots indeed compress with the rest of the remnant, a nuclear runaway could be triggered. (Of course, a nuclear runaway would start as soon as the heating timescale becomes shorter than the compression timescale, which may happen closer to the ignition line.)

In the right panel of Fig. 2.17, we show the results of applying our estimates to all our merger remnants. One sees that all compress and heat, and almost every remnant whose accretor mass is above $0.8 M_{\odot}$ will reach ignition somewhere on the equatorial plane, in many cases under degenerate conditions. We also chart the evolution of the off-center hot spots in similar-mass mergers (square points), and while they are at lower density, they remain degenerate and are all pushed substantially further above the ignition line than their counterparts on the equatorial plane. Almost all similar-mass mergers with an accretor mass above $0.5 M_{\odot}$ could therefore experience nuclear runaways due to their hot spots, though at least some of them will become non-degenerate before an explosion can occur.

The above suggests it is at least plausible that many of our mergers would eventually ignite in degenerate conditions, and that it thus is worthwhile to simulate their evolution in detail. Suitable simulations have recently been pioneered by [Shen et al. \(2012\)](#) and [Schwab et al. \(2012\)](#). [Shen et al.](#) started with a one-dimensional simulation, where they ported the remnant of a $0.6 - 0.9 M_{\odot}$ merger (from [Dan et al. 2011](#)), and evolved it assuming a $\gamma = 5/3$ polytropic equation of state and an $\alpha = 10^{-2}$ viscosity. They find the system spins down completely due to outward angular momentum transport, and the rotationally-supported thick disk is transformed into a tenuous, thermally-supported envelope that hardly affects the core. Over longer, thermal evolution timescales (simulated using MESA, [Paxton et al. 2011](#)), this tenuous hot envelope cools, compresses the core, and lights off-center convective carbon burning, eventually turning the remnant into an ONe WD (that may end its life in an accretion induced collapse).

[Schwab et al. \(2012\)](#) went a step further, porting the same $0.6 - 0.9 M_{\odot}$ simulation, as well as seven other systems, into two-dimensional ZEUS-MP2 simulations ([Hayes et al. 2006](#)), using the Helmholtz equation of state and an $\alpha = 3 \times 10^{-2}$ viscosity. They confirm the one-dimensional results, finding complete spin-down and transformation of the rotationally supported disk into a tenuous, spherically symmetric, hot envelope. They find a 50% increase in the temperature of the hottest point, and a factor of 3 increase in the corresponding density. They also find entropy to roughly be constant in the remnant, except in the outer regions and at the very center, where dissipation of rotational energy leads to heating.

It is encouraging that the results of the above detailed simulations are similar to what we find using our first-order estimates. For our $0.6 - 0.9 M_{\odot}$ remnant, our estimate give increases for the hottest equatorial point of a factor of 2.5 in density and 1.6 in temperature, reasonably close to what is found by [Schwab et al.¹¹](#). Thus, our simplifying assumptions appear to be appropriate at least for dissimilar-mass mergers, where most of the rotational dissipation will be in the disk and envelope, and the structure of the remainder is roughly spherically symmetric (both in density and temperature). It is not clear our estimates would be equally good for similar-mass mergers, where rotational dissipation should occur throughout the star, heating the entire remnant, and where there are substantial differences between the remnant's density and temperature structures. In particular, the rotational axis hotspots may dissipate, which would potentially make it more difficult for a similar-mass system to achieve a runaway. It will thus be particularly interesting to simulate the further evolution of those remnants in

¹¹For the hottest point along the rotational axis, we find a factor of 4.8 increase in density and 2.1 increase in temperature, suggesting our model does not depict as well the evolution of the outer hot envelope along the rotational axis.

more detail. Unfortunately, no such remnants were included by [Shen et al.](#) and [Schwab et al.](#).

2.6.2 Possible Explosions?

From our estimates, it seems that, as suggested by [vK10](#), many merger remnants will ignite carbon fusion. If a detonation is triggered, the resulting explosion may well resemble an SN Ia. Indeed, if the remnants spun down before ignition, their structures are sufficiently close to that of a cold WD that the calculations of [Sim et al. \(2010\)](#) should apply. From our estimates, for mergers that have a total mass between 1.2 and $1.4 M_{\odot}$ (which should be the most common ones), the final objects have masses between ~ 0.9 and $\sim 1.1 M_{\odot}$ which matches fairly nicely the range of ~ 1 to $\sim 1.2 M_{\odot}$ required to reproduce the observed range of SN Ia luminosities ([Sim et al. 2010](#)).

Of course, it is far from clear whether ignition leads to a detonation, since we do not currently understand how detonations are triggered ([Seitenzahl et al. 2009; Woosley et al. 2011](#), and references therein). Generally, it should help that ignition in our remnants is at much lower density (a few 10^7 g cm^{-3}) than is the case for near-Chandrasekhar models ($\sim 10^9 \text{ g cm}^{-3}$), because complete burning leads to much larger relative overpressures (e.g. [Mazurek et al. 1977; Seitenzahl et al. 2009](#)). Also, if a deflagration is started, plausible mechanisms to transition to a detonation all seem to require densities around 10^7 g cm^{-3} , where the conductive flame speeds are slower and the separation between the various burning fronts increases (e.g., [Woosley et al. 2009; 2011](#)).

An interesting aspect of our results is that for all cases ignition likely happens off-center: in shells for dissimilar-mass mergers and in hot spots along the rotational axis for similar-mass ones. Previous one-dimensional simulations suggested off-center ignition would lead to a slow deflagration flame that turns the CO WD into a ONe WD (e.g., [Saio & Nomoto 1985](#)). However, these calculations assumed a hot spot many pressure scale heights above the center. For ignition closer to the center, a deflagration plume is produced (e.g., [Aspden et al. 2011](#)), which may transition to a detonation ([Seitenzahl et al. 2011](#)) and unbind the star.

Given our findings, it seems likely that, if a detonation occurs, it will be triggered off-center. It would be interesting to simulate the resulting explosion, and see whether one could reproduce the observational evidence for asymmetries, which have been interpreted in terms of off-center ignition (though so far only in the context of near-Chandrasekhar models; [Maeda et al. 2010a;b](#)).

Finally, while we simulated only mergers of CO WDs, we can extrapolate our results to more massive ONe WDs. For these, the temperatures would be at least as high as for our $1 M_{\odot}$ accretors, and, after further viscous evolution, the mergers should become hot enough to ignite Ne burning. If this also leads to a detonation, the lower fusion energy released would likely lead to a less energetic explosion than expected for a CO WD merger, but it would produce far more ^{56}Ni and have a very large mass. Plausibly, it would resemble an SN Ia like SN 2009dc, which had unusually low ejecta velocities, produced $\sim 1.8 M_{\odot}$ of ^{56}Ni and had a total ejecta mass of $\sim 2.8 M_{\odot}$ ([Taubenberger et al. 2011](#)).

2.7 Conclusion

We have performed a large, detailed parameter-space study of CO WD mergers, extracting pertinent properties and profiles for each remnant, and studying how these vary across parameter space. For a

merger involving dissimilar-mass WDs, with low $q_\rho = \rho_{\text{c,d}}/\rho_{\text{c,a}}$, the outcome is a cold, slowly rotating, degeneracy-supported remnant core, which is essentially unaffected by the merger, surrounded by a hot, roughly spherical envelope and, further out, by a sub-Keplerian disk. For a similar-mass merger, with high q_ρ , an ellipsoidal core is produced along with a small disk, and the entire remnant is hot and partly supported by rotation. The transition between these two regimes is smooth, but occurs roughly at $q_\rho \simeq 0.6$, or equivalently a mass difference $\Delta M = M_{\text{a}} - M_{\text{d}} \simeq 0.1$. We found that for a fixed q_ρ , merger remnant curves are roughly homologous. We also presented trends for a number of merger remnant properties, providing linear scaling relations and best fits for most of them, hoping these can guide theoretical understanding and help analytical estimates.

We made first-order estimates of the post-merger viscous evolution and spindown, and found that it is plausible that a large fraction of the mergers simulated will eventually experience a nuclear runaway, as was suggested by vK10, and thus possibly end as thermonuclear supernovae. Further, detailed, simulations of this evolution across the whole parameter space, using techniques similar to those of Shen et al. (2012) and Schwab et al. (2012), would be required to confirm this. If the evolution of these remnants results in a detonation, a detailed comparison of the resulting light curve with observations must be carried out.

Our work represents one of the most detailed parameter studies of WD mergers to date. It would benefit, however, from resolution of a number of topics. First, for greater precision, it will be necessary to use better initial conditions. For synchronized systems, it is already known this has nontrivial effect on the outcome (Dan et al. 2011; 2012), and our results suggest it is important also for non-synchronized systems. Unfortunately, for the non-synchronized case, it is not trivial to implement the initial conditions, but better approximations are possible. Second, it would be useful to try to compare with merger simulations done with a grid code, which should have become more straightforward now that good moving mesh codes have become available (Springel 2010a; Duffell & MacFadyen 2011). More generally, whether or not WDs are synchronized before the merger remains unknown, yet clearly affects the resulting merger. Hopefully, this can be resolved empirically, by measuring the spin frequency for WDs in the very short-period binaries that have recently been discovered (e.g., Brown et al. 2011).

We thank Pablo Lorén-Aguilar, Enrique García-Berro, Stuart Sim, Enrico Ramirez-Ruiz, Marius Dan, James Guillochon, Evan Scannapieco, Cody Raskin and Ken Shen for insight into their simulations and useful discussion on the physics of mergers and post-merger evolution. We are grateful to Frank Timmes for creating the Helmholtz equation of state, and assisting us with its implementation in Gasoline, as well as to Bill Paxton and the MESA team for creating MESA and making it modular. This work made extensive use of NASA’s ADS and was supported by the Vanier and Discovery grants of Canada’s Natural Sciences and Engineering Research Council (NSERC).

2.8 Postscript: Post-Merger Evolution Revised

Since the publication of Z13, the work of Ji et al. (2013) was published, which is relevant not only because they simulate the post-merger evolution of an equal-mass $0.6 - 0.6 M_\odot$ remnant, but also because they eschew the use of an α -viscosity and instead directly evolve the magnetic field of the merger remnant. Also published was Raskin et al. (2014), which uses the machinery of Schwab et al. (2012) to generate post-viscous remnant profiles for massive (mostly dissimilar-mass) mergers with $> 0.9 M_\odot$ accretors, to determine their nucleosynthetic output if they then experienced a pure

detonation. They do not discuss their viscous simulations in detail. We have not performed our own post-merger evolution simulations¹², and use Schwab et al. (2012) and Ji et al. (2013)'s results extensively throughout this thesis - in particular, we reconsidered the simple estimate made in Sec. 2.6.1 using Ji et al. (2013)'s results when preparing ?. Since this thesis has no dedicated chapter on post-merger evolution, we expand and update the discussion in Sec. 2.6.1 below.

Ji et al. (2013) implements their magnetohydrodynamic simulation using the Eulerian grid code FLASH (Fryxell et al. 2000) and with the $0.6 - 0.6 M_{\odot}$ remnant of LIG09 for initial conditions. Like Schwab et al. (2012), they utilize a 2.5D axisymmetric grid, where a 2D grid extends along \hat{r} and \hat{z} (Schwab et al. (2012) use a $\hat{r} - \hat{\theta}$ spherical grid instead), while $\hat{\phi}$ quantities remain constant for all ϕ , and the Helmholtz EOS. Since LIG09's remnants are unmagnetized, they artificially insert a purely poloidal magnetic field whose strength is $\sim 10^8$ G in the remnant disk, and $\lesssim 10^5$ G in the core (they determine their results are robust to changing initial field strength and spatial resolution by factors of 2). They advance their simulation to 2×10^4 s, comparable to the completion times in Schwab et al. (2012). They find that the magnetorotational instability (MRI) acts on the differentially rotating portions of the remnant to greatly amplify the field over several hundred seconds, resulting in an equilibrium field with a peak strength of $\sim 10^9$ G in the disk and $\gtrsim 10^{10}$ G in the core, as well as a total magnetic energy of $\sim 10^{48}$ erg, on part with the differential rotation energy of the system (see Ch. 4). This field produces Maxwell stresses that are roughly equivalent to $\alpha \sim 10^{-2}$ viscosity, facilitating global outward angular momentum transport like in Schwab et al. (2012). It also generates a hot, magnetized corona by displacing disk material through magnetic buoyancy, and a binconal outflow along the remnant's rotational axis. These outflows eject $10^{-3} M_{\odot}$ of material at roughly twice the local escape speed (of ~ 1600 kms $^{-1}$).

Much like Schwab et al. (2012), the remnant loses most of its rotational support and evolves toward a spherically symmetric state with a dense, degeneracy-supported core and a more tenuous thermally-supported envelope. By the end of the simulation $\sim 0.08 M_{\odot}$ of material either resides in the magnetically dominated corona or is outfluxed from the simulation domain, leaving $1.12 M_{\odot}$ remaining in the remnant – though this does not distinguish between the core and envelope. Accretion onto and loss of rotational support within the core leads to its center being compressionally heated by a factor of ~ 2.5 in density and ~ 2 in temperature. As their initial conditions are a factor of ~ 2 hotter than our equivalent $0.6 - 0.6 M_{\odot}$ remnant (Sec. 2.5.1), this additional compression ignites central nuclear fusion.

How do Ji et al. (2013)'s results, alongside Schwab et al. (2012)'s, compare to our simple estimates of viscous evolution in Sec. 2.6.1? The most relevant quantities we need are the density and temperature at the center and at the hottest point of the post-viscous remnant, to determine whether carbon fusion ignites under highly degenerate conditions and the amount of material that remains a part of the dense, degeneracy-dominated remnant core. The latter is important for comparing against simmering WDs in Chapter ?. As noted in Sec. 2.6.1, we estimate the hottest point within our $0.6 - 0.9 M_{\odot}$ remnant increases by a factor of 2.5 in density and 1.6 in temperature, very similar to Schwab et al. (2012)'s results. The central density of their remnant is 1.75×10^7 g cm $^{-3}$ at the start of viscous evolution (Dan et al. 2011) and 2.8×10^7 g cm $^{-3}$ at the end – a factor of 1.6 increase, while we find a factor of 2.0. We tend to estimate much larger amounts of compressional heating for similar-mass systems, however, finding that the $0.6 - 0.6 M_{\odot}$ one increases its central density and temperature by a factor of 6.6 and

¹²We experimented with FLASH-based 2.5D simulations that included an α -viscosity, but did not follow up with a detailed investigation.

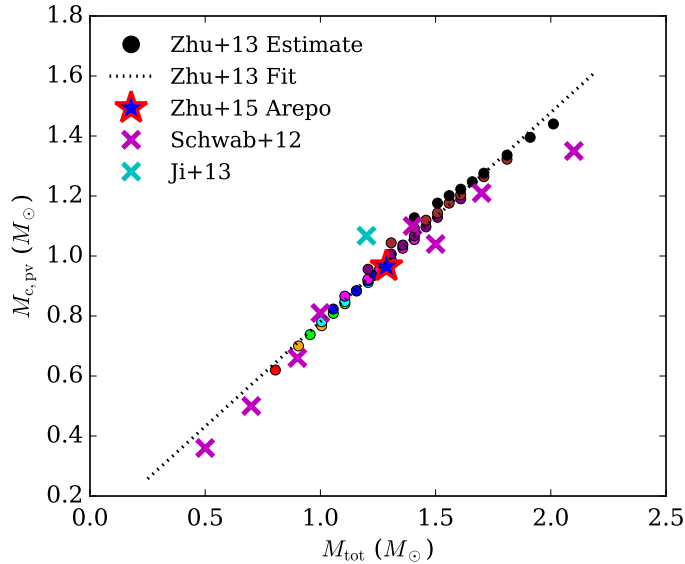


Figure 2.19: Post-viscous degenerate core mass $M_{c,pv}$, estimated using the simple viscous evolution prescription in Sec. 2.6.1, as a function of remnant total mass M_{tot} , for the simulated systems of Z13 (points; colors have the same meaning as in Fig. 2.17) and the $0.625 - 0.65 M_{\odot}$ remnant from the AREPO MHD simulation (Ch. 4; red-blue star). Also plotted are estimates of $M_{c,pv}$ from Schwab et al. (2012; using $M_c + M_{\text{tp}}$ in their Table 3) and Ji et al. (2013; estimated from integrating its spherical density profile to $r = 2 \times 10^9$ cm). The dotted line is a best fit to the Z13 points.

2.7, respectively, substantially larger than the ~ 2.5 and ~ 2 found by Ji et al. (2013). Similarly, Raskin et al. (2014) find the central density of their $1.0 - 1.0 M_{\odot}$ remnant increases from $7.1 \times 10^7 \text{ g cm}^{-3}$ to $2.4 \times 10^8 \text{ g cm}^{-3}$, a much smaller compression than the factor of ~ 10 we find. This is likely because our simple estimate assume all rotational energy is deposited as heat solely in the outermost regions of the remnant, while in reality remnants, particularly those of similar mass, are rotationally supported throughout and thus will likely also be heated throughout during viscous evolution, reducing the amount of core compression. We also note Ji et al. (2013)'s remnant also has not fully lost core rotational support at the end of their simulation, with Ω_c still $\approx 0.15 \text{ s}^{-1}$.¹³ We therefore can make reasonable estimates for dissimilar mass systems, but overestimate by a factor of a few the degree of compression and heating in similar-mass ones.

In our simple estimate, the mass of the post-viscous core, $M_{c,pv}$, is given by the mass of the spherically symmetric hydrostatic model representing the spun-down remnant (Sec. 2.6.1). In Fig. 2.19, we plot this mass versus the total mass of the merging binary, finding that to first order

$$M_{c,pv} = 0.70M_{\text{tot}} + 0.08 M_{\odot}, \quad (2.26)$$

($M_{c,pv}$ also has a weak inverse dependence on mass ratio q_m). We also perform our estimate on the $0.625 - 0.65 M_{\odot}$ remnant from our AREPO (Springel 2010a) MHD simulation in Ch. 4, and find little difference from its GASOLINE counterpart. For Schwab et al. (2012), $M_{c,pv}$ can be estimated from the combined mass of the core and isothermal region ($M_c + M_{\text{tp}}$ in their Table 3), which overall follow the

¹³We do not know if the same is true for Raskin et al. (2014)'s simulations. Ji et al. (2013) additionally note the central temperature at the end of evolution has not converged, increasing by $\sim 20\%$ with spatial resolution.

slope of Eqn. 2.26 but tend to be $\sim 0.1 M_{\odot}$ below it. For Ji et al. (2013), we estimate (from their Fig. 1) the spherical boundary between the dense core and tenuous envelope to be $r \approx 1.5 \times 10^9$ cm; $M_{c,pv}$ can then be estimated by determining the enclosed mass, which is $1.07 M_{\odot}$ (Suoqing Ji and Robert Fisher private communication), or $\sim 0.15 M_{\odot}$ above Eqn. 2.26's estimate. Our estimate therefore only roughly reproduces (with errors of $\sim 0.1 M_{\odot}$) the amount of mass remaining in the post-viscous core, partly because the assumption that material not in the core is marginally bound with $E = 0$ is overly simplistic, and partly because $M_{c,pv}$ is somewhat difficult to define in a system that may be supported by both degeneracy and thermal pressure.

For those systems that do not ignite nuclear fusion during the viscous phase, their next stage of evolution involves entropy being transported via radiative diffusion throughout and away from the remnant. Since the remnant hot envelope ($\rho \lesssim 10^4$ g cm $^{-3}$, $T \sim 10^9$ K) is radiation-dominated, it has a near-Eddington luminosity, and thermal evolution will occur over a timescale (Shen et al. 2012)

$$t_{\text{therm}} \sim E_{\text{th, envelope}} / L_{\text{edd}} \sim 10^4 \text{ yr.} \quad (2.27)$$

(For those systems that do ignite fusion, the nuclear runaway time is $\lesssim 10^2$ yr, so this evolution will only occur to a very limited extent.) Shen et al. (2012) simulates this phase of thermal evolution using the MESA (Paxton et al. 2011; 2013; 2015) 1D quasi-hydrostatic stellar evolution code, but use an artificial stellar profile that approximates their $0.6 - 0.9 M_{\odot}$ post-viscous remnant. Notably, they set the peak temperature at the base of the hot envelope (at $m \sim 0.9 M_{\odot}$) below the carbon ignition line. They find the entropy from the remnant interior diffuses outward over $\sim 10^4$ yr, leading to the further compression and heating of the interior until carbon fusion ignites at the (non-degenerate) base of the envelope. Meanwhile, convection rapidly redistributes entropy to much of the envelope, expanding it until its photosphere reaches $10^{12} - 10^{13}$ cm, comparable to giant stars. They predict that their remnant will be converted into an ONe WD, much like in earlier calculations of near-Eddington accretion onto massive WDs (eg. Saio & Nomoto 1985).

More recently, Schwab et al. (2016) have directly ported their post-viscous $0.6 - 0.9 M_{\odot}$ remnant from Schwab et al. (2012), and a more massive $0.64 - 0.96 M_{\odot}$ one from Raskin et al. (2014), into MESA to simulate their thermal evolution. The peak temperatures of both remnants are already high enough to ignite carbon nuclear fusion at the very start of the simulation; this generates a carbon-burning shell that propagates inward via conduction, reaching the center of the WD in $\sim 2 \times 10^4$ yr. The result is a non-degenerate, but still bound, ONe WD, which will subsequently cool through neutrino losses and contract. For those remnants with masses $\gtrsim 1.35 M_{\odot}$, this contraction leads to off-center neon burning to silicon-group elements, and for super- M_{Ch} remnants, may even lead to fusion to iron followed by core-collapse into a neutron star. For substantially sub- M_{Ch} remnants that nevertheless ignite non-explosive burning, though, the likely end result is a massive ONe WD.

Thermal evolution of post-viscous remnants that are hottest at their *center* have, to our knowledge, not yet been calculated. We expect it would be qualitatively similar to the findings of Shen et al. (2012) and Schwab et al. (2016) their dissimilar-mass remnants: a further compression of the interior over $\sim 10^4$ yr, and less heating than if the compression were adiabatic, since radiative and neutrino cooling become significant over these longer timescales. We thus expect that systems brought to the brink of ignition by viscous spin-down may subsequently ignite due to thermal contraction, though the number of such systems is likely to be small. Those whose central temperatures are significantly below 6×10^8 K will cool too much during their compression to ignite, and, since neutrino cooling is density-dependent,

may experience off-center ignition instead.

The radiation-dominated envelope alongside the remnant’s carbon-oxygen composition, however, suggest that the remnant drives strong winds, complicating the thermal evolution and potentially preventing an AIC (Shen et al. 2012; Schwab et al. 2016). They may also impress the remnant with distinct observational properties, which we discuss in Sec. [XXX](#).

Chapter 3

White Dwarf Mergers in Smoothed-Particle and Moving Mesh Hydrodynamics

Chenchong Zhu, Rüdiger Pakmor, Marten H. van Kerkwijk, Philip Chang

The physics and final outcomes of the merger of two white dwarfs can currently only be directly studied in detail through 3D hydrodynamic simulations, and to date merger simulations have largely relied on smoothed-particle hydrodynamics, a method known to produce numerical artefacts under certain conditions. In order to determine if the outcome of these simulations depend on the code being used, we followed the merger of a $0.625 - 0.65 M_{\odot}$ carbon-oxygen white dwarf binary in both the SPH code GASOLINE and the moving mesh code AREPO. We find that the two agree well with one another until the merger is complete. Afterward, the merger remnant becomes axisymmetric over the course of a few hundred seconds in GASOLINE, with most of its mass comprising a dense, oblate-spheroidal core. The remnant in AREPO, on the other hand, remains non-axisymmetric and features a crescent-shaped core flanked on one side by a hot, underdense “void”. This configuration has an offset gravitational potential, which launches an $m = 1$ spiral mode within the surrounding disk that transports disk angular momentum over a timescale of $\sim 10^3 - 10^4$ s comparable to that of the standard α -viscosity formulation. These code-dependent differences could substantially affect processes that occur early-on during post-merger viscous evolution, from magnetic dynamo processes to the possible onset of a nuclear detonation. The final product, of the merging process, however, likely remains a spherically symmetric dense core surrounded by a hot, non-degenerate envelope, regardless of which code is used.

This chapter is heavily updated from an unpublished paper from late 2014. I include a summary of our preliminary investigation in 2013-2014, which led to the discovery that AREPO failed to conserve angular momentum over timescales relevant to the merger. The latter resulted in modifications to AREPO (Pakmor et al. 2016), which I also summarize.

3.1 Introduction

Simulations of white dwarf (WD) mergers are a window into the detailed dynamics of the merging process and – since mergers cannot directly be seen using current observational capabilities – a link between observations of strange stars and explosive transients and theories about their formation. Since the pioneering work of Benz et al. (1990), these simulations have overwhelmingly used a single numerical hydrodynamics implementation, smoothed-particle hydrodynamics (SPH), to model WD mergers. Within SPH, regions of high density are automatically more resolved and advection is simulated without errors; its equations of motion also inherently conserve energy, linear and angular momentum. These features make it attractive for modelling the bulk fluid flows and complicated geometry present in mergers. Building on Benz et al. and other early works such as Segretain et al. (1997) and Guerrero et al. (2004), more recent efforts has focused on more precise binary initial conditions (Dan et al. 2011), exploration of remnant properties across parameter space (Lorén-Aguilar et al. 2009; Raskin et al. 2012; Zhu et al. 2013; Dan et al. 2014) and exploring the possible instigation and consequences of a thermodynamic transient caused by the merger (eg. Pakmor et al. 2010; Dan et al. 2012; Pakmor et al. 2013; Moll et al. 2014; Raskin et al. 2014).

The traditional SPH formulation is not without its problems, however (eg. Springel 2010a; Hopkins 2015): it uses an artificial viscosity, which can produce spurious heating and angular momentum transport in shear flows, it is known to suppress hydrodynamic instabilities, and has relatively poor shock and steep gradient capture compared to other schemes at the same resolution. Shocks, large-scale shear flows and the formation of instabilities are all expected for WD mergers, and comparisons between SPH and Eulerian grid codes for other astrophysical phenomena (eg. de Val-Borro et al. 2006; Trac et al. 2007; Mitchell et al. 2009) have often shown qualitative and resolution-independent differences. Reproducing simulations across different types of codes is essential both for development of numerical hydrodynamic schemes and for ensuring the physical validity of their results, and so we are motivated to simulate mergers with other hydrodynamic schemes.

A recent alternative to SPH, as well as Eulerian grid codes, is AREPO (Springel 2010a), one of a growing class of codes (eg. Duffell & MacFadyen 2011; Gaburov et al. 2012; Vandenbroucke & De Rijcke 2016) that render fluid evolution on a dynamically moving unstructured mesh. AREPO retains the accurate treatment of shocks and instabilities as well as negligible artificial viscosity that Eulerian grid codes feature, while gaining the automatic refinement and Galilean invariance inherent to SPH. These features, coupled with a tree-based self-gravity solver, make it highly attractive for astrophysical simulations (eg. Vogelsberger et al. 2012; Pakmor & Springel 2013; Hayward et al. 2014; Marinacci et al. 2014; Ohlmann et al. 2016), and, with the notable exception of formal angular momentum conservation, ideal for simulating WD mergers. AREPO has already been used to investigate helium detonations during the initial mass transfer phase of a $0.9 - 1.1 M_{\odot}$ CO WD merger (Pakmor et al. 2013).

In this work, we compare the merger of a $0.625 - 0.65 M_{\odot}$ carbon-oxygen (CO) WD binary simulated in AREPO with one simulated in the SPH code GASOLINE (Wadsley et al. 2004). We generate identical initial conditions for both simulations, and disable chemical and nuclear evolution to focus solely on the hydrodynamic differences. The purpose of this work is not to compare SPH to AREPO in the abstract, but rather to understand if any critical hydrodynamic phenomena is missing or misrepresented from past SPH-based merger simulations. Our results show that the two simulations closely resemble one another until the two WDs coalesce, after which the GASOLINE merger remnant becomes axisymmetric

over several hundred seconds, while the AREPO one remains asymmetric for much longer, potentially altering post-merger evolution. This work is also a companion to Zhu et al. (2015; henceforth Z15), which presents the growth of a seed magnetic field within the AREPO-based merger to amplitudes of $\sim 10^{10} - 10^{11}$ G, which also has significant consequences for post-merger evolution.

In Section 3.2, we review the hydrodynamic schemes of SPH and AREPO, and discuss the parameters and initial conditions used in each simulation. In Section 3.3, we summarize efforts to improve angular momentum conservation within AREPO, essential to both this work and Z15. In Section 3.4, we present results for each code and compare their outcomes. Lastly, in Section 3.5, we describe which code represents the more physical result, and implications for merger outcomes.

3.2 Codes and Initial Conditions

All hydrodynamic and magnetohydrodynamic codes seek to properly evolve the continuum dynamics of a fluid on a discrete set of points in space and time. Most astrophysical fluid codes (including the two we use) explore the simpler regimes of ideal hydro- or magnetohydrodynamics, where molecular viscosity and electrical resistance are negligible – generally the case astrophysical settings outside of planetary interior dynamics. The coupled partial differential equations of ideal magnetohydrodynamics, in their conservative form and with Gaussian units (eg. Goedbloed & Poedts 2004; Pakmor & Springel 2013; Spruit 2013, Feiden & Chaboyer 2012 Sec. 3), is

$$\begin{aligned}\partial_t \rho + \partial_j(\rho u^j) &= 0 \\ \partial_t(\rho u^i) + \partial_j(\rho u^i u^j + \delta^{ij} P_{\text{tot}} - \frac{1}{4\pi} B^i B^j) &= \rho \partial^i \Phi \\ \partial_t(\rho e) + \partial^j \left(u_j (\rho e + P_{\text{tot}}) - \frac{B_j}{4\pi} (u^l B_l) \right) &= u_j \rho \partial^j \Phi \\ \partial_t B^i - \partial_j(u^i B^j - u^j B^i) &= 0,\end{aligned}\quad (3.1)$$

where ρ , u^i , B^i , and Φ are the density, velocity, magnetic field and gravitational potential, respectively, $P_{\text{tot}} = P + \frac{1}{8\pi} B_j B^j$ is the total pressure, $e = \frac{1}{2} u_i u^i + e_{\text{int}} + \frac{B^2}{8\pi\rho}$ is the specific total energy, and the usual Einstein summation convention holds. This can be written in compact form:

$$\frac{\partial \mathbf{U}}{\partial t} + \nabla \cdot \mathbf{F}(\mathbf{U}) = \mathbf{G} \quad (3.2)$$

where

$$\mathbf{U} = \begin{pmatrix} \rho \\ \rho \mathbf{u} \\ \rho e \\ \mathbf{B} \end{pmatrix}, \quad (3.3)$$

$$\mathbf{F}(\mathbf{U}) = \begin{pmatrix} \rho \mathbf{u} \\ \rho \mathbf{u} \mathbf{u}^T + P_{\text{tot}} - \frac{1}{4\pi} \mathbf{B} \mathbf{B}^T \\ \mathbf{u} (e + P_{\text{tot}}) - \frac{\mathbf{B}}{4\pi} (\mathbf{u} \cdot \mathbf{B}) \\ \mathbf{B} \mathbf{u}^T - \mathbf{u} \mathbf{B}^T \end{pmatrix}, \quad (3.4)$$

$$\mathbf{G} = \begin{pmatrix} 0 \\ \rho\mathbf{g} \\ \rho\mathbf{u} \cdot \mathbf{g} \\ 0 \end{pmatrix}. \quad (3.5)$$

Eqn. 3.2 shows that the time-derivative of the fluid's values is given by the sum of a flux term (since, by the Green-Gauss theorem, the integral of $\nabla \cdot \mathbf{F}(\mathbf{U})$ within a volume is equivalent to a flux across its boundary) and a (self-)gravitational source term \mathbf{G} . These are generally calculated separately, and then combined.

To better understand the code comparison in this chapter, and to preface the discussion of improving AREPO's angular momentum conservation in Sec. 3.3, we present an extremely short and mostly qualitative discussion of how these equations are implemented within SPH and AREPO. The historical development of both methods is long and involved, and, as improving hydrodynamic simulations is not the focus of this thesis, we will refer the reader to a number review articles referenced throughout this section for further details.

3.2.1 Traditional Smoothed-Particle Hydrodynamics

SPH, first introduced in [Lucy \(1977\)](#) and [Gingold & Monaghan \(1977\)](#), is a mature simulation method used in a host of astrophysical contexts ranging from star formation to cosmology. Our overview summarizes the first few sections of [\(Springel 2010b\)](#); we also refer readers to [\(Monaghan 2005\)](#) and [Rosswog \(2009\)](#) for further details.

SPH represents a fluid with a set of particles. The fluid's continuum properties at some point \mathbf{r} in the simulation are sampled by using these particles as interpolation points. Representing any given continuum property (the most important of which is density, since it factors into the equations of motion) as $F(\mathbf{r})$, we can use a "kernel" $W(\mathbf{r}, h)$ to generate its approximate, locally-averaged value

$$F_s(\mathbf{r}) = \int F(\mathbf{r}') W(\mathbf{r} - \mathbf{r}', h) d\mathbf{r}'. \quad (3.6)$$

In the (computationally impossible) case of infinite resolution, we can choose $W(\mathbf{r}, h)$ to be a Dirac delta, and $F_s(\mathbf{r}) = F(\mathbf{r})$, but in practice we choose $W(\mathbf{r}, h)$ to extend over some characteristic "smoothing length" h . If $W(\mathbf{r}, h)$ were a Gaussian, the $h = \sigma$, the standard deviation. The most popular form of $W(\mathbf{r}, h)$ is a cubic spline that goes to zero when $\mathbf{r} > 2h$, and h is generally set to ensure a user-defined number of neighboring particles N fall within the kernel. For a set of particles with associated mass m_i and known values of $F_i = F(\mathbf{r}_i)$, we can discretize the integral as

$$F_s(\mathbf{r}) = \sum_j \frac{m_j}{\rho_j} F_j W(\mathbf{r} - \mathbf{r}_j, h). \quad (3.7)$$

where ρ_i can be estimated using $\rho_i = \sum_j m_j W(\mathbf{r}_i - \mathbf{r}_j, h)$. Derivatives of the field can also be determined using the gradient of the kernel $\nabla_i W_{ij}$.

Meanwhile, the Euler equations (Eqn. 3.2 without the gravitational and magnetic terms) can be shown to follow the Lagrangian:

$$L = \int \rho \left(\frac{\mathbf{u}^2}{2} - e \right) dV \quad (3.8)$$

which can be discretized for a set of particles as

$$L_{\text{SPH}} = \sum_i \frac{1}{2} m_i u_i^2 - m_i e_i. \quad (3.9)$$

This suggests a time-evolution scheme for the fluid. Each particle representing the fluid is given a (time-independent) mass m_i , position \mathbf{r}_i , velocity \mathbf{u}_i and specific internal energy e_i ; the fluid can then be simulated by time-evolving the latter three terms for all particles. The equations governing the latter two are derived by applying the Euler-Lagrange equation ($\frac{d}{dt} \frac{\partial L}{\partial \dot{\mathbf{r}}_i} - \frac{\partial L}{\partial \mathbf{r}_i}$) to L_{SPH} . They traditionally takes the form:¹

$$\frac{d\mathbf{u}_i}{dt} = - \sum_j m_j \left(\frac{P_i}{\rho_i^2} + \frac{P_j}{\rho_j^2} \right) \nabla_i W_{ij} \quad (3.10)$$

$$\frac{de_i}{dt} = - \frac{P_i}{\rho_i^2} \sum_j m_j (\mathbf{u}_i - \mathbf{u}_j) \cdot \nabla_i W_{ij} \quad (3.11)$$

where pressure P_i is determined from ρ_i and e_i using a user-prescribed equation of state. The left panel of Fig. 3.1 summarizes this scheme. Note that since Eqn. 3.8 has no time-dependence and is translationally and rotationally invariant, SPH naturally conserves total energy, momentum and angular momentum. Self-gravity can be added as an additional force to Eqn. 3.10 (see Springel 2010b Sec. 2.4 and Wadsley et al. 2004 Sec. 2.1) using methods originally developed for N -body simulations. Magnetic fields can also be included (eg. Price 2012), but the resulting “SPHMHD” formulation is not used in this thesis.

As given, the SPH equations of motion conserve entropy, but entropy must increase in the presence of shocks. The most popular solution is to include an artificial viscosity term

$$- \sum_j m_j \pi_{ij} \nabla_i W_{ij} \quad (3.12)$$

to Eqn. 3.10, where, defining $\mathbf{r}_{ij} = \mathbf{r}_i - \mathbf{r}_j$ and $\mathbf{u}_{ij} = \mathbf{u}_i - \mathbf{u}_j$,

$$\pi_{ij} = \begin{cases} \frac{-\alpha \frac{1}{2}(c_i + c_j)\mu_{ij} + \beta \mu_{ij}^2}{\frac{1}{2}(\rho_i + \rho_j)} & \text{for } \mathbf{u}_{ij} \cdot \mathbf{r}_{ij} < 0 \\ 0 & \text{otherwise,} \end{cases} \quad (3.13)$$

where $\mu_{ij} = \bar{h} \mathbf{u}_{ij} \cdot \mathbf{r}_{ij} / (|\mathbf{r}_{ij}|^2 + 0.04\bar{h}^2)$, $\bar{h} = \frac{1}{2}(h_i + h_j)$, c_i is the sound speed and α and β are tunable parameters ($\beta = 2\alpha$ is used in GASOLINE). In addition to facilitating shock capture, π_{ij} also prevents spurious particle interpenetration between interacting flows (Hernquist & Katz 1989). It, however, can also introduce spurious viscous forces, and so must be damped in the absence of shocks. In shear flows, this can be done with a “Balsara switch”, which multiplies π_{ij} with a prefactor, proportional to the ratio between the divergence and curl of velocity, that goes to zero in the presence of a pure shear flow. It is also possible to make the α and β coefficients in π_{ij} time-variable (eg. Morris & Monaghan

¹We state Wadsley et al. (2004)’s formulation of Eqns. 3.10 and 3.11, as Springel (2010b) assumes a different method of controlling the smoothing length h_i .

1997; Dolag et al. 2005) with

$$\frac{d\alpha_i}{dt} = -\frac{\alpha_i - \alpha_{\min}}{\tau} + S_i \quad (3.14)$$

where $\tau = h_i/(c_i l)$, l is a tuneable parameter of order unity, S_i is a source term that becomes large in the presence of shocks, and $\alpha_{\min} > 0$ is a minimum α value to negate noise and spurious particle interpenetration in smooth flows. Eqn. 3.14 exponentially damps α to its minimum value over timescale τ in the absence of shocks, and increases it via the source term when shocks are present. Both these methods are used in GASOLINE.

As explained in the introduction, SPH’s Lagrangian nature allows it to automatically resolve regions of high density, simulate advection without errors, and conserve energy, linear and angular momentum to high accuracy. These features make it much easier to model mergers in SPH than in Eulerian grid schemes, which discretize the simulation volume on a static grid, and time-evolve the system by tracking fluid fluxes between grid cells. These traditionally have issues with simulating advection, and adaptively increasing the spatial resolution when following orbiting binaries, except under specific coordinate systems and symmetries (eg. (Hopkins 2015)), and thus have very infrequently been used to simulate WD mergers (see Katz et al. (2016), however for recent developments).

The limitations of SPH (and Eulerian codes) have also been well-covered in literature (see, eg., the introductions to Springel 2010a; Hopkins 2015; Katz et al. 2016). Chief among them is the artificial viscosity discussed above, which can produce spurious heating and angular momentum transport in shear flows even in codes that utilize the Balsara switch and time-variable viscosity (Cullen & Dehnen 2010). Classical formulations of SPH have also been known to suppress hydrodynamic instabilities (eg. Agertz et al. 2007) due to poor treatment of contact discontinuities manifesting as a “surface tension” (eg. Read et al. 2010; Heß & Springel 2010). While this has subsequently been resolved (eg. Hopkins 2013; Hu et al. 2014; Keller et al. 2014) by introducing artificial mixing terms (Price 2008) and smoothing the pressure as well as the density across discontinuities (eg. by replacing the $P_i/\rho_i^2 + P_j/\rho_j^2$ term in Eqn. 3.10 with $(P_i + P_j)/(\rho_i\rho_j)$; Keller et al. 2014) the vast majority of merger simulations in the literature come from before these alterations became widely used. SPH resolves shocks and steep gradients relatively poorly compared to Eulerian schemes due to kernel smoothing of the density, and can corrupt smooth flows with particle velocity noise (Springel 2010b). Lastly, it suffers from a resolution-independent “ E_0 ” error associated with Eqn. 3.10 (eg. Read et al. 2010), which in some situations produces enough noise to drown out large-scale structures (Hopkins 2015). All of these issues motivate both the further development of SPH and competing hydrodynamic schemes, and simulating mergers in a diversity of codes.

3.2.2 GASOLINE SPH Code

GASOLINE is a modular, tree-based SPH code that we previously used to explore the parameter space of CO WD mergers in Zhu et al. (2013; henceforth Z13). Code settings and initial conditions used in this work are nearly identical to those used in Z13, and we refer the reader to that paper for further details. We utilize GASOLINE’s default Hernquist & Katz (1989) kernel with 100 neighbours, and use the asymmetric energy formulation (Wadsley et al., Eqn. 8) to time-evolve particle internal energy. Artificial viscosity is dynamically controlled using a combination of the Balsara switch and time-variable coefficients for the α and β viscosity terms ($\alpha = 0.05$, $\beta = 0.1$ when shocks are not present,

and approximately unity when they are). We utilize the Helmholtz equation of state² (EOS; Timmes & Swesty 2000) to properly represent arbitrarily degenerate and relativistic gases. Since GASOLINE tracks the particle internal energy, while Helmholtz uses temperature as an input, a Newton-Raphson inverter is included in the EOS to determine the latter from the former. To keep the energy-temperature relation positive-definite for the inverter, we enable Coulomb corrections even when the total entropy becomes negative. SPH noise occasionally brings highly degenerate particles to below the Fermi energy. Under these conditions we set the pressure to the Fermi pressure, but let the energy freely evolve (see Zhu et al. 2013, Sec. 4.6).

Like in our previous work, we ignore outer hydrogen and helium layers, composition gradients, and any nuclear reactions, in order to focus on the merger hydrodynamics. Previous work that did include nuclear reactions (Lorén-Aguilar et al. 2009; Dan et al. 2012), and in one case an outer helium layer (Raskin et al. 2012), have shown that they play a negligible role in the hydrodynamics of a $0.625 - 0.65 M_{\odot}$ CO WD merger. More massive binaries, as well as less massive ones involving a CO-He hybrid WD, may experience He or CO detonations during the merger (Pakmor et al. 2010; Raskin et al. 2012; Dan et al. 2012).

We use the same version of GASOLINE as Z13, which does not include the improvements recently introduced in GASOLINE2 (Keller et al. 2015; Tamburello et al. 2015) and CHANGA/GASOLINE (Governato et al. 2015). These include a turbulent diffusion scheme to facilitate fluid mixing (Shen et al. 2010) and the use of the $(P_i + P_j)/(\rho_i \rho_j)$ density-averaged pressure term in the SPH force expression (Keller et al. 2014) to properly treat contact discontinuities. We also do not consider more advanced prescriptions for viscosity, such as Godunov-SPH (eg. Cha & Wood 2016), as these are generally not implemented in SPH codes. We again stress that the purpose of this work is to compare the traditional SPH formulation, used in almost all merger simulations to date, to AREPO, and we leave comparisons with improved and modified SPH schemes to future work.

3.2.3 AREPO Moving Mesh Code

We now introduce AREPO’s moving-mesh magnetohydrodynamics scheme, summarizing Springel (2010a), Pakmor et al. (2011a) and Pakmor & Springel (2013). AREPO discretizes a fluid using a mesh (i.e. a grid), much like static Eulerian codes. To overcome the traditional Eulerian code shortcomings of not being Galilean invariant, having large advection errors and having difficulty adjusting spatial resolution for complex flows, AREPO moves the mesh to follow local fluid motion. Fluxes between mesh cells are calculated in the frame of the (moving) cell walls that divide them – this preferred frame choice, in addition to the moving mesh, give the scheme a Lagrangian nature and automatic spatial refinement similar to SPH. Allowing a structured grid to move with the fluid can lead to severe mesh deformation that prevent its further evolution. AREPO circumvents this by utilizing an unstructured mesh defined by Voronoi tessellation (see Springel 2010a, Sec. 2) of a set of “mesh-generating points”, each of which corresponds to a single mesh cell. The mesh-generating points are given the velocities of the fluid they represent, and the tessellation reperformed at each timestep. The result is a moving mesh that, due to the mathematical properties of Voronoi tessellation, does not suffer from mesh-tangling effects. To keep the Voronoi mesh regular (improving computational efficiency), mesh-generating point velocities are slightly altered from their pure Lagrangian values, and additional velocity adjustments

² Available at <http://cococubed.asu.edu/>.

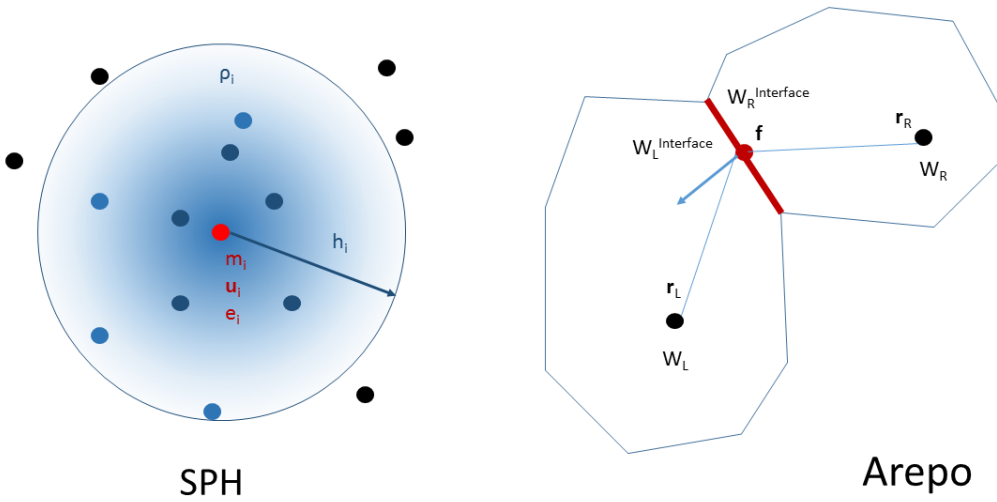


Figure 3.1: PLACEHOLDER!!!

can be made to keep cells near a constant mass or volume. This representation of the fluid also couples more naturally to N -body based gravity solvers (see Springel 2010a, Sec. 3), with AREPO using a nearly identical TreePM solver as the SPH code GADGET2 (Springel 2005).

On the Voronoi mesh, AREPO tracks the finite volume integral of \mathbf{U} (Eqn. 3.3) for each cell, i.e.

$$\mathbf{Q} = \int_V \mathbf{U} dV = \begin{pmatrix} m \\ \mathbf{p} \\ E \\ \mathbf{B}V \end{pmatrix}, \quad (3.15)$$

where m is the cell mass, \mathbf{p} its momentum, E its total energy and \mathbf{BV} the magnetic field multiplied by the cell volume. The time-evolution for cell i from timestep n to $n + 1$ is then given by

$$\mathbf{Q}_i^{n+1} = \mathbf{Q}_i^n - \Delta t \sum_j A_{ij} \hat{\mathbf{F}}_{ij}^{n+1/2} \quad (3.16)$$

where Δt is the timestep, j stands for all cells that border cell i , A_{ij} is the oriented area of the face dividing cells i and j and $\hat{\mathbf{F}}_{ij}$ is the estimated flux between them (positive flux means escaping from i). In practice fluxes are more easily calculated using primitive variables

$$\mathbf{W} = \begin{pmatrix} \rho \\ \mathbf{v} \\ P \\ \mathbf{B} \end{pmatrix} \quad (3.17)$$

and then converted back to \mathbf{Q} . As noted earlier, fluxes are calculated in the frame of face A_{ij} to maintain

Galilean invariance, so the \mathbf{W} on either side of the face – which we term the “left” and “right” cells – is boosted by A_{ij} ’s velocity before being used. The geometry of this setup can be seen in Fig. 3.1. In AREPO’s original formulation (Springel 2010a), the values of $\mathbf{W}^{\text{interface}}$ on the left and right sides of A_{ij} ’s centroid are determined from their respective cell’s \mathbf{W} using the MUSCL-Hancock approach of a piecewise linear spatial reconstruction and a first-order time-extrapolation by half a timestep:

$$\mathbf{W}_{\text{L,R}}^{\text{interface}} = \mathbf{W}_{\text{L,R}} + \frac{\partial \mathbf{W}}{\partial \mathbf{r}} \Big|_{\text{L,R}} (\mathbf{f} - \mathbf{s}_{\text{L,R}}) + \frac{\partial \mathbf{W}}{\partial t} \Big|_{\text{L,R}} \frac{\Delta t}{2}, \quad (3.18)$$

where \mathbf{f} is the position of A_{ij} ’s centroid, and \mathbf{s} each cell’s center-of-mass. The spatial gradient is estimated by taking advantage of the Green-Gauss theorem:

$$\langle \nabla \phi \rangle_i = \frac{1}{V_i} \sum_j \phi(\mathbf{f}_{ij}) \mathbf{A}_{ij}. \quad (3.19)$$

$\phi(\mathbf{f}_{ij})$ is ϕ at A_{ij} ’s centroid, and can be estimated by appealing to geometric properties of Voronoi cells (see Springel (2010a) Sec 3.1). The temporal gradient is determined by relating it to the spatial gradient using the Euler equations. Finally, the flux is resolved from $\mathbf{W}_{\text{L,R}}^{\text{interface}}$ with a Riemann solver (in all our simulations, HLLD; Miyoshi & Kusano 2005). Eqns. 3.18 and 3.19 were replaced in Pakmor et al. (2016) order to resolve AREPO’s angular momentum conservation issue (Sec. 3.3), but the overall flux calculation procedure remains the same as above.

The self-gravity term \mathbf{G} from Eqn. 3.2 can easily be added to the flux calculation, since, when using \mathbf{W} , gravity only changes the momentum. This change, and the corresponding one for kinetic energy, can then be appended to \mathbf{Q} (Springel 2010a Sec. 5.2).

The advantages of AREPO – automatic adaptive resolution enhancement, Galilean invariance, accurate shock capture, low velocity noise and artificial viscosity in smooth flows, and a natural coupling to particle-based gravity solvers – make it an excellent platform with which to simulate mergers.

For the simulations in this chapter, we set $\mathbf{B} = 0$, reducing AREPO to a purely hydrodynamic simulation (Ch. 4 considers the magnetohydrodynamic case). We use the same Helmholtz EOS in AREPO that we installed into GASOLINE and also ignore composition gradients and any nuclear reactions. To assure a reasonably constant mass resolution (and other, similar criteria), we use an explicit refinement scheme (Vogelsberger et al. 2012) that adds or subtracts mesh-generating points to the grid. This keeps cell masses near a fixed value, and keeps all cell volumes within one order of magnitude of each other.

3.2.4 Initial Conditions and Completion Time

Our chosen WD masses are typical of the narrowly peaked empirical mass distribution of field CO WDs (Tremblay & Bergeron 2009; Kleinman et al. 2013). As in Z13, we generated WDs by rescaling a sphere of particles to the proper enclosed mass-radius relation determined from 1D hydrostatic integration. We used a 50% C, 50% O composition by mass uniform throughout the star, and assumed a uniform temperature of 5×10^6 K. The stars were placed into GASOLINE for approximately 11 dynamical times (33.3 s for the $0.625 M_\odot$ WD and 31.3 s for the $0.65 M_\odot$ WD). Thermal energy and particle velocity were damped to $\sim 5 \times 10^6$ K and 0 cm s^{-1} during the first dynamical time, and left free during the remaining 10 dynamical times. 64 neighbours, rather than 100, were used during relaxation to

minimize the number of particle pairs generated. These pairs (ex. Dehnen & Aly 2012, Springel 2010b) do not change global properties of the relaxed WDs, but do effectively reduce spatial resolution and having too many of them make transferring SPH initial conditions into AREPO problematic. Following relaxation, the density profile of both stars were consistent with the hydrostatic equilibrium solution, with the numerical central densities deviating from the 1D integrated ones by less than 1%. Since all particles have identical mass, the tenuous outer layers of the WDs are difficult to capture in GASOLINE; consequently the radii of the relaxed stars, as defined by the outermost particle, were $\sim 4\%$ smaller than the integrated ones. Even after energy damping, particle noise prevents the central temperature of the relaxed stars from reaching below $\sim 1 \times 10^7$ K, so all particle temperatures were artificially reset to $\sim 5 \times 10^6$ K.

We then placed the relaxed stars in a circular, unsynchronized binary, with initial separation $a_0 = 2.2 \times 10^9$ cm chosen (using the approximation of Eggleton 1983) so that the $0.625 M_\odot$ donor will just overflow its Roche lobe.³ The corresponding orbital period is 49.5 s. These initial conditions do not account for the tidal bulges of the stars, and so are not fully equilibrated (eg. Dan et al. 2011). While this means our initial conditions do not reflect “real” CO WD binaries with complete accuracy, we stress that the purpose of this work is to discover any code dependence on merger evolution, rather than providing the final word in WD merger simulations.

We generate initial conditions in AREPO by converting the SPH particles of the GASOLINE initial conditions into mesh-generating points, while retaining their conservative quantities (mass, momentum and energy). These initial conditions are not guaranteed to be regular, but AREPO regularizes the mesh over just a few timesteps by nudging each cell’s mesh-generating points to their cell’s center of mass.

Our SPH particles all have the same mass of 2×10^{27} g (1.3×10^6 particles represent the system), comparable to the highest resolutions used in other recent work (Pakmor et al. 2012; Raskin et al. 2014). We likewise use the AREPO refinement scheme’s to keep cell masses within a factor of 2 of this value, and to keep adjacent cell volumes to within a relative factor of 10. AREPO’s grid refinement scheme naturally increases the resolution of our simulations over time, though, and so all resolutions stated in this work are for the start of the simulation. We additionally initialize a background grid of 10^{-5} gcc cells in AREPO to fill the vacuum surrounding the WDs – this adds only $\sim 0.005 M_\odot$ of material to the simulation. Consequently, our spatial resolution in GASOLINE is about a factor of 3 lower than that in AREPO but because the two codes differ so greatly regardless of resolution, we believe equivalent mass resolution to be the most appropriate comparison (see Vogelsberger et al. Sec. 2.3 for complications in achieving equivalent accuracy in SPH and grid codes). In Sec. 3.5.1 we check if our results are resolution-dependent.

We run both simulations to 1000 s, as the WDs have merged long before (at ~ 200 s) this time. However, as we shall see in Sec. 3.4, the AREPO simulation continues its hydrodynamic evolution long after this time.

3.3 Improving Angular Momentum Conservation in Arepo

Before we move onto our current results, we summarize the discovery and resolution of a critical angular momentum conservation issue in AREPO.

³The 1D integrated radius was used to calculate a_0 , rather than the smaller relaxed SPH radius. This accounts for the small differences in initial conditions between this work and the equivalent simulation in Z13.

The first simulation we performed in AREPO showed dramatic differences from our GASOLINE ones. In it, the $0.625 M_{\odot}$ donor WD was destroyed by tidal forces within ~ 3 orbital periods (~ 150 s), versus the GASOLINE simulation’s ~ 4 (~ 200 s). Following the final phase of the merger, when the two WDs coalesce into one, the AREPO merger remnant featured a dense, crescent-shaped region formed from accretor material that retained its pre-merger temperature of $\lesssim 10^7$ K, while the GASOLINE remnant was relatively hot throughout its interior, with an average temperature of $\sim 2 \times 10^8$ K. Most prominently, the GASOLINE becomes axisymmetric within several hundred seconds after the merger, while the AREPO remnant maintained the integrity of its non-axisymmetric crescent while launching one, and then multiple trailing spiral waves into the surrounding medium.

In the top panel of Fig. 3.2, we show the evolution of the total z -axis angular momentum (top cluster of lines), $L_{z,\text{tot}}$, for low-resolution (1×10^{28} g particles/cells) and standard-resolution (2×10^{27} g) GASOLINE and AREPO simulations. We also show the angular momentum within a cylinder oriented along the rotational axis with radius $\omega = 10^9$ cm, $L_{z,\omega < 9}$, which represents the angular momentum within the dense core of the merger remnant. Because coalescence occurs at different times between them, each simulation’s curve is shifted by $t_{\max(L_z)}$, the time in each simulation when $L_{z,\omega < 9}$ achieves its maximum value (a rough proxy for the end of coalescence) to synchronize the start of post-merger evolution. We see that, over $\sim 10^3$ s, the $L_{z,\omega < 9}$ of the AREPO remnant at both resolutions drop by a factor of ~ 20 , behavior not reproduced by the GASOLINE runs. The spiral waves generated by the crescent in AREPO are a mechanism for transporting angular momentum (eg. [Papaloizou & Lin 1995](#); [Balbus 2003](#)) and were initially presumed to be the cause of this remnant spin-down. Global angular momentum in AREPO, however, is not conserved: the low-resolution run loses a *third* of its angular momentum over ~ 1000 s, and the standard-resolution one $\sim 20\%$. SPH formally conserves angular momentum, and we find the $L_{z,\text{tot}}$ for GASOLINE varies in time by $\lesssim 10^{-5}$ from its mean values at either resolution.

A moving mesh that refines in regions of high density may not properly resolve the disk of the merger remnant (which carries much of its angular momentum). To better pinpoint where the angular momentum was being spuriously lost, we computed (similar to [Ji et al. \(2013\)](#) Sec. 2.2.4) the theoretically expected change in L_z . For a cylinder V oriented along the rotational axis, this is given (via the Euler equations) by

$$\frac{\partial L_z}{\partial t} = - \oint_V \rho \omega v_\phi v_\omega dS + \int_V \omega \times \nabla \Phi dV \quad (3.20)$$

where the first term encapsulates advection (including wave motion; eg. [Balbus 2003](#)) out of the volume and the second term external torque – in our case gravitational.⁴ Subtracting the time-integral of Eqn. 3.20 (i.e. the cumulative angular momentum change ΔL_z) from the volume’s angular momentum gives us the “balance”

$$L_{\text{bal}}(t) = L(t) - \Delta L_z = L(t) - \int_{t_0}^t \frac{\partial L_z}{\partial t'} dt'. \quad (3.21)$$

In a system with perfect angular momentum conservation, $L_{\text{bal}}(t) = L_{\text{bal}}(t_0)$. In Fig. 3.2, we show using dashed lines the L_{bal} for the cylinder of $\omega = 10^9$ cm ($L_{\text{bal}}(\omega < 10^9 \text{ cm})$) for each of the four simulations. While $L_{\text{bal}}(\omega < 10^9 \text{ cm})$ decreases by $\sim 5\%$ for the GASOLINE simulations (likely due to

⁴A third, pressure torque term also arises in general, but for a cylinder oriented along the axis of rotation it is analytically zero (and numerically negligible as well).

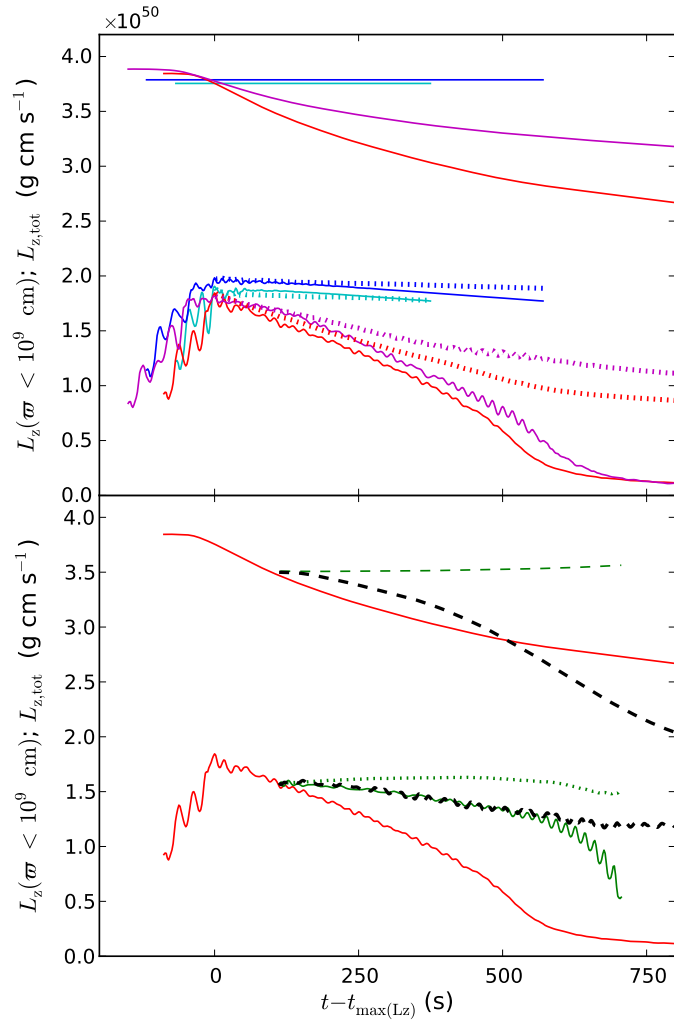


Figure 3.2: Evolution of total z-axis angular momentum $L_{z,\text{tot}}$ (top cluster of lines in each panel) and that within a cylinder of radius $\varpi = 10^9 \text{ cm}$, $L_{z,\varpi < 9}$ (bottom cluster), for various simulations in 2013-2014, before AREPO was updated to better conserve angular momentum. All curves are shifted in time by $t_{\max(L_z)}$, the time in each simulation at which $L_{z,\varpi < 9}$ achieved its maximum value, to synchronize the start of post-merger evolution. In the top panel, red and magenta lines represent the low and standard-resolution AREPO simulations, respectively, while the cyan and blue ones represent low and standard-resolution GASOLINE ones, respectively. Dotted lines represent angular momentum balance $L_{\text{bal}}(\varpi < 10^9 \text{ cm})$, which should be flat in the absence of spurious angular momentum losses. (Slightly different initial amounts of total angular momentum between AREPO and GASOLINE runs are due to inconsistencies in their initial conditions that have subsequently been solved.) In the bottom panel, the red line is again the low-resolution AREPO simulation, while the green line is for an AREPO low-resolution run where the mesh is held static after $t = 114 \text{ s}$. The dashed black line is a FLASH simulation that uses the AREPO low-resolution run at $t = 114 \text{ s}$ for initial conditions; its loss of total angular momentum is due to having outflow boundaries.

artificial viscosity, not included in Eqn. 3.20), the change in L_{bal} accounts for approximately *all* of the total spurious losses in AREPO (compare the $L_{z,\text{tot}}$ and L_{bal} lines), invalidating the hypothesis that it is the outer regions of the simulation spuriously losing angular momentum.

We then hypothesized that low-density regions near $\omega = 10^9$ cm that interact with the remnant core were underresolved. To rectify this, we performed a run which included a additional volume refinement scheme after coalescence for cells within $\omega = 10^9$ cm. This translated to a dramatic increase in resolution over time, with the simulation eventually exceeding 2×10^7 grid points. This run loses $\sim 5\%$ of $L_{z,\text{tot}}$ in ~ 500 s, but $\sim 30\%$ of $L_{z,\omega < 9}$ is still spuriously lost over the same timespan, meaning losses would only be rendered negligible at impractically high resolutions.

We then turned to simulating post-merger evolution in other codes. In the bottom panel of Fig. 3.2, we plot our simulation in the Eulerian code FLASH (Fryxell et al. 2000, using the low-resolution AREPO run at $t = 110$ s (chosen to be ~ 2 orbital periods after coalescence) for initial conditions. In FLASH we used a 3D Cartesian grid of size 1.6×10^{10} cm to a side, with multiple levels of fixed-mesh refinement centered on the merger remnant so that its core is resolved with cells 7.8×10^6 cm to a side (comparable to the low-resolution AREPO run). Gravity was solved using a multiple solver with $l_{\text{max}} = 50$, and fluxes propagated with the HLLC Riemann solver. We also plot a low-resolution AREPO run where, at $t = 110$ s the mesh's velocities were forced to zero, transforming AREPO into a static grid code operating on an unstructured mesh. Considering the sheer number of differences between the two simulations, they agree remarkably on the rate of change of $L_{z,\omega < 9}$ until very late times (when mesh drift issues corrupt the AREPO simulation). $L_{\text{bal}}(\omega < 10^9$ cm) for the AREPO-static run also changes by $\sim 1\%$ over ~ 500 s. These simulations suggested AREPO's moving mesh scheme cause spurious angular momentum losses.

Eventually, Pakmor et al. (2016) found two aspects of AREPO's original hydrodynamic scheme (Sec. 3.2.3) were responsible for making the code only *first-order* convergent for non-trivial moving meshes. First, while Eqn. 3.18 provides second-order convergence on static meshes of arbitrary geometry, it only uses the initial state of the mesh itself, and so only provides first-order convergence on moving meshes. Second, AREPO's estimate for $\phi(\mathbf{f}_{ij})$ in Eqn. 3.19 assumes that the cell centers of mass \mathbf{s} – where the value of \mathbf{W} is defined – and mesh-generating points \mathbf{r} align, which is untrue for elongated cells. This first-order convergence does not inevitably cause major errors – the galaxy formation study of Marinacci et al. (2014) is not affected, for example – but for a rotation-dominated system being simulated over hundreds of dynamical times, such as the accretion disk in Pakmor et al. (2016), systematic deviations in angular momentum conservation become large.

The solution is also two-fold: first, replace Eqns. 3.16 and 3.18 by a hybrid MUSCL-RK2 method:

$$\begin{aligned} \mathbf{W}'_i &= \mathbf{W}_i^n + \Delta t \frac{\partial \mathbf{W}}{\partial t} \\ \mathbf{r}' &= \mathbf{r}^n + \Delta t \mathbf{w}^n \\ \mathbf{Q}_i^{n+1} &= \mathbf{Q}_i^n - \frac{\Delta t}{2} \left(\sum_j A_{ij}^n \hat{\mathbf{F}}_{ij}^n(\mathbf{W}^n) + \sum_j A'_{ij} \hat{\mathbf{F}}'_{ij}(\mathbf{W}') \right) \\ \mathbf{r}^{n+1} &= \mathbf{r}', \end{aligned} \quad (3.22)$$

where \mathbf{r} is the coordinate of the mesh-generating point. With this method, we first make a prediction of the cell's future primitive variables \mathbf{W}' , as well as the future Voronoi mesh. We then use both the

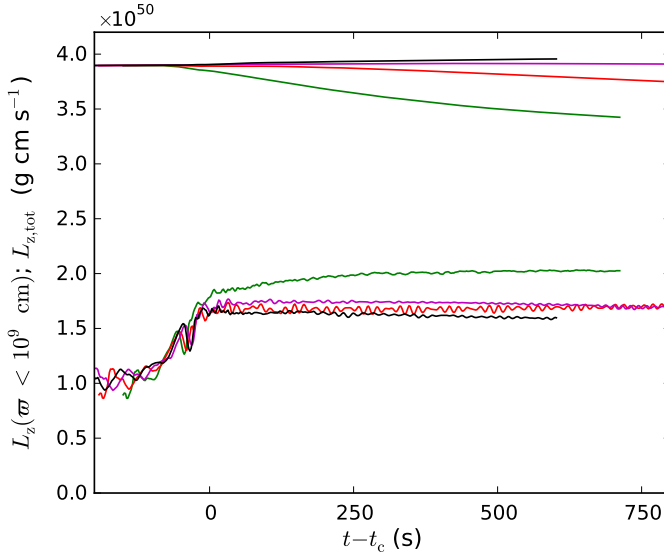


Figure 3.3: Evolution of total z -axis angular momentum $L_{z,\text{tot}}$ (top cluster of lines) and that within a cylinder of radius $\omega = 10^9 \text{ cm}$, $L_{z,\omega < 9}$ (bottom cluster) for the AREPO-RKLSF simulations. All curves are shifted in time by t_c (rather than $t_{\max(L_z)}$), the time when average separation between donor and accretor material reaches a tenth of its initial value. Colors indicate initial resolution: green is for 5.1×10^4 cells, red for 2.5×10^5 , magenta for 1.3×10^6 and black for 2.5×10^6 .

current and predicted values to calculate an average flux (spatial extrapolation to the cell interface is implicit when calculating \hat{f}_{ij}) and time-evolve the cell. The mesh velocities are assumed to be constant over Δt , so the predicted and true future mesh are identical. Second, the Green-Gauss gradient estimate is replaced with linear least-squares estimator, where slope $\langle \nabla \phi \rangle_i$ is determined by minimizing

$$\sum_j g_j (\phi_j - \phi_i - \langle \nabla \phi \rangle_i (\mathbf{s}_j - \mathbf{s}_i))^2, \quad (3.23)$$

where $g_j \equiv A_{ij} / |\mathbf{s}_j - \mathbf{s}_i|^2$ is a weighting function. This estimate gives the value that best reproduces the change in ϕ when travelling from cell i to any of its neighbours, and relies only on cell centers of mass (and their values of \mathbf{W}), rather than mesh generating points. Working in concert, these “RKLSF” fixes make AREPO second-order convergent.

In Fig. 3.3, we show the evolution of $L_{z,\text{tot}}$ and $L_{z,\omega < 9}$ for AREPO-RKLSF runs (from Sec. 3.5.1) at resolutions ranging from 5.1×10^4 to 2.5×10^6 cells. We immediately notice that $L_{z,\omega < 9}$ no longer decreases with time, cementing the fact that the rapid spin-down seen in Fig. 3.2 was an artefact of spurious angular momentum losses. Indeed, this makes it impossible to calculate $t_{\max(L_z)}$! We instead use “ t_c ”, the time when average donor-accretor separation reaches a tenth of its value at the start of the simulation (see Sec. 3.4), to synchronize the curves. In all but the lowest-resolution run, $L_{z,\text{tot}}$ deviates by less than $\sim 7\%$ from its initial value, and at the highest-resolution run of 2.5×10^6 cells, it deviates by $\sim 1\%$ over ~ 840 s, an order of magnitude better than the 2×10^7 -cell simulation without the RKLSF implementation.

We now compare these AREPO-RKLSF simulations against ones in GASOLINE.

3.4 Results

Fig. 3.4 compares snapshots at various times in the GASOLINE and AREPO simulations.

The initial evolution of the two systems, shown in row 1 of Fig. 3.4, is qualitatively similar. Our initial conditions are approximate, so both stars immediately tidally stretch in response to the binary potential, overshooting their Roche lobes in the process and transferring mass to each other in spurts. This eventually dies down for the $0.65 M_{\odot}$ accretor, and becomes steady mass transfer for the $0.625 M_{\odot}$ donor, just prior to it becoming fully disrupted. In reality, the $0.625 M_{\odot}$ donor WD should overflow first and begin a period of quasi-stable mass transfer over potentially dozens of orbits, and so our simulations, both of which experience donor full disruption in just a few orbits, overestimate the rate of early mass transfer (Dan et al. 2011).

The accretion streams in both codes are travelling at supersonic speeds ($\mathcal{M} \approx 2$) relative to the accretor when they impact, and as a result the streams shock-heat at impact and their material rapidly thermalize. By the time the donor is fully disrupted a hot atmosphere has formed around the accretor. This atmosphere has a temperature of 1.6×10^8 K in AREPO and 1.9×10^8 K in GASOLINE – both about half of the virial temperature, $GM_a m_P / 3R_a k_B \approx 4 \times 10^8$ K – with corresponding densities of 1.8×10^5 g cm $^{-3}$ and 2.3×10^5 g cm $^{-3}$, respectively. As seen in Fig. 3.4 row 1, AREPO’s hot atmosphere is somewhat less extended and tends to have more localized hotspots in temperature compared to the extended and uniform one in GASOLINE. This may be due to a combination of AREPO being better able to capture underdense regions **DISCUSS WHY EARLIER!**, and having higher local spatial resolution for the same mass resolution

As mass transfer continues to expand the donor and draw it closer to the accretor, eventually tidal forces between the two WDs are strong enough to fully disrupt the donor, stretching it out into a thick stream of material that wraps around the donor, as seen in Fig. 3.4 row 1. In both simulations, this occurs ~ 3.7 orbital periods of the initial binary, or ~ 180 s, after the start of simulation, by which time the donor has transferred $\sim 0.05 M_{\odot}$ to the accretor. During coalescence, both the density and temperature profiles appear very similar between the codes, and the destruction of the donor takes over the same amount of time – about one orbital period, or 49.5 s – in both codes.

Once the donor is fully disrupted, and coalescence begins, a portion of it forms an accretion stream that slides across the accretor at supersonic speeds, creating a string of Kelvin-Helmholtz vortices. In AREPO these vortices are markedly more pronounced, being both larger by $\sim 30\%$ in radius, and having a slightly higher temperature of $\sim 5 \times 10^8$ K compared to GASOLINE’s $\sim 4 \times 10^8$ K. The accretion stream continues to inspiral toward the center of the accretor, severely deforming the accretor while carrying the string of Kelvin-Helmholtz vortices toward the center of the system. Meanwhile, the remainder of the donor material increases its average distance from the accretor (conserving total angular momentum), wrapping around it as a thick sub-Keplerian disk. The two WDs have nearly equal masses, so material near the surface of the accretor is dredged up to become part of the disk, while the incoming donor accretion streams severely disrupt the accretor from a sphere into a crescent shape. Coalescence is approximately complete when the average separation between material from the donor and accretor changes from its initial value of 2.2×10^9 cm to its equilibrium value of $\sim 1 - 2 \times 10^8$ cm. We thus estimate the time coalescence is complete, t_c , by determining the time when average donor-accretor separation reaches a tenth of its initial value. We find $t_c = 228$ s for GASOLINE, and 220 s (roughly Fig. 3.4, row 3).

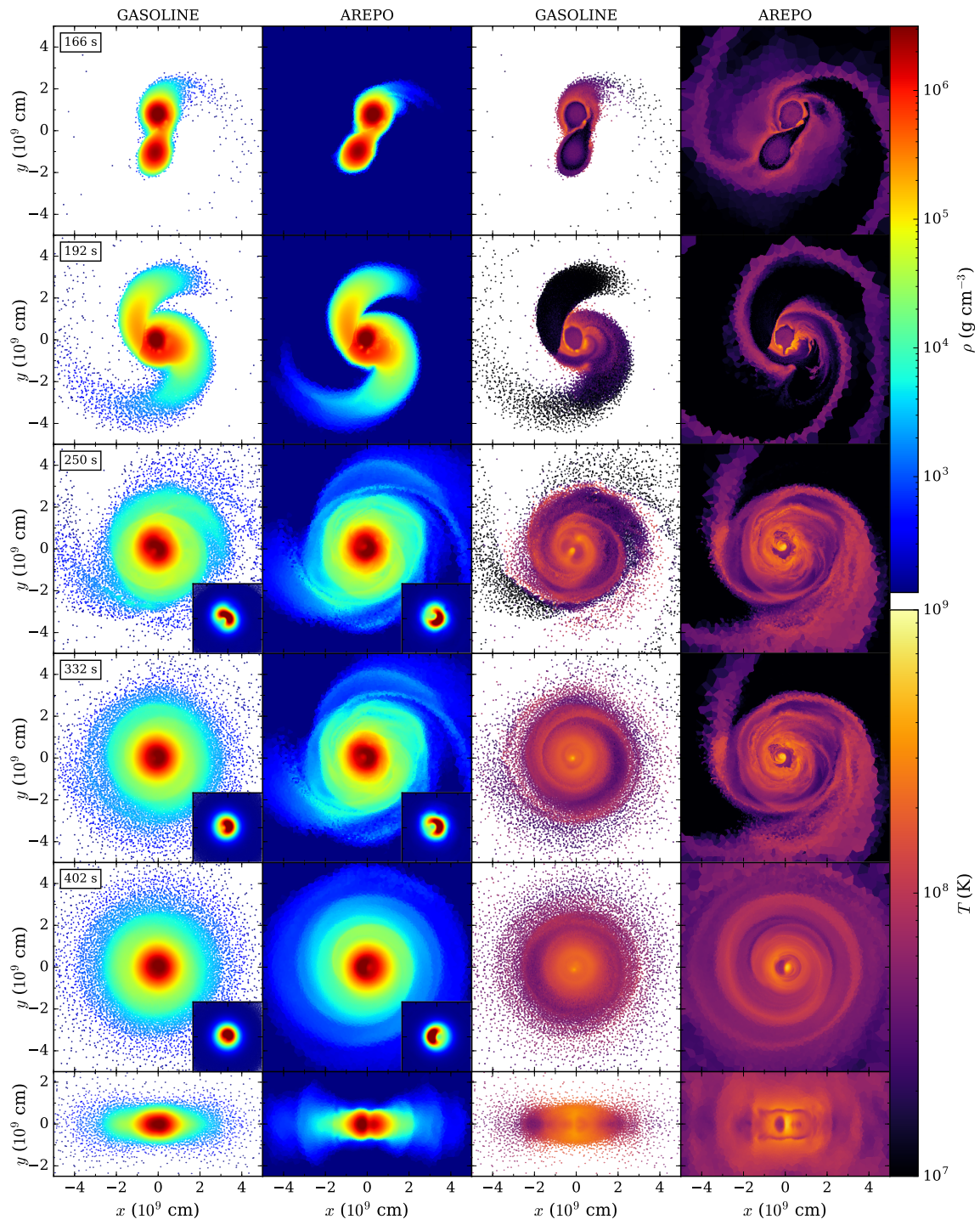


Figure 3.4: Series of equatorial (xy) plane density (left two columns) and temperature (right two columns) intensity plots for five snapshots in time (rows; the time for each snapshot is indicated at the top left of the density plots) during the GASOLINE and AREPO simulations. xz-plane plots are also included for the final snapshot.

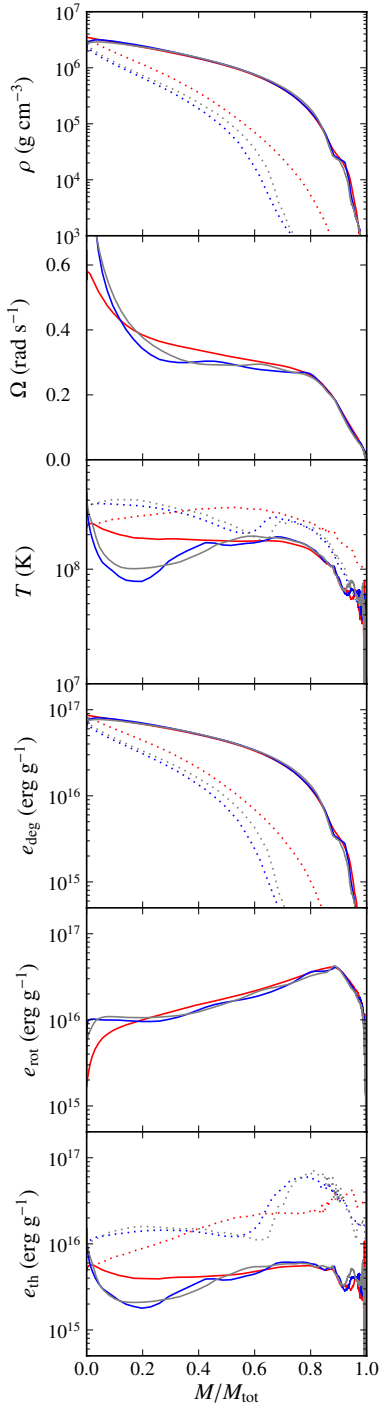


Figure 3.5: Merger remnant profiles from the GASOLINE (red), AREPO (blue) and AREPO MHD (gray; Zhu et al. 2015) simulations 99 s after coalescence (around row four of Fig. 3.4). The profiles are, from top to bottom, density ρ , angular rotation speed Ω , temperature T , specific degeneracy energy e_{deg} , specific thermal energy e_{th} , and specific rotational energy e_{rot} , all as a function of the ratio of spherical enclosed to total mass M/M_{tot} . Solid lines represent profiles on the original binary's orbital plane, while dash-dotted lines represent profiles along the rotational axis.

In Fig. 3.5, we plot profiles of density, temperature and energy for the merger remnants 99 s (2 orbital periods) after coalescence, roughly equivalent to row 4 of Fig. 3.4. Profiles both along the original plane of the merger, or “equatorial plane” (solid lines) and rotational axis are considered, and like Z13 we map ω and z positions to the ratio of corresponding spherical enclosed mass to total mass M/M_{tot} . The equatorial profiles are axisymmetrically averaged, while the rotational axis ones are averaged from the profiles above and below the equatorial plane. As a whole, the two remnants have very similar structures: both feature a degeneracy-supported core surrounded by a rotationally supported thick disk along the equatorial plane (plane of the original binary), and by a hot, thermally supported atmosphere along the axis of rotation. Following Z13 Sec. 3.2.3, we find the disk mass $M_{\text{disk}} = 0.23 M_{\odot}$ and the core-envelope mass $M_{\text{ce}} = 1.05 M_{\odot}$ in both simulations, though we note that the core-envelope also has substantial rotational support throughout.⁵ Both remnant’s internal energy (1.5×10^{50} erg) is also identically divided into $\sim 30\%$ rotational, $\sim 10\%$ thermal and $\sim 60\%$ degeneracy energy. One minor difference between the two codes is the total amount of material unbound by the merger – $1.4 \times 10^{-3} M_{\odot}$ in GASOLINE, and $5.0 \times 10^{-3} M_{\odot}$ in AREPO – though this value is much smaller and harder to constrain than the bulk values above.

The simulations’ profiles in Fig. 3.5 are likewise very similar in shape to one another: both, for example, have a peak density of $\sim 3 \times 10^6$ g cm $^{-3}$ and a large fraction of their mass rotating nearly rigidly at $\sim 0.3 \text{ s}^{-1}$. We also plot the AREPO MHD simulation from Zhu et al. (2015) in grey, and find it is also similar to both simulations, indicating that including magnetic dynamo effects lead only to minor changes in the *hydrodynamics* in the merger. The greatest discrepancy is in the factor of ~ 2 decrease in the temperature curve at small M/M_{tot} in the AREPO simulation.

That discrepancy, however, reflects a larger evolutionary difference visible in rows 4 - 6 of Fig. 3.4. Just after coalescence, the center of the merger remnant in both simulations is clearly divided into a dense and cold crescent-shaped region, formed from the perturbed core of the accreting WD, and a low-density void that is an order of magnitude hotter, formed by material roughly evenly mixed between donor and accretor (this hot void appears as a column in the xz plots of Fig. 3.4). 99 s after coalescence, the hot void has a density and temperature of $\sim 2 \times 10^6$ g cm $^{-3}$ and $\sim 6 \times 10^8$ K, respectively, in both codes, but the AREPO void is $\sim 80\%$ larger in radius. The cold crescent, meanwhile, has a density of $\sim 4 \times 10^6$ g cm $^{-3}$ in both codes, but has a temperature of $\sim 2 \times 10^8$ K GASOLINE versus $\sim 5 \times 10^7$ K in AREPO. Over the next several hundred seconds, the GASOLINE remnant’s crescent deforms and becomes axisymmetric, eliminating the hot void in the process; material from the void moves off of the equatorial plane to form two $\sim 3.5 \times 10^8$ K hotspots along the rotational axis (row 6 of Fig. 3.4). By $t \approx 500$ s, the GASOLINE remnant structure – an oblate spheroidal core with a roughly uniform temperature of $\sim 2 \times 10^8$ K (outside of the hotspots) and surrounded by a stubby disk – has stopped evolving on a hydrodynamic timescale (roughly equal to one binary orbital period). AREPO, on the other hand, maintains the distinction between its crescent and void, and consequently remains non-axisymmetric, for more than a thousand seconds after coalescence. The system’s center of rotation and mass coincide at the midpoint along the boundary between the crescent’s interior edge and the hot void, and most of the dense crescent actually revolves around this point (rather than spinning about it). This generates a lopsided gravitational potential that perturbs the surrounding disk, launching a single spiral wave into the surrounding medium.

⁵The mass of material whose degeneracy specific energy is $> 50\%$ of their total specific energy is $\sim 0.8 M_{\odot}$ in both simulations, as in Zhu et al. (2015).

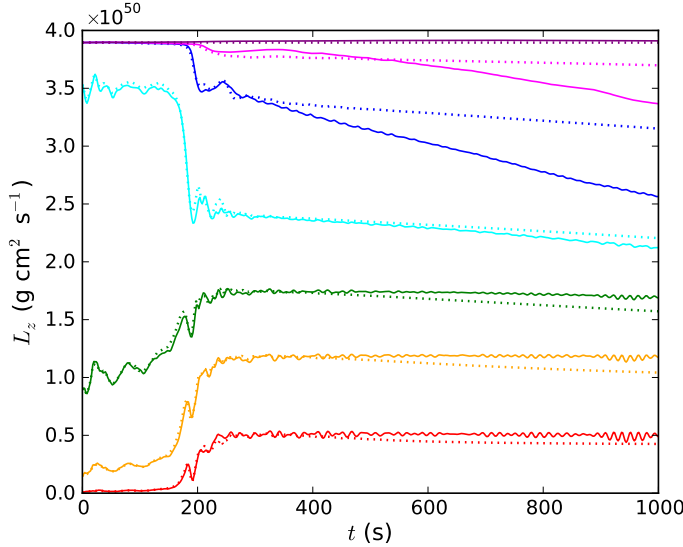


Figure 3.6: Time evolution of z -axis angular momentum L_z for AREPO (solid lines) and GASOLINE (dotted) simulations. The purple line represents total L_z , while the others represent angular momentum within concentric cylinders aligned along the rotation axis and with radii $\omega = 5 \times 10^8$ (red), 7.5×10^8 (yellow), 1×10^9 (green), 1.5×10^9 (cyan), 3×10^9 (blue) and 6×10^9 cm (magenta).

Since spiral waves transport angular momentum, we show the evolution of z -axis angular momentum L_z within concentric cylinders in Fig. 3.6 for the two simulations. We see that all cylinders slowly lose angular momentum after coalescence in the GASOLINE simulation, likely a consequence of artificial viscosity. The AREPO simulation’s L_z within $\omega = 10^9$ cm changes by less than $\sim 0.5\%$ over 1000 s. By contrast the $L_z(\omega < 3 \times 10^9$ cm) drops at a rate of $dL_z/dt = 1.2 \times 10^{47}$ g cm 2 s $^{-2}$ (compared to the of its GASOLINE equivalent of 3.3×10^{46} g cm 2 s $^{-2}$). The base of the spiral wave is at $\omega \approx 1.5 \times 10^9$ cm, which suggests the $L_z(\omega < 3 \times 10^9$ cm) curve probes the wave’s angular momentum transport. At ~ 1000 s, AREPO’s simulation still resembles row 6 of Fig. 3.4, indicating that the crescent structure is quasi-stationary and persists on a timescale approaching the post-merger viscous timescale calculated by van Kerkwijk et al. 2010 and Shen et al. (2012). The remnant disk has also transported over half of its angular momentum to much larger distances, suggesting it will spin down on a timescale of $\sim 10^3 - 10^4$ s, comparable to that for an α -viscosity disk with $\alpha \sim 10^{-1} - 10^{-2}$. We discuss the physical robustness and implications of this result in Sec. XXX.

3.5 Discussion

To determine the robustness of our results, and provide clues to the sources of the differences between AREPO and GASOLINE simulations, we ran a number of tests varying code parameters.

3.5.1 Resolution Test

As noted in Sec. 3.2.4, an AREPO simulation with identical mass resolution to a GASOLINE one will have roughly a factor of 3 higher spatial resolution because of the 100 neighbouring particles needed

by the kernel. It is possible that the differences we observe between our simulations are not due to fundamental differences between the codes, but because our GASOLINE simulation insufficiently resolves the merger. To address this, we performed a series of GASOLINE and AREPO simulations with a mass resolutions of 5×10^{28} g (equivalent to 5.1×10^4 particles/cells and comparable to resolutions used in parameter-space sweeps [Dan et al. 2012; 2014](#)), 1×10^{28} g (2.6×10^5) and 1×10^{27} g (2.6×10^6). This factor of 50 range in mass resolution (~ 4 in spatial resolution) allows us to both determine the degree to which mergers in each code change with resolution, and to can compare AREPO runs to GASOLINE ones at finer mass resolution.

At all four resolutions, the GASOLINE simulations exhibit very similar behaviour prior to coalescence. The donor fully disrupts in at ~ 3.5 orbits of the initial binary for the two higher resolution runs, while the two lower-resolution ones experience a slightly earlier disruption at ~ 3.2 orbits ($\sim 155 - 160$ s). Coalescence for the highest resolution run occurs at $t_c = 230$ s, within 2 seconds of the standard resolution value, while it occurs $15 - 30$ seconds earlier for the two lower resolution runs (we note the method we determine coalescence is somewhat sensitive to changes in the detailed configuration of the remnant). Just after coalescence, all reproduce the crescent-and-void configuration, with the void being least prominent in the lowest-resolution run. AREPO also reproduces the same qualitative evolution up to coalescence at all resolutions, but donor disruption occurs within only ~ 2 orbits at its lowest resolution, and in ~ 3 in its second lowest. The time of coalescence is likewise much sooner in the lowest resolution simulation, at $t_c = 150$ s for the lowest resolution run. The two higher resolution runs, however, are very similar to one another, with donor disruption occurring at ~ 180 s and $t_c = 234$ s, much closer to the standard resolution run's values. These differences are in part due to our initial conditions setup, where GASOLINE SPH particles are directly mapped to AREPO cells. WDs that are hydrostatic in GASOLINE are not precisely so in AREPO, particularly in the poorly resolved atmosphere, and we see the WDs spuriously expanding in the first few seconds. This effect leads to larger mass-transfer rates early in the merger, and is magnified with decreasing resolution. Just after coalescence, all reproduce the crescent-and-void configuration, with the void being least prominent in the lowest-resolution run.

In Fig. 3.7, we plot the equatorial and rotational axis profiles of all simulations 100 s after their time of coalescence. The GASOLINE remnants (left column) are all remarkably similar to one another, with the sole exception of the temperature structure at the lowest resolution. The disk and core-envelope masses as well as internal energy and its partitioning into various forms are all within 1% of their values at standard resolution reported in Sec. 3.4. The central density also deviates by $\lesssim 3\%$ from 3.6×10^6 g cm $^{-3}$ in all remnants. The AREPO remnants (right column) are less uniform: masses and energies vary by $\sim 10\%$ from their reported values in Sec. 3.4, and the central density ranges from $3 - 4 \times 10^6$ g cm $^{-3}$ for all resolutions except the lowest one, where it is $\sim 2 \times 10^6$ g cm $^{-3}$. The variations in the rotation and temperature curves reflect variations in the structure of the dense crescent and hot void. While at the highest two resolutions the dense crescent is clearly colder, with a temperature of $\sim 6 \times 10^7$ K, at a resolution of 1×10^{28} g the crescent's temperature is a much warmer 3×10^8 K, and at the lowest resolution the remnant's core never forms a crescent at all, instead appearing as a dumbbell-shaped object that transforms into a spherically symmetric one within 500 s of coalescence. During this time, global angular momentum decreases by ~ 10 (see Fig. 3.3), and a $< 10^7$ K ring of material spurious forms at the interface between donor and accretor, both indicating that the AREPO is too poorly resolved to simulate the merger. At all other resolutions, however, the crescent and void

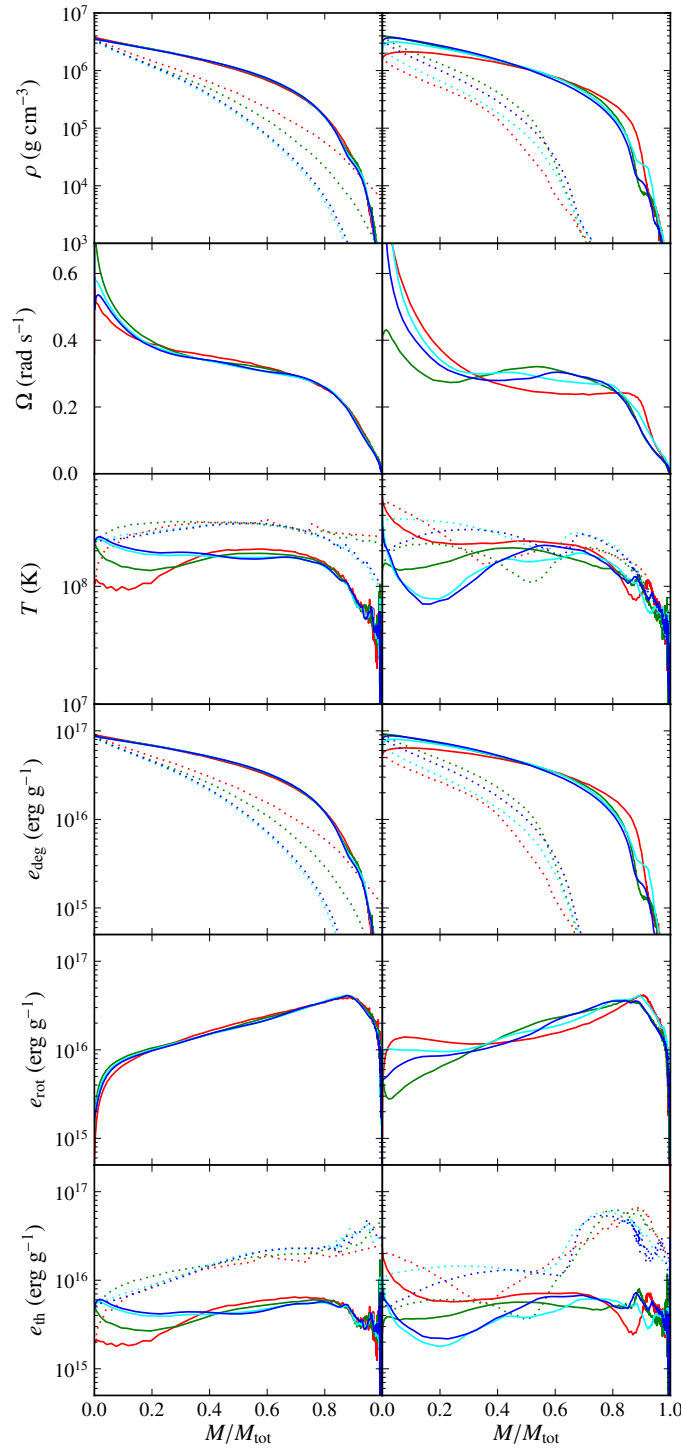


Figure 3.7: Merger remnant profiles, as in Fig. 3.5, for GASOLINE (left column) and AREPO (right) simulations of various (initial, for AREPO) mass resolutions. Resolutions include 5×10^{28} g (equivalent to 5.1×10^4 particles/cells; red lines), 1×10^{28} g (2.6×10^5 ; green) 2×10^{27} g (1.3×10^6 ; cyan) and 1×10^{27} g (2.6×10^6 ; blue).

survive until the end of the simulation at 1000 s.

The crescent-void configuration also appears, but then fades away over several hundred seconds, in all GASOLINE simulations. To check if the longevity of the configuration is resolution-dependent, we turn to Zhu et al. 2013’s measurement of non-axisymmetry, measured from $|f_1|/|f_0|$, the ratio of largest non-zero to zeroth Fourier coefficient of particles or cells binned in azimuth. For all simulations, the largest non-zero Fourier coefficient is the first, and the time the hot void disappears the remnant roughly matches the time t_f when $|f_1|/|f_0| = 0.01$. We find, from lowest to highest resolution, $t_f = 425$ s, 483 s, 515 s and 513 s – roughly corroborated by visual inspection of the remnant’s non-axisymmetry – that suggests convergence at $t_f \approx 510$ s. Note that all AREPO simulations maintain $|f_1|/|f_0| \gtrsim 0.1$ for $\gtrsim 1000$ s, except (unsurprisingly) for the lowest-resolution run, which drops to $|f_1|/|f_0| \approx 0.02$ by the end of the simulation.

We thus conclude that the largest difference between the GASOLINE and AREPO simulations – the survival of the crescent-void configuration long after the merger – is the case for all resolutions. The void persists for hundreds of seconds in all but the lowest-resolution AREPO simulations, while even in the highest-resolution GASOLINE one it smears away, disappearing within ~ 250 s after coalescence. This indicates that spatial resolution alone is insufficient to explain the diverging behavior of the codes. We also find that, curiously, that GASOLINE’s results change little between all resolutions, while AREPO’s results only appear to agree at the highest resolutions. This bodes well for merger parameter-space studies using lower-resolution SPH simulations (eg. Z13, Dan et al. 2014; ?; the latter finds in their resolution study similar results unless nuclear burning becomes important during the merger), but the same study would require a mass resolution finer than $\sim 1 \times 10^{28}$ g in AREPO (and ideally closer to our standard resolution of 2×10^{27} g) to guarantee qualitative accuracy with higher-resolution runs.

Varying Viscosity in Gasoline

Artificial viscosity, which is essential in SPH for proper shock capture, has been a major issue for white dwarf merger simulations for decades (eg. Guerrero et al. 2004; Lorén-Aguilar et al. 2009) because it spuriously shears differential rotation into rigid rotation, dumping excess energy into heat. This viscosity cannot simply be mitigated by resolution Springel (2010b), and we cannot run our mergers with zero artificial viscosity without neglecting shock heating and introducing unphysical particle behaviour. We can, however, increase and reduce its strength to see what effect it has on our simulation results, as in Z13 Sec. XXX.

We ran GASOLINE simulations of our merger with a mass resolution of 1×10^{28} g and time-independent artificial viscosity coefficients of either $\alpha = 0.05$, $\beta = 0.1$, or $\alpha = 1$, $\beta = 2$ (the Balsara switch is still active), comparing them to the variable-viscosity run at the same resolution in Sec. 3.5.1. These simulations both experience donor disruption after ~ 3.2 binary orbits, similar to the variable one, and coalescence occurs at 205 s and 219 s for the low and high-viscosity runs, respectively. This similarity is to be expected, since mass transfer and donor disruption are governed by tidal forces, which are unchanged between the simulations. During coalescence, the evolution of the variable and high-viscosity runs is similar, except that the accretor becomes about twice as hot. In the low-viscosity run, however, the donor’s accretion stream produces a contiguous hot ring around the accretor during coalescence, rather than the string of vortices seen in row 2 of Fig. ??, and perturbs the accretor far less. As a result, no distinct void ever forms, though the remnant core is distorted into a bean shape. Within ~ 25 s of coalescence, the void in the high-viscosity simulation is already fast-disappearing,

having a radius less than half of that of the variable-viscosity run. $t_f = 358\text{ s}$ and 486 s for the high and low-viscosity runs, respectively, compared to 483 s for the variable one. The similarity of the latter two values is likely because the variable-viscosity run tends toward the same α and β values as the low-viscosity one in the absence of shocks. At $\sim 500\text{ s}$, the remnant has become axisymmetric in all three codes, but in the high-viscosity run the interior $\sim 0.8 M_\odot$ of the remnant is also rigidly rotating with $\Omega = 0.33\text{ s}^{-1}$, and features a nearly uniform temperature of $2 - 2.5 \times 10^8\text{ K}$.

As expected, then, the high-viscosity simulation rapidly spins down to axisymmetry while eliminating differential rotation, showing that excess artificial viscosity contributes to the disappearance of the crescent-void configuration. The low-viscosity simulation, on the other hand, primarily shows the importance of increasing α and β during coalescence in order to properly capture shocks and shearing interactions between donor and accretor.

Chapter 4

Magnetized Moving Mesh Merger of a Carbon-Oxygen White Dwarf Binary

Chenchong Zhu, Rüdiger Pakmor, Marten H. van Kerkwijk, Philip Chang
The Astrophysical Journal Letters, Volume 806, Issue 1 - article id. L1, 5pp.,
2015 ([Z15](#))

While simulations of white dwarf mergers are numerous (Sec. ??), to date they have not included magnetic fields, even though they are believed to play a significant role in the evolution of the merger remnant. We simulated a $0.625 - 0.65 M_{\odot}$ carbon-oxygen WD binary merger in the magnetohydrodynamic moving mesh code AREPO. Each WD was given an initial dipole field with a surface value of $\sim 10^3$ G. As in simulations of merging double neutron star binaries, we find exponential field growth within Kelvin-Helmholtz instability-generated vortices during the coalescence of the two stars. The final field has complex geometry, and a strength $> 10^{10}$ G at the center of the merger remnant. Its energy is $\sim 2 \times 10^{47}$ ergs, $\sim 0.2\%$ of the remnant's total energy. The strong field likely influences further evolution of the merger remnant by providing a mechanism for angular momentum transfer and additional heating, potentially helping to ignite carbon fusion.

4.1 Introduction

The merging process has, in the last decade, been investigated with increasingly sophisticated 3D hydrodynamic simulations (Lorén-Aguilar et al. 2009; Pakmor et al. 2010; Dan et al. 2012; 2014; Raskin et al. 2012; Zhu et al. 2013; Moll et al. 2014). However, one fundamental piece missing in WD merger studies so far is magnetic fields.

Mergers (that do not immediately explode) are expected to produce remnants that are susceptible to magnetic dynamo processes such as the magnetorotational instability (MRI; Balbus & Hawley 1991), Tayler-Spruit dynamo (e.g. Spruit 2002), and the $\alpha\omega$ dynamo (if convection occurs in the inner disk; García-Berro et al. 2012). It has therefore long been suspected that they can generate strong fields, and recent 2D simulations of MRI in the remnant (Ji et al. 2013) have indeed shown amplification of a weak seed field to $> 10^{10}$ G. Magnetic shear from these fields transports angular momentum over a timescale of $\sim 10^4 - 10^8$ s (van Kerkwijk et al. 2010; Shen et al. 2012) – far shorter than the thermal timescale of the remnant – and also (non-locally) heats the remnant. The latter, combined with loss of rotational support from angular momentum transport, could push remnant temperatures past the point of carbon ignition ($\sim 6 \times 10^8$ K for densities between $10^5 - 10^7$ g cm $^{-3}$), leading to either stable nuclear burning or a runaway. This mechanism could potentially drive nuclear runaways even in remnants with masses below the Chandrasekhar Mass M_{Ch} that have traditionally been considered stable (van Kerkwijk et al. 2010).

While field growth after the merger has been explored, field growth *during* the merger is also expected, and can have a profound impact on the post-merger magnetic evolution. Magnetohydrodynamic (MHD) double NS binary merger simulations (eg. Price & Rosswog 2006; Kiuchi et al. 2014; Giacomazzo et al. 2015) have found that Kelvin-Helmholtz vortices produced along the shear interface between the coalescing stars can amplify field strengths by orders of magnitude (Obergaulinger et al. 2010; Zrake & MacFadyen 2013). The same should hold true for WD mergers. Motivated by this, we present the first MHD simulation of a CO WD binary merger.

This chapter is organized as follows: in Section 4.2, we describe AREPO and our initial conditions. The results of our simulation are in Section 4.3. In Section 4.4, we test our simulation’s robustness, and finally in Section 4.5 we discuss implications for merger outcomes and possible avenues for future research.

4.2 Methods

We employ the moving-mesh code AREPO (Springel 2010a), which solves the equations of ideal MHD on a Voronoi mesh coupled with self-gravity. We operate the code in its pseudo-Lagrangian mode, so that the mesh-generating points that define the Voronoi grid move with the local velocity of the fluid. To conserve angular momentum to within $\sim 2\%$ of its initial value, we use the latest improvements to time integration and gradient estimate (Pakmor et al. 2016). AREPO’s MHD implementation is described in Pakmor et al. (2011a) and Pakmor & Springel (2013); we use the Powell et al. (1999) eight-wave scheme for divergence control. Our simulation ignores outer hydrogen and helium layers, composition gradients, and nuclear reactions (negligible for sub- M_{Ch} CO WD mergers; Lorén-Aguilar et al. 2009; Raskin et al. 2012).

We model the merger of two CO WDs with masses of 0.625 and $0.65 M_{\odot}$, respectively, in a circular,

unsynchronized binary with initial separation $a_0 = 2.20 \times 10^9$ cm (corresponding period $P_0 = 49.5$ s), chosen (using the estimate of Eggleton 1983) such that the lower-mass WD just fills its Roche lobe. We chose masses typical of the narrowly peaked empirical mass distribution of field CO WDs (Kleinman et al. 2013). Our initial conditions are very similar to those of the $0.625 - 0.65 M_\odot$ binary simulated with smoothed particle hydrodynamics (SPH) in Zhu et al. (2013; henceforth Z13). As in Z13, both WDs are generated with a uniform initial temperature of 5×10^6 K (the corresponding thermal pressure is dynamically irrelevant) and a uniform composition of equal parts carbon and oxygen by mass. They are separately relaxed to hydrostatic equilibrium using the SPH code GASOLINE (Wadsley et al. 2004) and added to AREPO by converting the SPH particles to mesh-generating points while retaining their conservative quantities (mass, momentum and energy). A uniform 10^{-5} g cm $^{-3}$ background grid fills up a 10^{12} cm box centered on the binary. Each WD is given a (dynamically irrelevant) dipole seed magnetic field with an equatorial surface value of 10^3 G (and corresponding central field of $\sim 2 \times 10^7$ G). The fields are overlapped when the two stars are placed into a binary.

The mass resolution of our simulation is $m_{\text{cell}} \approx 1 \times 10^{-6} M_\odot$. We utilize explicit refinement and derefinement (Vogelsberger et al. 2012) to keep cell masses within a factor of two of $10^{-6} M_\odot$ and to ensure adjacent cells differ by less than a factor of 10 in volume.

4.3 Results

We depict the evolution of the binary in Fig. 4.1, highlighting temperature T and magnetic field strength $|B|$. Fig. 4.2 shows the growth of total magnetic energy E_B over time.

In the first stage of the merger, up to ~ 180 s, the $0.625 M_\odot$ donor WD transfers mass to the $0.65 M_\odot$ accretor for about 3.5 orbits before fully disrupting. Because our initial conditions are approximate – the WDs are not initially tidally deformed – mass transfer begins in spurts as the WDs stretch in response to the binary potential, and occurs at a rate that is artificially high (Dan et al. 2011). The early mass transfer shears the atmospheres of both WDs. As a result, E_B grows roughly linearly in the first ~ 100 s, reaching about quadruple its initial value. Since the initial mass transfer rate is artificially high, this growth is likely an overestimate, but remains negligible compared to what follows.

By ~ 120 s, mass transfer becomes steady, and a stream of material from the donor wraps around the accretor, forming a shear layer. Along it, the Kelvin-Helmholtz instability generates a string of hot vortices that exponentially amplify their entrained magnetic fields. This is illustrated in Fig. 4.1 (row 2), where the hot vortices along the donor-accretor interface correspond to regions of high field strength. At ~ 180 s, tidal forces between the two WDs become strong enough to fully disrupt the donor, which then coalesces with the accretor over ~ 50 s. During this time, infalling donor material spirals into the accretor, severely deforming the accretor while carrying the string of magnetized vortices toward the system’s center of mass (CM). Fig. 4.2 shows E_B growing exponentially by a factor of $\sim 10^7$ over ~ 100 s, with an e -folding time $\tau = 6.4$ s, comparable to the typical turnover timescale of the largest eddies $2\pi R_{\text{eddy}} / \Delta v_{\text{shear}} \sim 3$ s, where Δv_{shear} is the velocity difference across the shear layer.

By ~ 250 s many of the vortices have merged together into a hot, rapidly rotating underdense void at the CM (Fig. 4.1, row 4). Magnetic growth within the void begins to saturate as its magnetic and kinetic energy approach equipartition. The rate of field growth slows as well, with E_B growing another two orders of magnitude over ~ 150 s before plateauing at $\sim 2 \times 10^{47}$ ergs at ~ 400 s.

In Fig. 4.3 we show the density ρ , T , $|B|$ and ratio of magnetic to rotational energy density e_B/e_{rot}

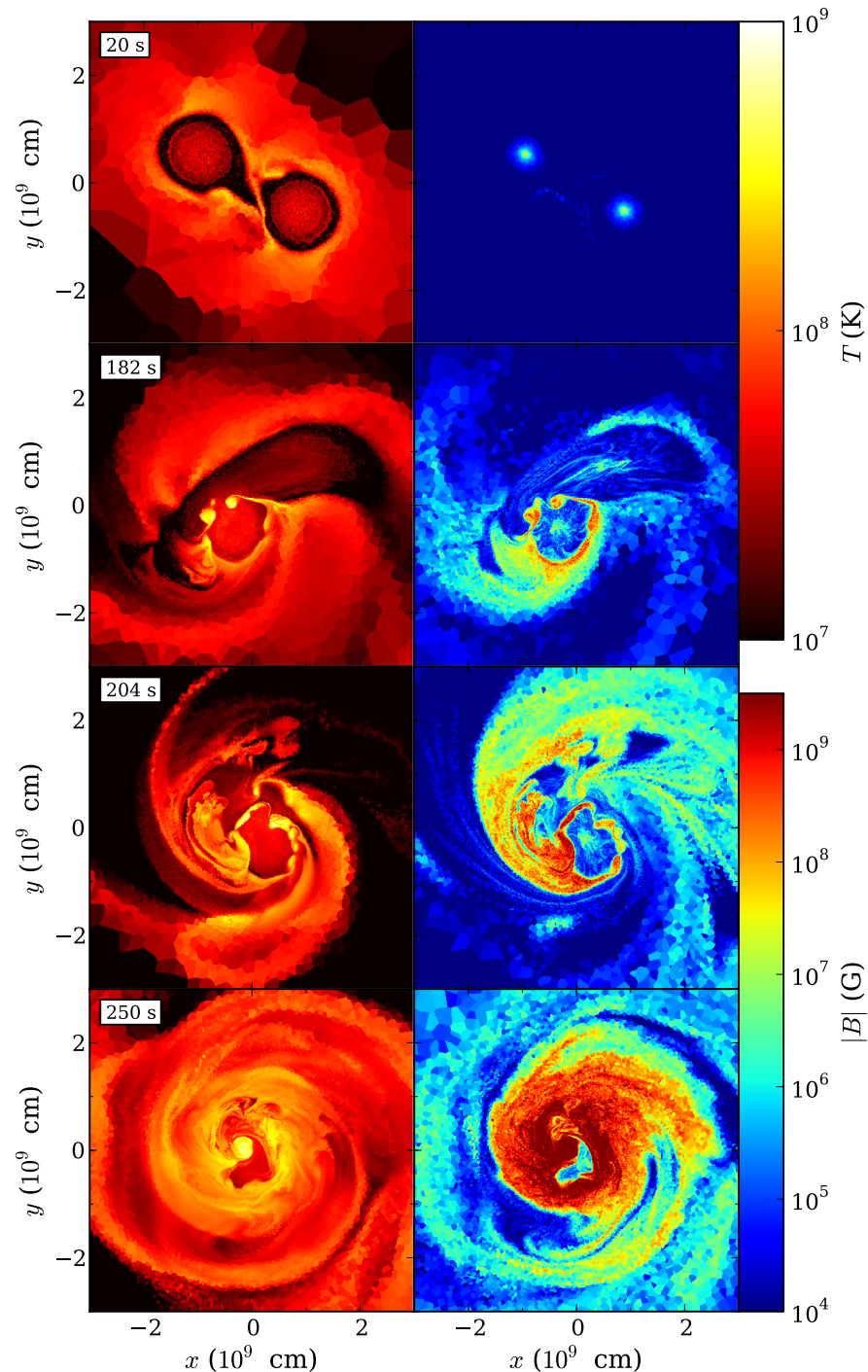


Figure 4.1: Series of temperature T (left column) and magnetic field strength $|B|$ (right) logarithmic intensity profiles in the equatorial plane of the merger for four snapshots in time (rows; time indicated at the top left of each row).

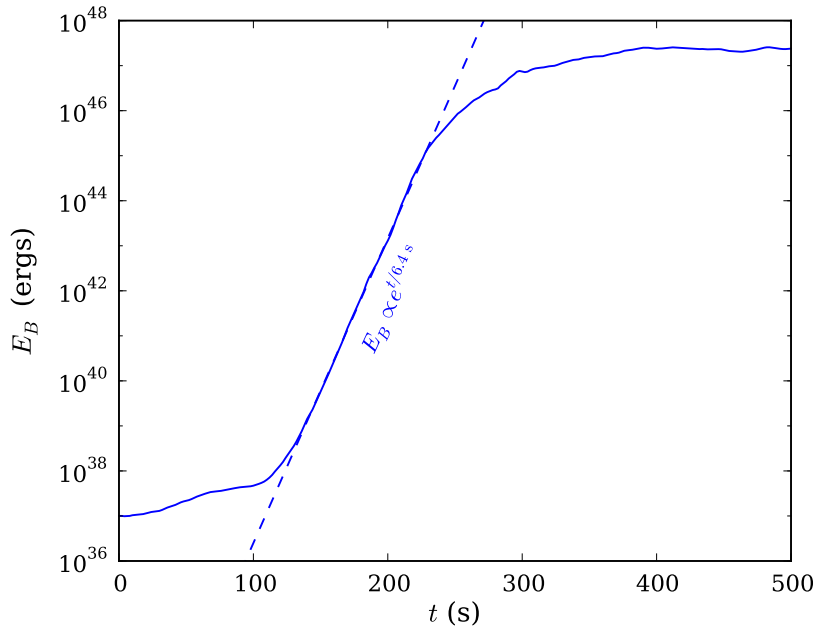


Figure 4.2: Total magnetic energy E_B over time, with a best fit to the rapid exponential growth (dashed $E_B \propto e^{t/6.4\text{s}}$ line).

of the merger remnant at 400 s. The remnant consists of a dense, degeneracy-supported core containing $\sim 60\%$ of the remnant’s mass, a partly thermally supported hot envelope that surrounds the core, and a rotationally supported disk, a configuration similar to the SPH 0.625–0.65 M_\odot remnant from Z13. The AREPO remnant core, however, has distinctly non-axisymmetric density and temperature structures, unlike the SPH simulation which achieves axisymmetry ~ 170 s after coalescence (Z13, online figure set Fig. 1.16). The magnetic fields are too weak during the merger to have an effect on merger dynamics, so these contrasts are due to differences in the *hydrodynamic* schemes between AREPO and SPH (C. Zhu et al. 2015, in preparation).

The remnant magnetic field configuration is complex: while field lines are coherent along “strands” of high field strength, neighboring strands often point in opposite directions (see Fig. 4.3). In the core, the volume-averaged field strength is 4×10^{10} G, but strands of $> 10^{11}$ G field perforate the core. The field remains $> 10^9$ G near the core-disk interface at $\sim 10^9$ cm, before dropping below 10^7 G at $\gtrsim 3 \times 10^9$ cm. The total magnetic field energy is $\sim 0.2\%$ the total, $\sim 0.6\%$ the total rotational, and $\sim 6\%$ the total differential rotation energy of the remnant.¹ This energy is roughly equally partitioned into toroidal and poloidal field components, with the ratio of poloidal to total magnetic energy $E_{B\phi}/E_B = 0.62$. Studies of local field amplification within Kelvin-Helmholtz vortices predict magnetic growth saturates when the magnetic and kinetic energy densities are close to equipartition (Obergaulinger et al. 2010; Zrake & MacFadyen 2013). In our simulation, this is only the case for the strands of $> 10^{11}$ G field, where magnetic energy density is $\sim 7\%$ ($\sim 47\%$) the rotational (differential rotation) energy density (see Fig. 4.3, column 4). It is possible that because the strands are distributed throughout the core, they drive the core’s overall evolution and inhibit further magnetic amplification

¹Differential rotation energy of a cell is estimated with $E_{\text{drot}} = m_{\text{cell}}|\mathbf{v}| |\nabla \times \mathbf{v}| V_{\text{cell}}^{1/3}$.

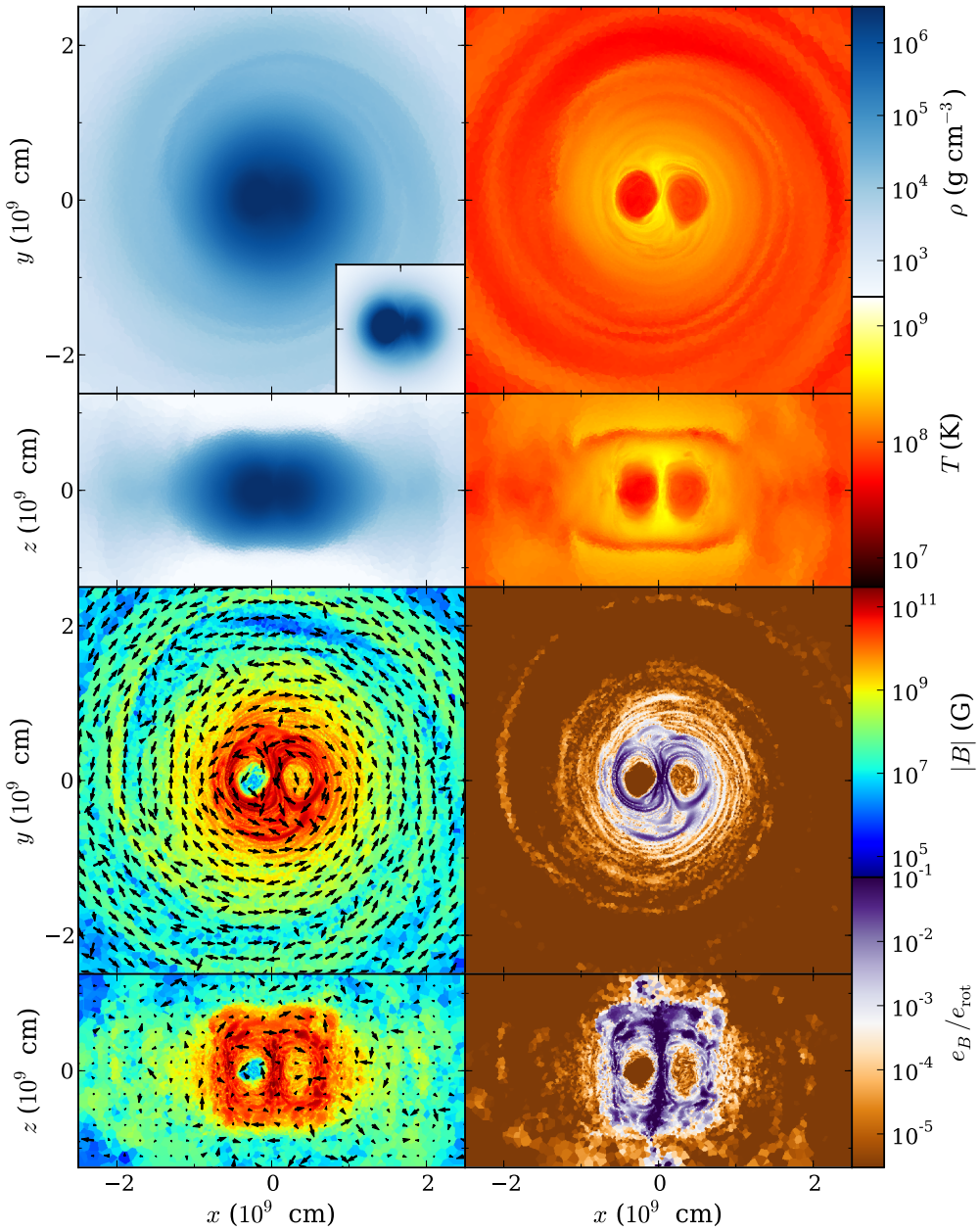


Figure 4.3: From leftmost to rightmost column, equatorial plane (top row) and polar (bottom) logarithmic intensity profiles of density ρ , temperature T , magnetic field strength $|B|$ and ratio of magnetic to rotational energy density e_B/e_{rot} for the simulation at 400 s (~ 170 s after coalescence). The equatorial plane density plot includes a linear profile of the remnant core (with the same x and y scale as the logarithmic profile) to show its shape. Arrows in the magnetic field strength plots indicate field directions, with their lengths equal to the fraction of the field that lies along the xy plane (top frame) and xz plane (bottom).

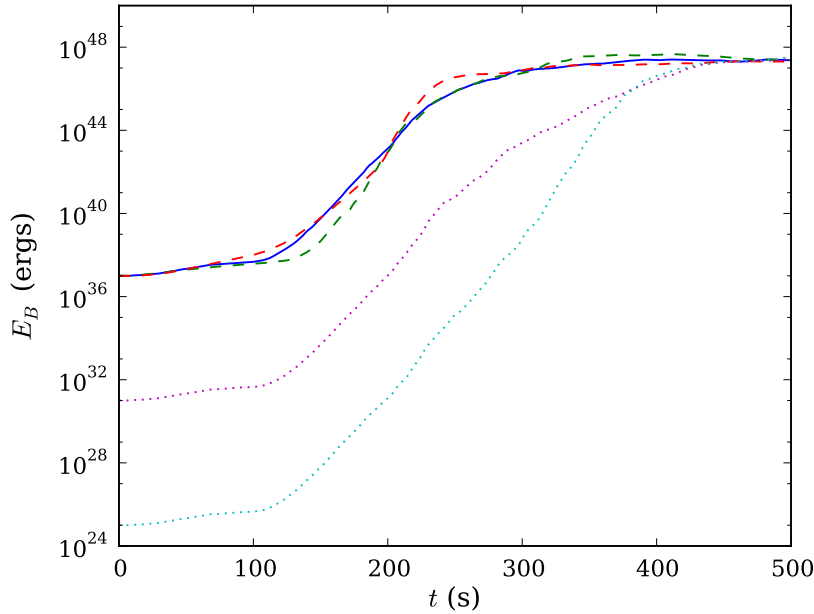


Figure 4.4: Total magnetic energy E_B over time for the fiducial (solid blue; $m_{\text{cell}} \approx 1 \times 10^{-6} M_\odot$, equatorial surface field strength 10^3 G) simulation and the robustness tests. Dashed lines represent low (green; $m_{\text{cell}} \approx 5 \times 10^{-6} M_\odot$) and high resolution (red; $m_{\text{cell}} \approx 2 \times 10^{-7} M_\odot$) simulations. Dotted lines represent 1 G (magenta) and 10^{-3} G (cyan) low initial field simulations.

in their surroundings.

Some of the magnetized accretion stream is ejected during coalescence and integrates into the inner disk ($\sim 1 - 3 \times 10^9$ cm), producing a $10^7 - 10^8$ G field by 400 s. This field has a negligible hydrodynamic effect on the disk (magnetic energy density to pressure ratio $e_B/P \approx 3 \times 10^{-5}$ at 2×10^9 cm), and, unlike the field in the core, has *not* saturated: $|B|$ continues to grow exponentially with $\tau \sim 200$ s.²

4.4 Robustness Tests

4.4.1 Resolution Test

To check that our results are not resolution-limited, we performed simulations, otherwise identical to the fiducial one in Sec. 4.3, with lower and higher mass resolutions of $m_{\text{cell}} \approx 5 \times 10^{-6} M_\odot$ and $m_{\text{cell}} \approx 2 \times 10^{-7} M_\odot$, respectively. Fig. 4.4 compares the E_B evolution between these simulations (dashed lines) and the fiducial one (solid).

The three runs are qualitatively identical. Donor disruption and the start of exponential field growth occurs ~ 0.75 orbital periods earlier at low resolution, and ~ 0.5 periods later at high, because the outer layers of the WDs are better captured and the differences in hydrostatic equilibrium between AREPO and GASOLINE are less pronounced at higher resolution. Exponential growth rates are similar between

²The remnant disk is generally poorly resolved, even at the highest resolution used in Sec. 4.4.1; this may artificially slow the disk field growth rate.

the runs - the E_B *e*-folding time is $\tau = 4.9$ s for the low resolution run, faster than $\tau = 6.4$ s for the fiducial. At high resolution, the growth curve appears to be separated into two phases, with $\tau = 7.8$ s before coalescence, and $\tau = 3.9$ s during it. The total magnetic energy at the end of exponential growth is also similar - at 400 s, E_B is $\sim 4 \times 10^{47}$ ergs in the low resolution run and $\sim 1.5 \times 10^{47}$ ergs in the high, compared to $\sim 2 \times 10^{47}$ ergs at the fiducial resolution. The fiducial and high resolution runs also qualitatively have very similar magnetic field structures by 400 s. Our fiducial resolution of $1 \times 10^{-6} M_\odot$ therefore appears sufficient for qualitatively capturing the growth and final field configuration of the merger.

In their MHD disk galaxy simulations, [Pakmor & Springel \(2013\)](#) find faster field growth and higher field strength at saturation in their lowest resolution run, which they attribute to larger divergence errors at lower resolution. We perform a similar test, and also see a trend of decreasing divergence error (and more accurate magnetic evolution) at higher resolution, though the errors of all our simulations are at least a factor of two smaller than any reported in [Pakmor & Springel \(2013\)](#). The errors are highly localized in space and trace steep magnetic gradients, suggesting they contribute only to small-scale variations in the magnetic field.

4.4.2 Changing the Seed Field Strength

To understand the dependence of our results on the initial seed field, we ran two additional simulations in which we decreased the strength of the seed field by 3 and 6 orders of magnitude leading to an initial equatorial surface field of 1 G (central field $\sim 2 \times 10^4$ G), and 10^{-3} G (~ 20 G), respectively. Fig. 4.4 shows their E_B evolution (dotted lines). We find the growth curves to be homologous between both low initial field runs and the fiducial one – differing only by the ratios of seed E_B – up to ~ 200 s, with the *e*-folding time for exponential amplification approximately 6.5 s for all three runs. By ~ 250 s, the field in the fiducial simulation begins to plateau, while amplification (of initially weaker fields) continues for several hundred more seconds in the low initial field runs. For both runs, E_B plateaus at $\sim 3 \times 10^{47}$ ergs, comparable to the fiducial $\sim 2 \times 10^{47}$ ergs. Because the fields in the low initial field runs remain dynamically irrelevant for longer, however, their structures differ from that of the fiducial run and resemble more the crescent in Fig. 4.1, row 4. The disk field does not saturate in any simulation – its strength is proportional to the strength of the seed field, and is thus much weaker in the low initial field runs. Our tests thus suggest that the exponential growth, growth timescale and plateau E_B are robust to changes in initial field strength, while the remnant field configuration is more sensitive to the choice of seed field.

4.5 Discussion

We have shown that the merger of a $0.625 - 0.65 M_\odot$ CO WD binary produces a strong, $> 10^{10}$ G magnetic field with a complex structure that winds through the remnant core and into the inner disk. Similar to previous simulations of binary NS mergers, the strong field is generated by dynamo action within Kelvin-Helmholtz vortices formed during the coalescence of the two WDs. Since these vortices are ubiquitous in WD mergers, strong magnetic fields are a likely feature of all merger remnants. The degree to which a field permeates the remnant core depends on how thoroughly the donor and accretor mix during coalescence, which itself is sensitive to initial conditions such as the degree

of synchronization between the WDs, or how accurately their tidal bulges and early mass transfer are captured (Dan et al. 2011; 2014). A parameter space study of magnetized mergers is needed to investigate the range of possible remnant field configurations.

We note that NS mergers simulated in Eulerian grid codes generally show E_B growing by only a factor of $\sim 10^2 - 10^3$ during coalescence, compared to the $\sim 10^9$ we see, despite these simulations having resolutions comparable or superior to our low resolution AREPO run. This weaker growth is also inconsistent with the amplification to local kinetic equipartition seen in small-scale simulations (Obergaulinger et al. 2010; Zrake & MacFadyen 2013), and is attributed to insufficient resolution in the NS merger simulations (Kiuchi et al. 2014; Giacomazzo et al. 2015, though see Dionysopoulou et al. 2015). Giacomazzo et al. (2015) incorporated a subgrid magnetic amplification model, calibrated using Zrake & MacFadyen (2013)s results, into their Eulerian NS merger simulation, and found E_B amplification by a factor of $\sim 10^{10}$ over a single dynamical time.³ This suggests AREPO may be better able to resolve small-scale velocity structures than an Eulerian code at comparable resolution, or better able to couple these structures to magnetic growth. Further work is needed to understand the magnetic field growth in detail.

The density profile of the remnant remains non-axisymmetric for hundreds of seconds after coalescence. As a result, the core continues to evolve dynamically, and by 400 s has begun to launch a pair of spiral waves into the surrounding medium (see the density panel of Fig. 4.3), which transport angular momentum on a timescale rivalling that for magnetic shear. While Kashyap et al. (2015) report a similar spiral instability in their Eulerian remnant evolution simulation, SPH simulations like those of Z13 rapidly achieve axisymmetry after coalescence and do not form spiral waves. As noted earlier, this difference between AREPO and SPH simulations is a product of the differences between their hydrodynamic schemes. Further study is needed to understand these differences and their consequences for remnant evolution (C. Zhu et al. 2015, in preparation).

The post-merger evolution of the remnant has been followed to $\sim 3 \times 10^4$ s with axisymmetric cylindrical (two-dimensional) Eulerian grid simulations (Schwab et al. 2012; Ji et al. 2013). As described earlier, Ji et al. (2013)s MHD simulation of a $0.6 - 0.6 M_\odot$ remnant shows the development of a strong magnetic field due to MRI. The subsequent heating and angular momentum transport due to the fields pushes core temperatures to ignition, supporting the possibility of a nuclear runaway within sub- M_{Ch} remnants. Their results are, however, likely sensitive both to their initial hydrodynamic conditions – which may have artificially high core temperatures – and their chosen seed magnetic field, a pure poloidal one to optimize the onset of MRI. Our much stronger poloidal-toroidal field could substantially change post-merger evolution. Moreover, the persistence of a non-axisymmetric remnant core will lead to evolution that clearly cannot be captured in a axisymmetric cylindrical grid. We therefore stress the need to perform high-resolution three-dimensional simulations of post-merger evolution to determine the final fate of the remnant.

There are a number of potentially observable consequences of the magnetic fields produced by the merger. Ji et al. (2013) note the creation of a magnetized corona and biconal jet in their simulations, which act in concert to cause an outflow of material near the remnant’s poles. This outflow eventually unbinds $\sim 10^{-3} M_\odot$ of material, and Beloborodov (2014) estimates it should lead to an optical transient with a duration of ~ 1 day and peak $L \sim 10^8 L_\odot$, which should be detectable by optical surveys.

³Price & Rosswog (2006)s SPH simulations also show strong amplification; while runs using their Euler potential MHD method suffer exaggerated field growth from improper boundary conditions, their B -based runs show similar results (Price 2012).

If a remnant later experiences a nuclear runaway and explodes as a SN Ia, its magnetic field will increase the late-time emission by trapping positrons (produced by ^{56}Co β^+ decay) that would otherwise escape the ejecta. The trapping efficiency depends on the strength and configuration of the remnant magnetic field, with a locally entangled $\sim 10^{11}$ G field – similar to our findings – well able to trap positrons past 1000 days (Ruiz-Lapuente & Spruit 1998). This is in line with observed late-time SN Ia light curves (most recently Kerzendorf et al. 2014).

Those remnants that do not explode will retain strong fields when they reach quiescence, and populate the high-mass tail of the distribution of isolated high-field magnetic WDs (García-Berro et al. 2012; Külebi et al. 2013; Wickramasinghe et al. 2014; Briggs et al. 2015). Since these remnants will have temperatures high enough to fuse any remaining hydrogen and helium they possess, their properties might eventually be akin to the recently discovered hot DQ WDs (e.g. Dufour et al. 2013). These WDs have carbon-dominated atmospheres and $T_{\text{eff}} \approx 2 \times 10^4$ K, are often strongly magnetized (~ 1 MG) and sometimes have monoperiodic photometric variability (possibly due to rapid rotation). Their origins remain unclear (Althaus et al. 2009; Lawrie et al. 2013; Williams et al. 2013). Dunlap & Clemens (in press) recently found that, if most known hot DQs are massive ($M \gtrsim 0.95M_{\odot}$), their population’s velocity dispersion corresponds to a kinematic age much older than what would be inferred from their temperatures, suggesting that at least some hot DQs are WD-WD merger remnants. If so, their observed properties would constrain merger and remnant evolutionary models, and double-degenerate channels for SNe Ia.

We thank Christopher Thompson, Christopher Matzner, Volker Springel, Bart Dunlap, Yuri Levin, Henk Spruit, Ue-Li Pen and Stephen Ro for their insights into magnetohydrodynamics and simulations. This work utilized the SciNet HPC Consortium’s GPC supercomputer (Loken et al. 2010). C.Z. acknowledges support from the Natural Sciences and Engineering Research Council (NSERC) Vanier Canada Graduate Scholarship. R.P. acknowledges support by the European Research Council under ERC-StG grant EXAGAL-308037 and by the Klaus Tschira Foundation. P.C. is supported by the NASA ATP program through NASA grant NNX13AH43G, and NSF grant AST-1255469.

4.6 Postscript: Reconsidering Divergence Cleaning in Arepo

In Sec. 4.5 we discussed why AREPO was capturing (at least some proxy of) rapid magnetic amplification during the merger when Eulerian simulations of NS mergers at similar resolutions do not. Since the publication of Z15, it has been pointed out that amplification could be the spurious result of AREPO’s divergence cleaning mechanism.

In most multidimensional numerical MHD schemes, the “divergence constraint” of $\nabla \cdot \mathbf{B} = 0$ is not guaranteed, and if the implicit divergence terms in Eqn. 3.1 are not considered, these schemes can in practice lead to spurious forces and magnetic instabilities (Tóth 2000; Hopkins & Raives 2016). A number of solutions exist (eg. Tóth 2000), and the most widely-used is Evans & Hawley (1988)’s constrained transport (CT) method, which staggers the different components of the magnetic field within the discretization to maintain the divergence constraint to round-off errors. This reliance on grid geometry, however, has made it challenging to implement in a moving mesh code (Mocz et al. 2014). Until the very-recent adoption of constrained transport in AREPO in June 2016 (Mocz et al. 2016), the code instead used either the Dedner et al. (2002) or Powell et al. (1999) divergence control schemes.

The former introduces an additional conserved scalar term ψ to \mathbf{U} in Eqn. 3.2 which is coupled to $\nabla \cdot \mathbf{B}$ while simultaneously being advected and forced to exponentially decay. The latter adds a source term to the righthand side of Eqn. 3.2 that is proportional to $\nabla \cdot \mathbf{B}$, which passively advects divergence errors but does not damp them. The Dedner method is superior because it actively minimizes divergence errors rather than simply preventing their local accumulation, but its implementation in AREPO requires prohibitively small timesteps and tended to become unstable in highly dynamic environments (Pakmor & Springel 2013), hence our use of the Powell scheme.

In Fig. 4.5 we plot the magnetic field strength, relative divergence error and absolute relative divergence error of our fiducial merger simulation at $t = 200$ s, when the donor has just been disrupted. The (mass-weighted) average relative divergence error $\langle |\nabla \cdot \mathbf{B}|(V_{\text{cell}})^{1/3}/B \rangle = 0.18$, where V is the Voronoi cell volume, is typical of both this simulation and Pakmor & Springel (2013)'s, but much larger than typical results from Dedner cleaning-based codes (Tricco 2015; Hopkins & Raives 2016). As in Pakmor & Springel (2013)'s galaxy disk evolution simulation, the divergence error alternates on very small scales (Fig. 4.5 middle panel), and peaks near large magnetic gradients (comparing top and bottom panels). While errors cancel over large scales (the average relative error with the sign of the divergence included is $\langle \nabla \cdot \mathbf{B}(V_{\text{cell}})^{1/3}/B \rangle = -1.4 \times 10^{-3}$), the regions of highest magnetic gradient correspond to the shear interface between donor and accretor, where we believe the field is amplified. It is therefore plausible that errors at small scales spuriously magnify the magnetic dynamo associated with the shear layer and Kelvin-Helmholtz vortices.

This hypothesis is supported by Hopkins & Raives (2016), who perform a battery of tests comparing the Dedner and Powell mechanisms for their mesh-free finite-volume code GIZMO, and show divergence errors in Powell-based simulations of advection and hydromagnetic instability lead to spurious and unstable field growth. Moreover, comparisons between Powell and CT-based AREPO in simulations of MHD turbulence and disk galaxy evolution show that the Powell scheme leads to greater magnetic field amplification by up to an order of magnitude, as well as a qualitatively different field topology (Mocz et al. 2016).

Caution is therefore in order when using this chapter's results, which are subject to confirmation by merger simulations using AREPO's new CT scheme. Given that the results will likely be different, it may also be useful to conduct a simpler test case of field evolution within a single Kelvin-Helmholtz vortex at various resolutions compared to the results of Obergaulinger et al. (2010) and Zrake & MacFadyen (2013). Meanwhile, the remnant magnetic field's bulk properties following coalescence are physically plausible, as discussed in Sec. 4.3, and are likely to be more robust than the detailed field configuration. We cite these properties (alongside Ji et al. (2013)'s work) when considering magnetic simmering WDs the next chapter.

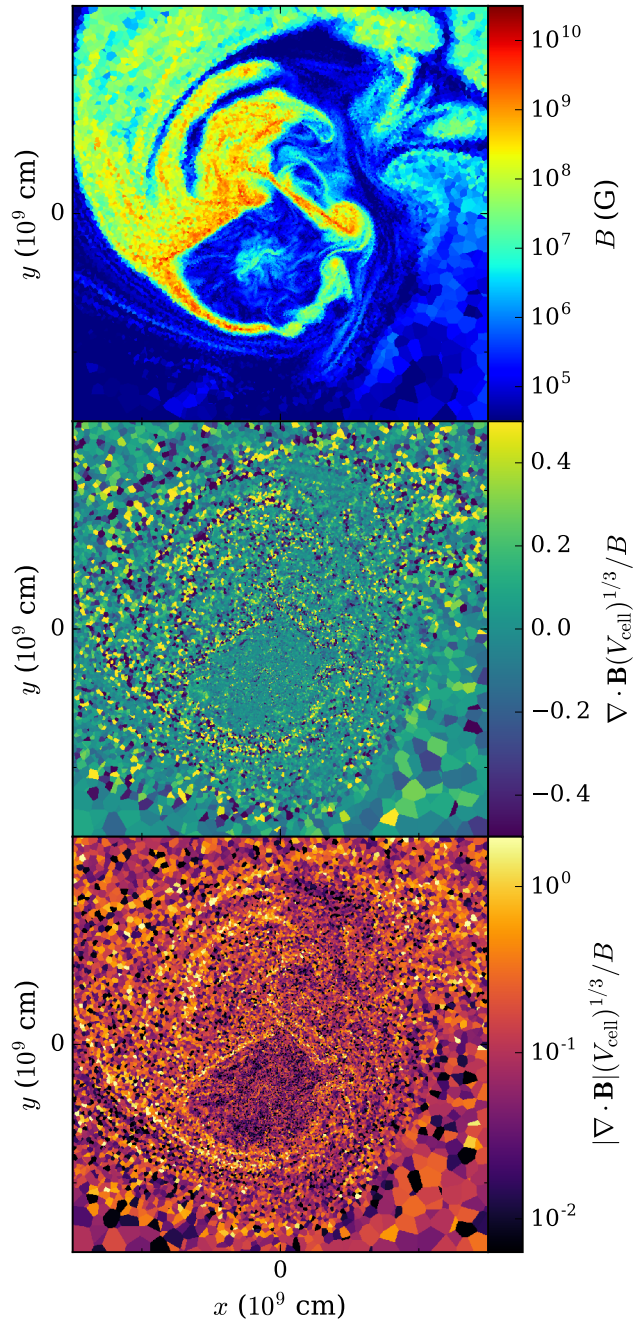


Figure 4.5: From top to bottom, equatorial plane intensity profiles for the magnetic field strength, relative divergence error (linear scale) and absolute relative divergence error (logarithmic) for the simulation at 200 s.

Bibliography

- Abbott, B. P., Abbott, R., Abbott, T. D., et al. 2016, Physical Review Letters, 116, 131102
- Abdikamalov, E. B., Ott, C. D., Rezzolla, L., et al. 2010, Phys. Rev. D, 81, 044012
- Agertz, O., Moore, B., Stadel, J., et al. 2007, MNRAS, 380, 963
- Althaus, L. G., García-Berro, E., Cársico, A. H., Miller Bertolami, M. M., & Romero, A. D. 2009, ApJ, 693, L23
- Andronov, N., Pinsonneault, M. H., & Terndrup, D. M. 2006, ApJ, 646, 1160
- Aspden, A. J., Bell, J. B., Dong, S., & Woosley, S. E. 2011, ApJ, 738, 94
- Badenes, C., & Maoz, D. 2012, ApJ, 749, L11
- Balbus, S. A. 2003, ARA&A, 41, 555
- Balbus, S. A., & Hawley, J. F. 1991, ApJ, 376, 214
- Barstow, M. A., Jordan, S., O'Donoghue, D., et al. 1995, MNRAS, 277, 971
- Beloborodov, A. M. 2014, MNRAS, 438, 169
- Benz, W., Cameron, A. G. W., Press, W. H., & Bowers, R. L. 1990, ApJ, 348, 647
- Briggs, G. P., Ferrario, L., Tout, C. A., Wickramasinghe, D. T., & Hurley, J. R. 2015, MNRAS, 447, 1713
- Brown, W. R., Kilic, M., Hermes, J. J., et al. 2011, ApJ, 737, L23
- Cha, S.-H., & Wood, M. A. 2016, MNRAS, 458, 480
- Clayton, G. C. 2013, in Astronomical Society of the Pacific Conference Series, Vol. 469, 18th European White Dwarf Workshop., 133
- Clayton, G. C., Geballe, T. R., Herwig, F., Fryer, C., & Asplund, M. 2007, ApJ, 662, 1220
- Cullen, L., & Dehnen, W. 2010, MNRAS, 408, 669
- Dan, M., Rosswog, S., Brüggen, M., & Podsiadlowski, P. 2014, MNRAS, 438, 14
- Dan, M., Rosswog, S., Guillochon, J., & Ramirez-Ruiz, E. 2011, ApJ, 737, 89
- . 2012, MNRAS, 422, 2417

- de Val-Borro, M., Edgar, R. G., Artymowicz, P., et al. 2006, MNRAS, 370, 529
- Dedner, A., Kemm, F., Kröner, D., et al. 2002, Journal of Computational Physics, 175, 645
- Dehnen, W., & Aly, H. 2012, MNRAS, 425, 1068
- Dionysopoulou, K., Alic, D., & Rezzolla, L. 2015, Phys. Rev. D, 92, 084064
- Dolag, K., Vazza, F., Brunetti, G., & Tormen, G. 2005, MNRAS, 364, 753
- D'Souza, M. C. R., Motl, P. M., Tohline, J. E., & Frank, J. 2006, ApJ, 643, 381
- Duffell, P. C., & MacFadyen, A. I. 2011, ApJS, 197, 15
- Dufour, P., Vornanen, T., Bergeron, P., & Fontaine, A., B. 2013, in Astronomical Society of the Pacific Conference Series, Vol. 469, 18th European White Dwarf Workshop., 167
- Dunlap, B. H., & Clemens, J. C. 2015, in Astronomical Society of the Pacific Conference Series, Vol. 493, 19th European Workshop on White Dwarfs, ed. P. Dufour, P. Bergeron, & G. Fontaine, 547
- Eggleton, P. P. 1983, ApJ, 268, 368
- Evans, C. R., & Hawley, J. F. 1988, ApJ, 332, 659
- Feiden, G. A., & Chaboyer, B. 2012, ApJ, 761, 30
- Fryxell, B., Olson, K., Ricker, P., et al. 2000, ApJS, 131, 273
- Fuller, J., & Lai, D. 2012, MNRAS, 421, 426
- Gaburov, E., Johansen, A., & Levin, Y. 2012, ApJ, 758, 103
- García-Berro, E., Lorén-Aguilar, P., Aznar-Siguán, G., et al. 2012, ApJ, 749, 25
- Giacomazzo, B., Zrake, J., Duffell, P. C., MacFadyen, A. I., & Perna, R. 2015, ApJ, 809, 39
- Gingold, R. A., & Monaghan, J. J. 1977, MNRAS, 181, 375
- Goedbloed, J. P. H., & Poedts, S. 2004, Principles of Magnetohydrodynamics
- Governato, F., Weisz, D., Pontzen, A., et al. 2015, MNRAS, 448, 792
- Guerrero, J., García-Berro, E., & Isern, J. 2004, A&A, 413, 257
- Hamann, W.-R. 1997, in IAU Symposium, Vol. 180, Planetary Nebulae, ed. H. J. Habing & H. J. G. L. M. Lamers, 91
- Hayes, J. C., Norman, M. L., Fiedler, R. A., et al. 2006, ApJS, 165, 188
- Hayward, C. C., Torrey, P., Springel, V., Hernquist, L., & Vogelsberger, M. 2014, MNRAS, 442, 1992
- Hernquist, L., & Katz, N. 1989, ApJS, 70, 419
- Heß, S., & Springel, V. 2010, MNRAS, 406, 2289
- Hillebrandt, W., Kromer, M., Röpke, F. K., & Ruiter, A. J. 2013, Frontiers of Physics, 8, 116

- Hopkins, P. F. 2013, MNRAS, 428, 2840
- . 2015, MNRAS, 450, 53
- Hopkins, P. F., & Raives, M. J. 2016, MNRAS, 455, 51
- Howell, D. A. 2011, Nature Communications, 2, 350
- Hu, C.-Y., Naab, T., Walch, S., Moster, B. P., & Oser, L. 2014, MNRAS, 443, 1173
- Ji, S., Fisher, R. T., García-Berro, E., et al. 2013, ApJ, 773, 136
- Justham, S., Podsiadlowski, P., & Han, Z. 2011, MNRAS, 410, 984
- Justham, S., Podsiadlowski, P., & Vink, J. S. 2014, ApJ, 796, 121
- Kaiser, N., Burgett, W., Chambers, K., et al. 2010, in Proc. SPIE, Vol. 7733, Ground-based and Airborne Telescopes III, 77330E
- Kashyap, R., Fisher, R., García-Berro, E., et al. 2015, ApJ, 800, L7
- Katz, M. P., Zingale, M., Calder, A. C., et al. 2016, ApJ, 819, 94
- Keller, B. W., Wadsley, J., Benincasa, S. M., & Couchman, H. M. P. 2014, MNRAS, 442, 3013
- Keller, B. W., Wadsley, J., & Couchman, H. M. P. 2015, MNRAS, 453, 3499
- Kerzendorf, W. E., Taubenberger, S., Seitenzahl, I. R., & Ruiter, A. J. 2014, ApJ, 796, L26
- Kiuchi, K., Kyutoku, K., Sekiguchi, Y., Shibata, M., & Wada, T. 2014, Phys. Rev. D, 90, 041502
- Kleinman, S. J., Kepler, S. O., Koester, D., et al. 2013, ApJS, 204, 5
- Knigge, C., Leigh, N., & Sills, A. 2009, Nature, 457, 288
- Külebi, B., Ekşit, K. Y., Lorén-Aguilar, P., Isern, J., & García-Berro, E. 2013, MNRAS, 431, 2778
- Külebi, B., Jordan, S., Nelan, E., Bastian, U., & Altmann, M. 2010, A&A, 524, A36
- Lai, D., Rasio, F. A., & Shapiro, S. L. 1994, ApJ, 437, 742
- Lawrie, K. A., Burleigh, M. R., Dufour, P., & Hodgkin, S. T. 2013, MNRAS, 433, 1599
- Loken, C., Gruner, D., Groer, L., et al. 2010, Journal of Physics Conference Series, 256, 012026
- Lorén-Aguilar, P., Isern, J., & García-Berro, E. 2009, A&A, 500, 1193
- LSST Science Collaboration, Abell, P. A., Allison, J., et al. 2009, ArXiv e-prints, arXiv:0912.0201
- Lucy, L. B. 1977, AJ, 82, 1013
- Maeda, K., Taubenberger, S., Sollerman, J., et al. 2010a, ApJ, 708, 1703
- Maeda, K., Benetti, S., Stritzinger, M., et al. 2010b, Nature, 466, 82
- Maoz, D., Mannucci, F., & Nelemans, G. 2014, ARA&A, 52, 107

- Marinacci, F., Pakmor, R., & Springel, V. 2014, MNRAS, 437, 1750
- Marsh, T. R., Nelemans, G., & Steeghs, D. 2004, MNRAS, 350, 113
- Mazurek, T. J., Meier, D. L., & Wheeler, J. C. 1977, ApJ, 213, 518
- Mitchell, N. L., McCarthy, I. G., Bower, R. G., Theuns, T., & Crain, R. A. 2009, MNRAS, 395, 180
- Miyoshi, T., & Kusano, K. 2005, Journal of Computational Physics, 208, 315
- Mocz, P., Pakmor, R., Springel, V., et al. 2016, ArXiv e-prints, arXiv:1606.02310
- Mocz, P., Vogelsberger, M., & Hernquist, L. 2014, MNRAS, 442, 43
- Moll, R., Raskin, C., Kasen, D., & Woosley, S. E. 2014, ApJ, 785, 105
- Monaghan, J. J. 2005, Reports on Progress in Physics, 68, 1703
- Morris, J. P., & Monaghan, J. J. 1997, Journal of Computational Physics, 136, 41
- Nandez, J. L. A., Ivanova, N., & Lombardi, Jr., J. C. 2014, ApJ, 786, 39
- Nomoto, K., & Iben, Jr., I. 1985, ApJ, 297, 531
- Obergaulinger, M., Aloy, M. A., & Müller, E. 2010, A&A, 515, A30
- Ohlmann, S. T., Röpke, F. K., Pakmor, R., & Springel, V. 2016, ApJ, 816, L9
- Pakmor, R., Bauer, A., & Springel, V. 2011a, MNRAS, 418, 1392
- Pakmor, R., Hachinger, S., Röpke, F. K., & Hillebrandt, W. 2011b, A&A, 528, A117
- Pakmor, R., Kromer, M., Röpke, F. K., et al. 2010, Nature, 463, 61
- Pakmor, R., Kromer, M., Taubenberger, S., et al. 2012, ApJ, 747, L10
- Pakmor, R., Kromer, M., Taubenberger, S., & Springel, V. 2013, ApJ, 770, L8
- Pakmor, R., & Springel, V. 2013, MNRAS, 432, 176
- Pakmor, R., Springel, V., Bauer, A., et al. 2016, MNRAS, 455, 1134
- Papaloizou, J. C. B., & Lin, D. N. C. 1995, ARA&A, 33, 505
- Paxton, B., Bildsten, L., Dotter, A., et al. 2011, ApJS, 192, 3
- Paxton, B., Cantiello, M., Arras, P., et al. 2013, ApJS, 208, 4
- Paxton, B., Marchant, P., Schwab, J., et al. 2015, ApJS, 220, 15
- Piro, A. L. 2011, ApJ, 740, L53
- Powell, K. G., Roe, P. L., Linde, T. J., Gombosi, T. I., & De Zeeuw, D. L. 1999, Journal of Computational Physics, 154, 284
- Price, D. J. 2008, Journal of Computational Physics, 227, 10040

- . 2012, *Journal of Computational Physics*, 231, 759
- Price, D. J., & Rosswog, S. 2006, *Science*, 312, 719
- Raskin, C., Kasen, D., Moll, R., Schwab, J., & Woosley, S. 2014, *ApJ*, 788, 75
- Raskin, C., Scannapieco, E., Fryer, C., Rockefeller, G., & Timmes, F. X. 2012, *ApJ*, 746, 62
- Rau, A., Kulkarni, S. R., Law, N. M., et al. 2009, *PASP*, 121, 1334
- Read, J. I., Hayfield, T., & Agertz, O. 2010, *MNRAS*, 405, 1513
- Rosswog, S. 2009, *New A Rev.*, 53, 78
- . 2015, *International Journal of Modern Physics D*, 24, 1530012
- Ruiz-Lapuente, P., & Spruit, H. C. 1998, *ApJ*, 500, 360
- Saio, H., & Jeffery, C. S. 2000, *MNRAS*, 313, 671
- Saio, H., & Nomoto, K. 1985, *A&A*, 150, L21
- . 1998, *ApJ*, 500, 388
- Schwab, J., Quataert, E., & Kasen, D. 2016, ArXiv e-prints, arXiv:1606.02300
- Schwab, J., Shen, K. J., Quataert, E., Dan, M., & Rosswog, S. 2012, *MNRAS*, 427, 190
- Segretain, L., Chabrier, G., & Mochkovitch, R. 1997, *ApJ*, 481, 355
- Seitenzahl, I. R., Ciaraldi-Schoolmann, F., & Röpke, F. K. 2011, *MNRAS*, 414, 2709
- Seitenzahl, I. R., Meakin, C. A., Townsley, D. M., Lamb, D. Q., & Truran, J. W. 2009, *ApJ*, 696, 515
- Shakura, N. I., & Sunyaev, R. A. 1973, *A&A*, 24, 337
- Shen, K. J., Bildsten, L., Kasen, D., & Quataert, E. 2012, *ApJ*, 748, 35
- Shen, S., Wadsley, J., & Stinson, G. 2010, *MNRAS*, 407, 1581
- Shigeyama, T., Nomoto, K., Yamaoka, H., & Thielemann, F.-K. 1992, *ApJ*, 386, L13
- Sim, S. A., Röpke, F. K., Hillebrandt, W., et al. 2010, *ApJ*, 714, L52
- Springel, V. 2005, *MNRAS*, 364, 1105
- . 2010a, *MNRAS*, 401, 791
- . 2010b, *ARA&A*, 48, 391
- Spruit, H. C. 2002, *A&A*, 381, 923
- . 2013, ArXiv e-prints, arXiv:1301.5572
- Tamburello, V., Mayer, L., Shen, S., & Wadsley, J. 2015, *MNRAS*, 453, 2490
- Taubenberger, S., Benetti, S., Childress, M., et al. 2011, *MNRAS*, 412, 2735

- Timmes, F. X., & Swesty, F. D. 2000, ApJS, 126, 501
- Tóth, G. 2000, Journal of Computational Physics, 161, 605
- Trac, H., Sills, A., & Pen, U.-L. 2007, MNRAS, 377, 997
- Tremblay, P.-E., & Bergeron, P. 2009, ApJ, 696, 1755
- Tricco, T. 2015, in American Astronomical Society Meeting Abstracts, Vol. 225, American Astronomical Society Meeting Abstracts, 211.06
- Tylenda, R., Hajduk, M., Kamiński, T., et al. 2011, A&A, 528, A114
- Uryū, K., & Eriguchi, Y. 1998, ApJS, 118, 563
- van Kerkwijk, M. H., Chang, P., & Justham, S. 2010, ApJ, 722, L157
- Vandenbroucke, B., & De Rijcke, S. 2016, Astronomy and Computing, 16, 109
- Vogelsberger, M., Sijacki, D., Kereš, D., Springel, V., & Hernquist, L. 2012, MNRAS, 425, 3024
- Wadsley, J. W., Stadel, J., & Quinn, T. 2004, New A, 9, 137
- Webbink, R. F. 1984, ApJ, 277, 355
- Wickramasinghe, D. T., Tout, C. A., & Ferrario, L. 2014, MNRAS, 437, 675
- Williams, K. A., Winget, D. E., Montgomery, M. H., et al. 2013, ApJ, 769, 123
- Woosley, S. E., Kerstein, A. R., & Aspden, A. J. 2011, ApJ, 734, 37
- Woosley, S. E., Kerstein, A. R., Sankaran, V., Aspden, A. J., & Röpke, F. K. 2009, ApJ, 704, 255
- Yoon, S.-C., Podsiadlowski, P., & Rosswog, S. 2007, MNRAS, 380, 933
- Yungelson, L. R. 2005, in American Institute of Physics Conference Series, Vol. 797, Interacting Binaries: Accretion, Evolution, and Outcomes, ed. L. Burderi, L. A. Antonelli, F. D'Antona, T. di Salvo, G. L. Israel, L. Piersanti, A. Tornambè, & O. Straniero, 1–10
- Zhu, C., Chang, P., van Kerkwijk, M. H., & Wadsley, J. 2013, ApJ, 767, 164
- Zhu, C., Pakmor, R., van Kerkwijk, M. H., & Chang, P. 2015, ApJ, 806, L1
- Zrake, J., & MacFadyen, A. I. 2013, ApJ, 769, L29